

Proton Irradiation Screening Results of Select Advanced Replacement Alloys for Core Internals

September 2017

This report was prepared by

Gary S. Was
Mi Wang
Miao Song
Calvin Lear

University of Michigan
2355 Bonisteel Blvd.
Ann Arbor, MI 48109

CONTENTS

Excutive Summary.....	I
1 introduction.....	1-1
2 Background.....	2-1
Objectives and Scope.....	2-1
3 Experimental.....	3-1
3.1 Materials and Specimens	3-1
Alloys.....	3-1
Samples.....	3-3
3.2 Sample Preparation for Microstructure Characterization	3-3
3.3 Irradiation Experimental Conditions.....	3-4
3.4 Mechanical Properties Tests Conditions.....	3-8
Hardness Measurement.....	3-8
Tensile Test at Room Temperature.....	3-8
3.5 CERT System and Test Procedure.....	3-9
3.6 Characterization of Cracking Susceptibility	3-10
3.7 Three Point Bend Test System and Procedure.....	3-11
4 Results	4-1
4.1 Irradiation Experiments	4-1
4.2 Microstructure Pre-characterization.....	4-6
4.3 Deformation structure of nickel-base alloys.....	4-9
4.4 Microstructure Characterization of Irradiated Alloys.....	4-12
Dislocation Loops	4-13
Irradiation Induced/Enhanced Precipitation	4-14
Voids.....	4-22
Irradiation Induced Segregation.....	4-22
Microstructure Summary of Irradiated Samples.....	4-25

4.5 Mechanical Properties.....	4-28
Irradiation hardening.....	4-28
Room Temperature Tensile Behavior.....	4-29
4.6 CERT Test Results.....	4-30
Environmental Conditions	4-30
High strength alloys	4-33
Low strength alloys.....	4-36
4.7 Cracking Behavior	4-37
High Strength Alloys	4-37
Low Strength Alloy.....	4-41
IASCC Susceptibility.....	4-42
5 Discussion	5-1
5.1 Formation of LRO phase	5-1
Irradiation Enhanced Formation of LRO Phase.....	5-1
Effect of Iron on The Formation of LRO Phase	5-2
5.2 IASCC Susceptibility of Nickel-Base Alloys.....	5-2
High Strength Alloys	5-3
Low Strength Alloys.....	5-4
6 Conclusions.....	6-1
7 References	7-1

EXECUTIVE SUMMARY

A total of 11 alloys have been irradiated to date, including eight nickel-base alloys, two austenitic stainless steels and a single Fe-Cr ferritic-martensitic (F/M) alloy. They are in various stages of microstructural characterization and assessment of IASCC susceptibility. Microstructural analysis both prior to and following proton irradiation up to 5 displacements per atom (dpa) of damage at 360 °C has been completed on nickel-base alloys 625, 625Plus, 625DA, 725 and 690, and on austenitic iron base alloys 310 and 800. Hardness measurements were made on all irradiated and non-irradiated conditions to quantify radiation hardening. Room temperature stress-strain testing of the four nickel-base alloys, 625, 625Plus, 625DA and 725, were conducted to assess their yield and ultimate tensile strength, and ductility. Stress corrosion cracking behavior in both boiling water reactor normal water chemistry (BWR-NWC) and pressurized water reactor primary water (PWR-PW) was studied. Cracking susceptibility was assessed using the crack length per unit area and the ratio between cracked length and high angle grain boundary (HAGB) length.

- Dislocation loops dominated the irradiated microstructure while voids were limited to only Type 310. Dislocation loops formed in all the alloys irradiated with the largest loops in alloy 800 (~50 nm) and the smallest in 625DA (~13 nm). The loop density varies inversely with size. Voids were observed in Type 310 with a size less than 10 nm and swelling less than 0.28 %. No voids were observed in alloys 625, 625Plus, 625DA, 725, 690 and 800.
- Both irradiation-enhanced and -induced precipitates were observed. Irradiation enhanced long range ordered phase (Ni_2Cr) was observed in most of nickel base alloys 625, 625Plus, 625DA, 725, 690, C22 after proton irradiation. Irradiation induced γ' phase was observed in alloys 690 and 800, with the chemical composition $\text{Ni}_3(\text{Ti}, \text{Al})$ in 690 and Ni_3Si in alloy 800.
- Radiation induced segregation (RIS) were observed in all alloys characterized. In nickel base alloys 625, 625Plus, 625DA, and 725, the as-received condition showed a depletion of Ni, and enrichment of Cr and Mo at the grain boundaries (GB). After irradiation, Ni was enriched, and Cr and Fe were depleted at GB. Mo diffuses slowly away from GB. RIS of other elements were insignificant. The difference in RIS among these alloys is also insignificant. In austenitic steels 310 and 800, little enrichment/depletion was observed in the as-received condition, but significant RIS was observed with Ni and S enrichment, and Cr and Fe depletion at the GB.
- All alloys exhibited some irradiation hardening. Irradiation hardening was greatest in austenitic stainless steels 310, 800 and solid solution nickel base alloys C22, 690. Irradiation hardening was lower in the precipitation hardened alloys (725, 625DA, 625Plus, X750 and 718) with less than a 25 % increase in hardness. Alloy 718 showed the least irradiation hardening. Grade T92, the only F/M steel tested in the program, showed only minimal irradiation hardening.
- Evaluation of IASCC behavior of the high strength nickel-base alloys (625Plus, 725, and 625DA) in both BWR-NWC and PWR-PW revealed that IASCC susceptibility was greater in BWR-NWC than in PWR-PW. Alloy 725 had the lowest IASCC susceptibility in both environments, and alloys 625Plus and 625DA were both highly susceptible to IASCC in both environments. Alloy 625 had intermediate IASCC susceptibility compared to that of the high strength nickel-base alloys.
- Preliminary assessment of the role of irradiated microstructure on IASCC shows that the alloys most susceptible to IASCC have the greatest irradiation-induced microstructural changes, making it difficult to identify the specific feature or combination of features responsible for cracking. However, results do show that radiation induced segregation (RIS) does not play an important role on the IASCC susceptibility of high strength nickel base alloys 625Plus, 625DA and 725.

1 INTRODUCTION

This report summarizes research activities for the Advanced Radiation Resistant Materials (ARRM) program between December 2015 and January 2017. The ARRM project is aimed at identifying promising candidates to replace austenitic stainless steels, which suffer from serious irradiation-assisted stress corrosion cracking (IASCC) in Light Water Reactor (LWR) environments. If suitable replacement materials can be identified, reactors can operate with better efficiency and lower costs of maintenance and repair. The ARRM Program is jointly funded by EPRI and the Department of Energy.

The previous report [1] focused on alloys 625, 625Plus, 625DA and 725. The as-received materials, alloys 625Plus, 625DA and 725, are precipitation hardened. After 5 dpa of proton irradiation damage, less long range order phase was formed in alloy 725 compared with alloy 625, 625Plus or 625DA. Alloy 625Plus exhibited the lowest irradiation hardening. Preliminary evaluation of IASCC of these alloys suggests that alloy 625Plus was more susceptible to IASCC than alloy 725 in BWR-NWC, and alloy 625 had a higher IASCC susceptibility in PWR-PW than in the BWR-NWC. Alloys 625, 625Plus and 625DA exhibited large increases in IASCC susceptibility after proton irradiation to 5dpa.

In this report, several nickel-base alloys and iron-base austenitic alloys were characterized and evaluated for IASCC susceptibility in PWR and BWR-NWC environments. The microstructures were characterized mainly through transmission electron microscopy (TEM). Alloys 310, 800 and 690 were fully characterized including dislocation loops, precipitates and void swelling. Radiation induced segregation (RIS) was characterized by energy-dispersive X-ray spectrometry (EDX) on alloys 625, 625DA, 625Plus, 725, 800 and 310. Irradiation hardening was evaluated for all the alloys irradiated so far. Voids were only observed in alloy 310. Both irradiation-enhanced and irradiation-induced precipitates were observed, such as a long range ordered phase in nickel-base alloys, and γ' phase in 800 and 690. RIS was observed in all the alloys examined with a similar behavior in which Ni and Si are enriched and Cr and Fe are depleted at grain boundaries (GB), while Mo diffuses slowly away from GB. While most of the alloys exhibited 25-150 % hardness increases due to irradiation, alloy 718 and grade T92 exhibited insignificant irradiation hardening.

Constant extension rate tensile (CERT) tests were used to evaluate the IASCC susceptibility. Nickel-base alloys 625Plus, 725, 625DA, and 625 were studied in full. Cracking susceptibility was much higher in BWR-NWC because of its much more aggressive environment than PWR-PW. For high strength nickel base alloys, alloy 725 exhibited the lowest IASCC susceptibility in both water environments while 625Plus and 625DA were both highly susceptible to IASCC. Especially for alloy 625DA, the radiation induced microstructural changes correlated well with

its poor IASCC behavior; however, no dominant microstructure feature could be identified. It seems that RIS does not play an important role in IASCC susceptibility. Low strength alloy 625 has a relatively high susceptibility to IASCC in both BWR-NWC and PWR-PW.

The initial phase of the ARRM program included identification of commercially available candidate materials for irradiation testing. This was followed by procurement of sufficient quantities of the candidate alloys to allow these materials to be tested throughout all phases of the program.

2 BACKGROUND

Irradiation assisted stress corrosion cracking (IASCC) describes the enhancement of stress corrosion cracking susceptibility of materials under irradiation in a light water reactor (LWR) environment. It is identified as one of the primary degradation mechanisms of core components made of stainless steels and nickel-base alloys, which are used in control rod blades, neutron source tubes, baffle bolts, and springs in LWR systems [2-5]. IASCC type degradation has also been observed in supercritical water that will be used in the Supercritical Water Reactor (SCWR), a promising concept for Gen IV nuclear reactors [6, 7]. For a given material, the IASCC susceptibility is known to be controlled by stress state, corrosive media, microstructure, irradiation dose, and may be a combination of effects rather than any sole factor [8].

In practice, austenitic stainless steels used in core components have proved to be problematic, especially at high irradiation dose [9-11]. The fracture toughness of Type 304L SS drops to extremely low values after just 4 dpa irradiation [12]. Void swelling may also become significant at higher dose [13]. More importantly, IASCC has been observed to occur quite early in life [12]. Nickel-base alloys X-750 and 718 show generally good performance in LWRs with a few failures that may have resulted in plant outages [14]. Because, these failures are costly, reselection of materials for LWR life extension may be necessary.

Due to the generally good performance of alloy 718 in nuclear reactors, alloys 625 and 725 have received renewed interest as potential structural materials to replace austenitic stainless steels for core components [9]. Because of its high strength, good fracture toughness and resistance to corrosion over a broad range of severe environments [15-17], alloy 625 continues to find new applications such as in the petroleum industry, waste-to-energy (WTE) boiler system, automotive exhaust system, and aircraft. Alloy 625 is available commercially in a variety of thermal-mechanical treatments. For example, alloy 625 is commonly used as a solid solution alloy. A solid solution and aged version of 625 is called alloy 625Plus. This alloy can also be processed through a direct ageing procedure after hot-working to achieve a high strength and is referred to as 625 direct aged (625DA). By adding titanium at five times the original value, alloy 725 is realized with a faster aging response [16]. Like its predecessor, alloy 725 exhibits similar corrosion resistance but higher strength. However, the application temperature is limited, as is typical for age hardened materials. Alloy 725 has been widely applied in the oil and natural gas industry including offshore and subsea, downhole applications [18-20].

Objectives and Scope

The primary objective of the ARRM program is to identify and test degradation resistant alloys that lies within current commercial alloy specifications by 2024. This includes the develop and

testing of a new advanced alloy with superior degradation resistance. This approach will ensure that a code qualified, radiation resistant material is available for use by vendors and utilities in the near term and will also allow extensive testing to be performed on new advanced materials to ensure their superior performance to very high dose levels.

Candidate alloys were selected based on the weighted score and the state of knowledge of all the potential candidates materials that included commercial alloys as well as novel materials such as ultrafine grained materials and metallic glasses, etc., with consideration of both low strength (Figure 2-1) and high strength (Figure 2-2) applications. The alloys selected as potential high strength materials include alloy 625Plus, alloy 625DA, alloy 725 and 14YWT ODS steel. The alloys chosen for low strength application include alloy 625, T91, alloy 690, alloy 800, alloy 310, C22 and Zr-2.5Nb. The test matrix also includes 316L and X-750 as control alloys for low strength and high-strength applications, respectively.

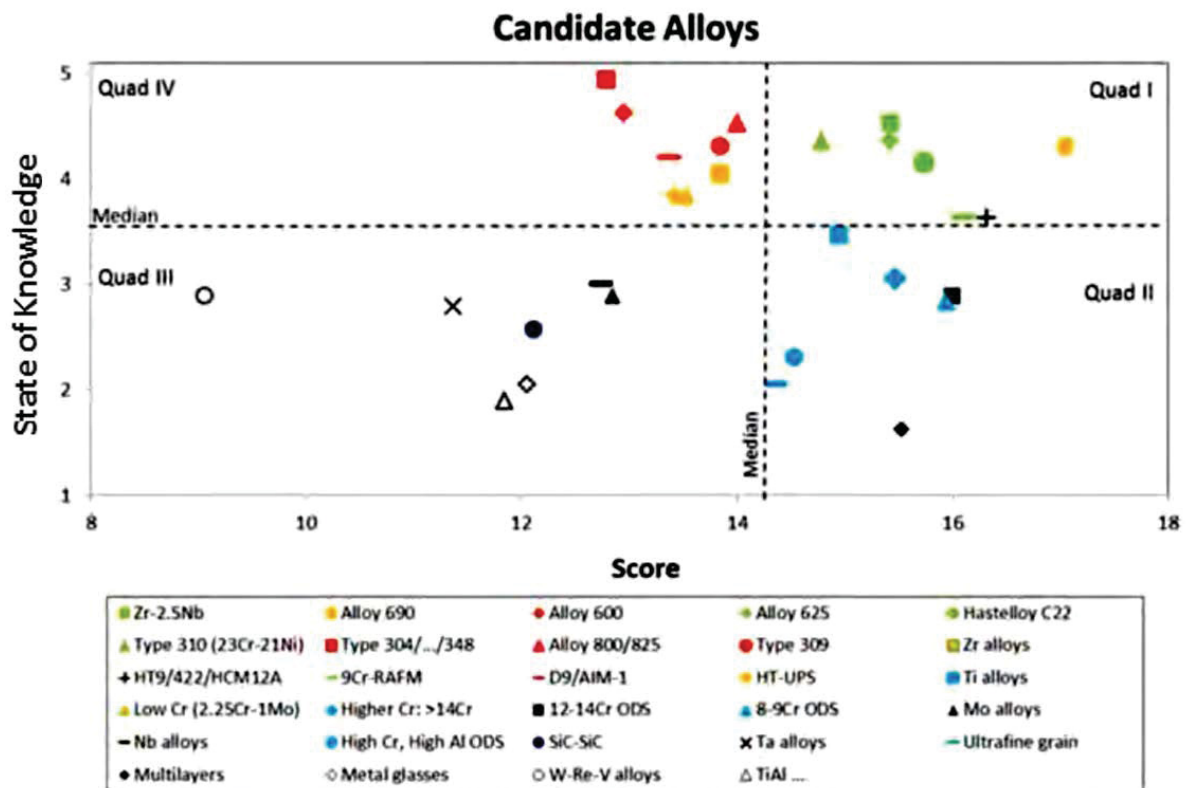


Figure 2-1 The weighted score and state of knowledge of alloys for potential low strength applications[12]

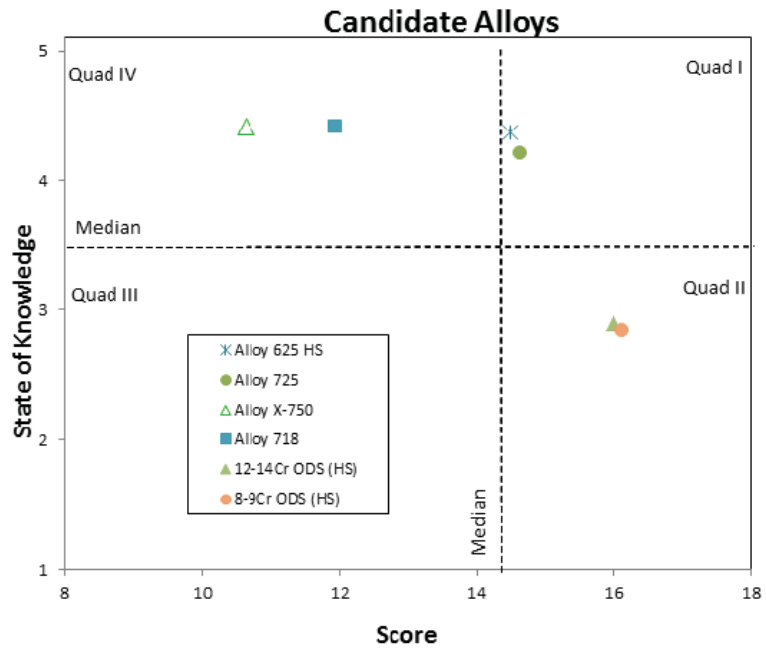


Figure 2-2 The weighted score and state of knowledge of alloys for potential high strength applications[12]

3 EXPERIMENTAL

3.1 *Materials and Specimens*

Alloys

Several groups of materials were tested including nickel-base alloys, austenitic stainless steels, ferritic/martensitic (F/M) steels. The nickel-base alloys included alloys 690, C22, X750, 718 and the alloy 625 family, which includes several heat treatment variants of alloy 625, and a derivative alloy 725. Alloy 625 was examined in three heat treatment conditions of three different heats: 1) solution treated at 955 °C for 0.5 h followed by water quenching, 2) alloy 625Plus solution annealed at 1038 °C for 2 h, fan cooled, then aged at 725°C for 8 h, cooled at 56 °C/h to 621 °C for another 8 h ageing, then air cooled to room temperature, and 3) alloy 625DA where the first alloy 625 heat treatment is direct aging after hot working at 648-667 °C for duration of 81 h, followed by air cooling to room temperature. Although within the alloy 625 specification, these three heats show slightly different chemical compositions. The concentration of Ti in alloy 625Plus is similar to alloy 725 (around 5 times that of alloy 625). Alloy 725 uses the same heat treatment recipe as alloy 625Plus. Alloy 718 was solution annealed at slightly higher temperature of 1093 °C for 1 h, and water quenched, aged at 718 °C for 8 h, cool at 55 °C/h, and finally aged at 621 °C for 8 h. Alloy X750 was solution annealed at 1080 °C for 2 h and aged at 715 °C for 20-22 h before air cooling. Alloys 625, C22 and 690 are tested for low strength applications, while the other alloys are precipitation hardened and designed for high-strength applications. Alloy 800, in a solution annealed condition, was also selected as a candidate for low strength application. Alloy 310 was the only austenitic stainless steel tested so far and was annealing at 1038°C for 1h and water quenched. Grade T92 steel (also known as ASTM A213 T92) was the only F/M steel tested in the program. Chemical compositions for the tested alloys are detailed in Table 3-1.

Table 3-1 Chemical compositions of alloys investigated (wt.%)

Alloy	Ni	Cr	Mo	Fe	Nb	Ti	Al	Ta	C	Si	Mn	Co	P	S	Cu	Mg	B	W	V	N
625	61.02	22.38	8.77	3.51	3.57	.23	.17	.02	.04	.08	.06	.03	.002	.001	-	-	-	-	-	-
625DA	62.41	20.76	8.39	3.88	3.58	.31	.33	.03	.036	.06	.08	.05	.009	.0004	.05	.0039	.0023			
625Plus	60.38	20.99	8.02	Bal.	3.4	1.28	.2	-	.008	.03	.02	-	.001	.0005	-	-	-	-	-	-
725	57.60	21.52	8.07	7.94	3.41	1.35	.17	.01	.011	.04	.04	.02	.004	.0006	.01	-	.0032			
X750	71.02	15.68		8.44	0.85	2.61	.72	.01	.04	.06	.04	.02	.005	.001	.02		.0039			
718A	52.77	18.46	2.90	18.95	5.20	0.96	.61	.01	.036	.02	.01	.01	.005	.0005	.01					
C22	57.50	22.02	14.24	2.64					.008	.04	.01	.03	.007	.0005	.01	.004		3.24	.02	
690	59.33	29.44	0.01	10.38	0.01	0.35	.23		.03	.05	0.15	.009		0.001		.001				.01
310	19.26	24.21	.01	Bal.					.059	.69	1.3	.01	.005	.001						.058
800	32.21	20.21	.3	44.9		.44	.24		.01	.45	.82	.079	.017	.0002	.24					
T92	.12	8.81	.36	Bal.	.08	.01	.01		.0091	.1	.4		.005	.0005	.01			1.78	.18	.046

Samples

Tensile and TEM samples were fabricated from the materials provided through EPRI and made per the standard design used for proton irradiations at the Michigan Ion Beam Laboratory (MIBL) at the University of Michigan. All the samples were machined with the tensile axis oriented in the extrusion or rolling direction. The tensile samples have a square gage section of 2 mm, a gage length of 21 mm and threaded ends, see Figure 3-1. The TEM samples are also rectangular, 20 mm long with a square section of 2 mm, as shown in Figure 3-1. All the samples were mechanically polished with silicon carbide abrasive paper from 360 to 4000 grit then followed by electro-polishing to a mirror finish before use.

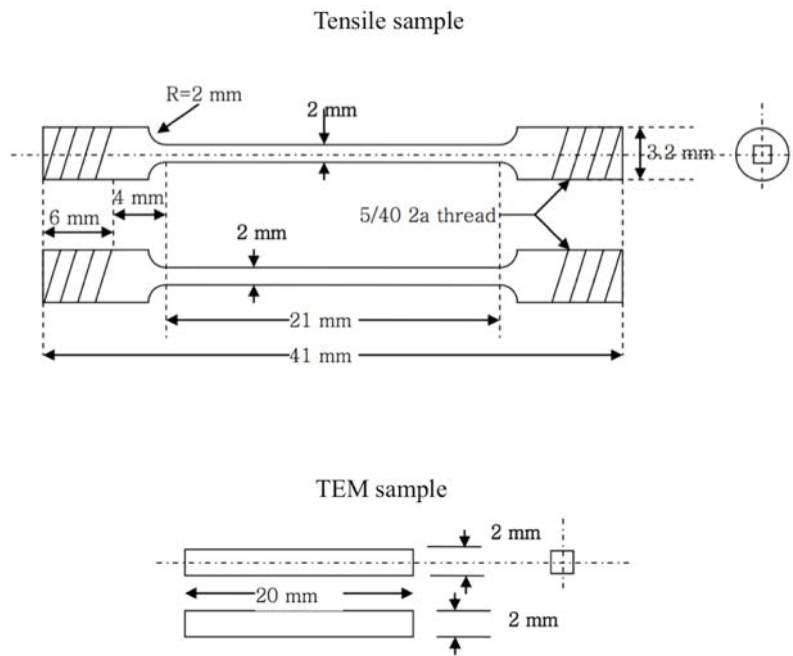


Figure 3-1 Schematic diagram of tensile sample (top) and TEM sample (bottom).

3.2 Sample Preparation for Microstructure Characterization

Specimens with dimensions of $2 \times 2 \times 20$ mm were cut from the as-received (AR) billet using electro discharge machining (EDM). Samples for optical microscopy were prepared by mechanical grinding up to 800 grit, and followed by cloth polishing with $1 \mu\text{m}$ diamond paste, and finally vibratory polishing. The nickel-base alloy samples were electrolytically etched in a solution of 10 g citric acid and 10 g ammonium sulfate per liter of water at 5-10 V and a current density of $\sim 0.01 \text{ A/cm}^2$. The finished samples exhibited a dull golden color. Electron backscatter diffraction (EBSD) specimens were polished using the same procedure followed by electro-polishing in place of etching. The electrolyte solution was a 20 vol.% sulfuric acid in methanol

solution. The polishing was performed at $-40\text{ }^{\circ}\text{C}$ and $\sim 20\text{ V}$ for 30 s. Electron transparent disks were prepared by mechanical grinding of 3 mm disks down to tens of μm . The disks were then perforated in a TenuPol-5 twinjet polisher with the same electropolishing solution at $0\text{ }^{\circ}\text{C}$ and 10-20 V. The irradiated samples are prepared by back thinning of the un-irradiated side to a thickness of around $60\text{ }\mu\text{m}$ with fine grid sand paper to avoid mechanical deformation of the specimens. The irradiated side was then electro-polished to the depth at which observations would be made (typically $\sim 10\text{ }\mu\text{m}$, based on a polishing curve collected beforehand). The as-ground disks were back thinned by twin jet polisher until perforation. Scanning electron microscope (SEM) experiments were performed using an FEI Helios 650 Nanolab system equipped with both Energy-dispersive X-ray (EDX) spectroscopy and EBSD detectors. The EBSD maps were collected with an operating voltage of 20 kV and a working distance of 15 mm. The step size for EBSD collection was typically around $1\text{ }\mu\text{m}$. TEM experiments were performed using JEOL 2010F and JEOL 3011 microscopes operated at 200 kV and 300 kV, respectively.

3.3 Irradiation Experimental Conditions

The proton irradiation experiments were conducted using a 3 MV NEC Tandem accelerator in the Michigan Ion Beam Laboratory (MIBL) at the University of Michigan. Four tensile samples and three TEM samples were irradiated on a specially designed stage, as shown in Figure 3-2. There was one TEM sample on both sides of the stage that served as the guide sample and was not fully irradiated. Four thermocouples were welded on the guide samples, used for calibrating the temperature of the samples. The irradiation area was about 16 mm wide and 8 mm long therefore, only the central part of the samples was irradiated. Both ends of the samples were positioned outside of the irradiation area. A schematic diagram of the stage design is illustrated in Figure 3-3. The cross-sectional view of the stage is shown in Figure 3-4, which shows a heater and an air cooling loop beneath the copper block, which were used to control the temperature of the samples.

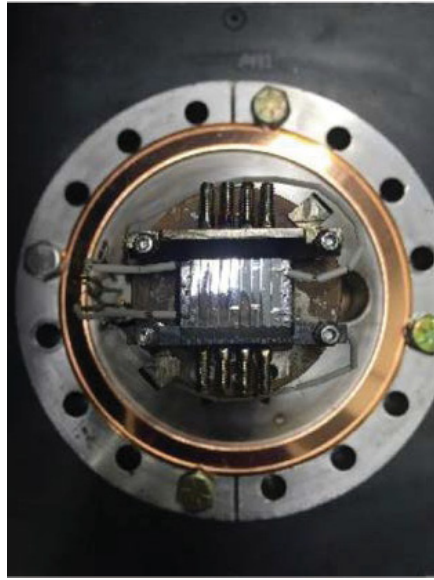


Figure 3-2 Photo of an irradiation stage with tensile and TEM samples (example: Alloy 725 5 dpa irradiation).

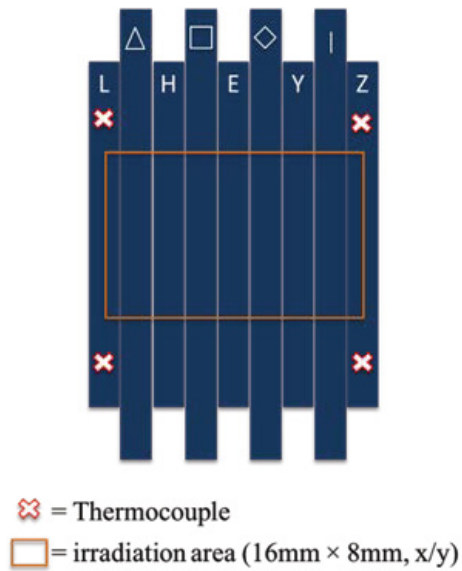


Figure 3-3 Schematic diagram of the irradiation stage (alloy 725).

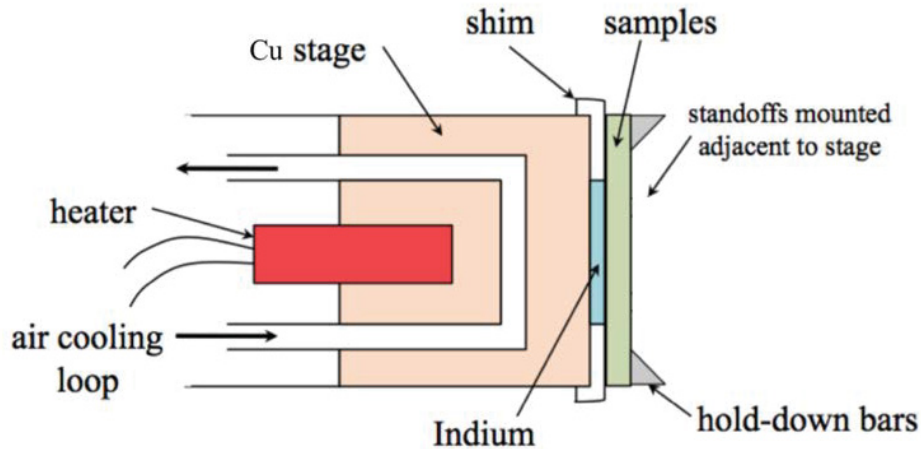


Figure 3-4 Schematic diagram of the cross-sectional view of the irradiation stage.

Irradiations were conducted with 2 MeV protons at a dose rate of about 1.3×10^{-5} dpa/s. The dose and dose rate were estimated using SRIM 2013 (full cascade option) [21]. The resulting damage layer was approximately 20 microns with relatively uniform damage in the first 15 microns. An example of damage profile for Alloy 725 is shown in Figure 3-5.

During the irradiation, infrared thermal images taken by the FLIR[®] camera (A310 Series) were used to monitor the temperature. Throughout the irradiation, the sample temperature was maintained at 360 ± 5 °C. Part of the temperature was due to the proton beam and the rest came from the heater. Before irradiation, the stage was first heated up to 360 °C by the heater, to calibrate the emissivities for the infrared camera. Three ROIs (regions of interest) were selected in the irradiation area on each sample, upper, middle, and bottom, as shown in Figure 3-6. Once the proton beam hits the stage, the temperature increases sharply. The heater and the air cooling loop were adjusted based on the infra-red thermal image to achieve the irradiation temperature of 360 °C. More detailed proton irradiation procedures have been represented elsewhere [22].

Proton irradiation experiments were completed to 5 dpa for alloys Alloy 625, Alloy 625Plus, Alloy 725, and Alloy 625DA during 2014-2015. Alloys 690, alloy 310, 800, X750, C22, and T92 were completed to 5 dpa during 2015-2016. The proton irradiations conducted to date are summarized in Table 3-2.

Table 3-2 Summary of proton irradiation experiments.

Alloys	Date	Final Dose
625	June 2015	5
625Plus	January 2015	4.15
725	April 2015	5
625DA	September 2015	5
T92	February 2016	5
800	March 2016	5
Nickel-base	May 2016	5

Experimental

690	June 2016	5
310	August 2016	5
C22	September 2016	5
X750	Dec.2016	5

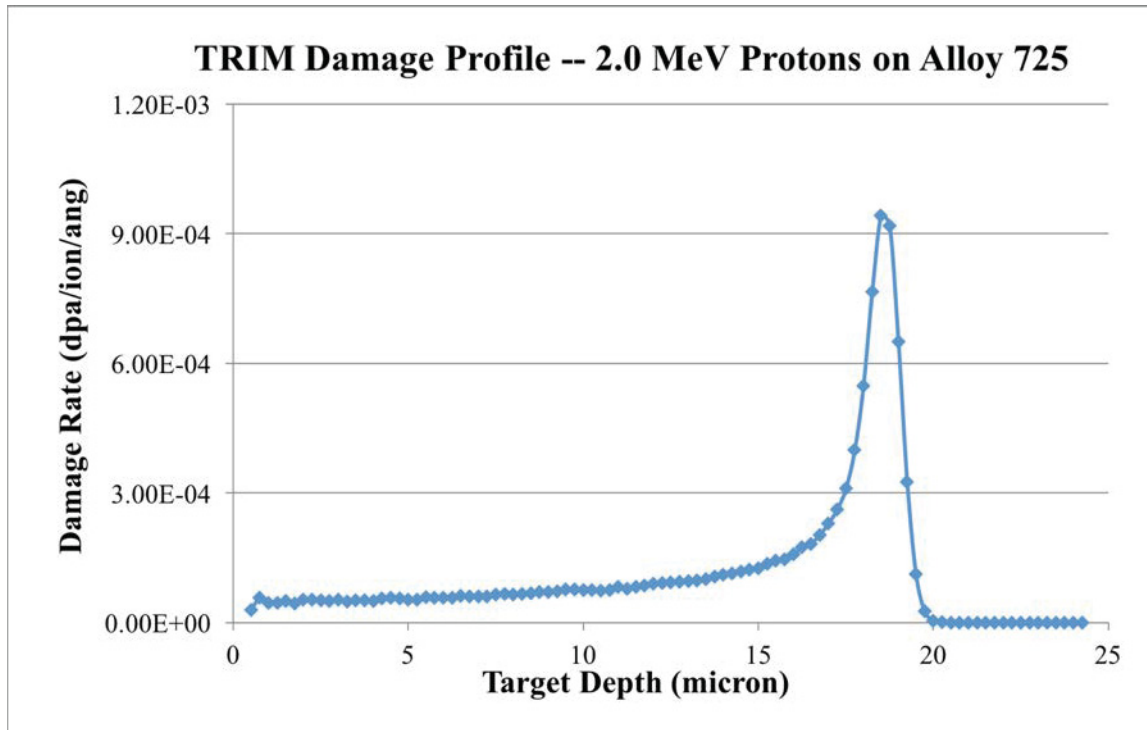


Figure 3-5 Damage profile of alloy 725 under 2 MeV proton irradiation.

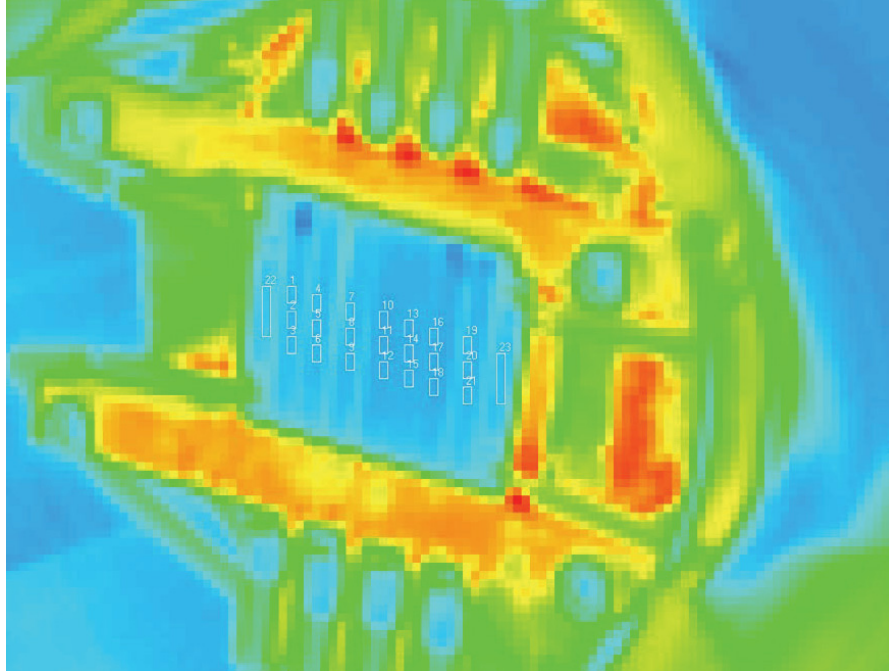


Figure 3-6 Infrared image of the irradiation stage (alloy 625DA).

3.4 Mechanical Properties Tests Conditions

Hardness Measurement

Microhardness was measured using a Vickers Hardness indenter (MICROMET II) with a load of 25 g. This modest load was chosen to confine the plastic zone, ahead of the indenter tip, to a depth within the proton damage range ($\sim 20\mu\text{m}$) to ensure that non-irradiated regions were not being sampled.

Samples used for hardness measurement were the same TEM samples used for proton irradiation. Thus, the polishing procedure was the same as described above. To evaluate the hardness changes due to irradiation, the hardness of the samples was measured at a load of 25 g before and after irradiation. Thirty indentations were made at each condition to ensure statistically relevant results. An average and standard deviation were determined for each condition.

Tensile Test at Room Temperature

Tensile tests at room temperature were performed using MTS Machine (TR/50) and extensometer (MTS 634.12F-24) in the Irradiated Materials Testing Laboratory (IMTL) at the University of Michigan. The aim of the test was to obtain information about the mechanical properties of the alloys. The tensile test was conducted at a strain rate of $1 \times 10^{-4} \text{ s}^{-1}$ to failure at room temperature.

3.5 CERT System and Test Procedure

Constant Extension Rate Tensile (CERT) tests were performed using the CERT I and CERT II systems in the High Temperature Corrosion Laboratory (HTCL) at the University of Michigan. CERT I and CERT II systems share the same design and are capable of straining four samples in parallel providing identical conditions within a given test, respectively. The CERT I system is assigned to BWR-NWC environment and CERT II PWR-PW environment.

The CERT experiments were conducted in a 4 liter autoclave connected to a flowing water loop, fed from an external water column where gasses were added. The systems used a mechanical pump, heater, back pressure regulator (BPR), and sensors to measure conductivity and dissolved oxygen on the inlet and outlet sides of the autoclave. The water loop consisted of two water columns (the secondary column replenishes the primary column). Water flowed from the primary column, where gas can be bubbled to achieve the desired dissolved oxygen or hydrogen concentrations and where water conductivity and dissolved oxygen content was recorded before entering the high-pressure pump. Before water entered the autoclave, it passed through a heat exchanger and pre-heater. Once inside the autoclave, the water was heated by resistive heaters located outside the autoclave and controlled by a thermocouple inside the autoclave (288°C for CERT I system and 320 °C for CERT II system). As water exited the autoclave, it passed through the heat exchanger, and then through a tube-in-tube chiller system. The BPR controlled the pressure inside the autoclave. The water pressure was reduced after passing through this regulator. The conductivity and dissolved oxygen (DO) concentration of the water were measured on the low-pressure side of the loop. Subsequently, the water flowed through an ion exchange resin filter, a sub-micron filter, and back into the primary water column. For the PWR-PW CERT II system, an ion exchange resin filter saturated with boron and lithium ions was installed in the loop so that the required concentrations of B/Li (e.g. 1000 ppm B and 2 ppm Li) were maintained while other impurities were removed. A schematic of the CERT II system is shown in Figure 3-7.

A stepper motor was used to strain the tensile samples at a constant displacement rate. It was controlled by digital outputs from a PC-monitoring system. The crosshead displacement was measured using a linear variable differential transducer (LVDT) with a resolution of 0.5 μm . Each of the pull rods were sealed at the feed-through into the autoclave with a self-energizing graphite seal with an internal spring that expanded under pressure. Each pull rod was connected to a Type 316L stainless steel sample loading fixture. Electrical insulation was provided by zirconia washers located in the loading fixtures. After the test specimens were loaded, the autoclave body was sealed by the autoclave head.

CERT experiments were conducted at a strain rate of $1 \times 10^{-7} \text{ s}^{-1}$ in either simulated BWR-NWC or PWR-PW environments to about 4 % plastic strain. The conductivity, oxygen content,

hydrogen content, and B and Li concentrations were chosen to be representative of both reactors cores, as listed in Table 3-3.

Another CERT test was conducted using an inert Argon gas environment at high temperature. The test design was very close to the CERT I and CERT II systems, similar in heating and straining setups. Instead of flowing water, Ar gas was continuously flowing into the autoclave to avoid the presence of oxygen. The specific conditions are listed in Table 3-3.

3.6 Characterization of Cracking Susceptibility

After the CERT test, each tensile sample was characterized in an SEM (JEOL JSM-6480) to determine the surface morphology and cracking susceptibility:

- Low magnification images were taken throughout the tensile sample surfaces to get general information about the sample.
- Higher magnification images were taken of specific features, such as cracks or precipitates, etc.
- Intermediate magnification images were taken of three random areas in both irradiated and non-irradiated regions for statistical counting of the cracking behavior.

Based on the information generated, a comparison of cracking susceptibility among the different alloys could be measured.

Table 3-3 Conditions of CERT test for simulated BWR (NWC) and PWR environments, and Ar environment.

Parameter	BWR (NWC)	PWR	Inert gas (Ar)
Temperature (°C)	288	320	320
Pressure (psi)	1500	2000	20-30
Inlet Conductivity (μS/cm)	< 0.1	20-30	-
Outlet Conductivity (μS/cm)	< 0.1	30-30	-
O ₂ Concentration (ppb)	2000	< 5	-
H ₂ Concentration (cc/kg)	-	35	-
[B] (ppm)	-	900-1100	-
[Li] (ppm)	-	2-3	-
pH at 25°C	7.0	6 – 6.7	-

Experimental

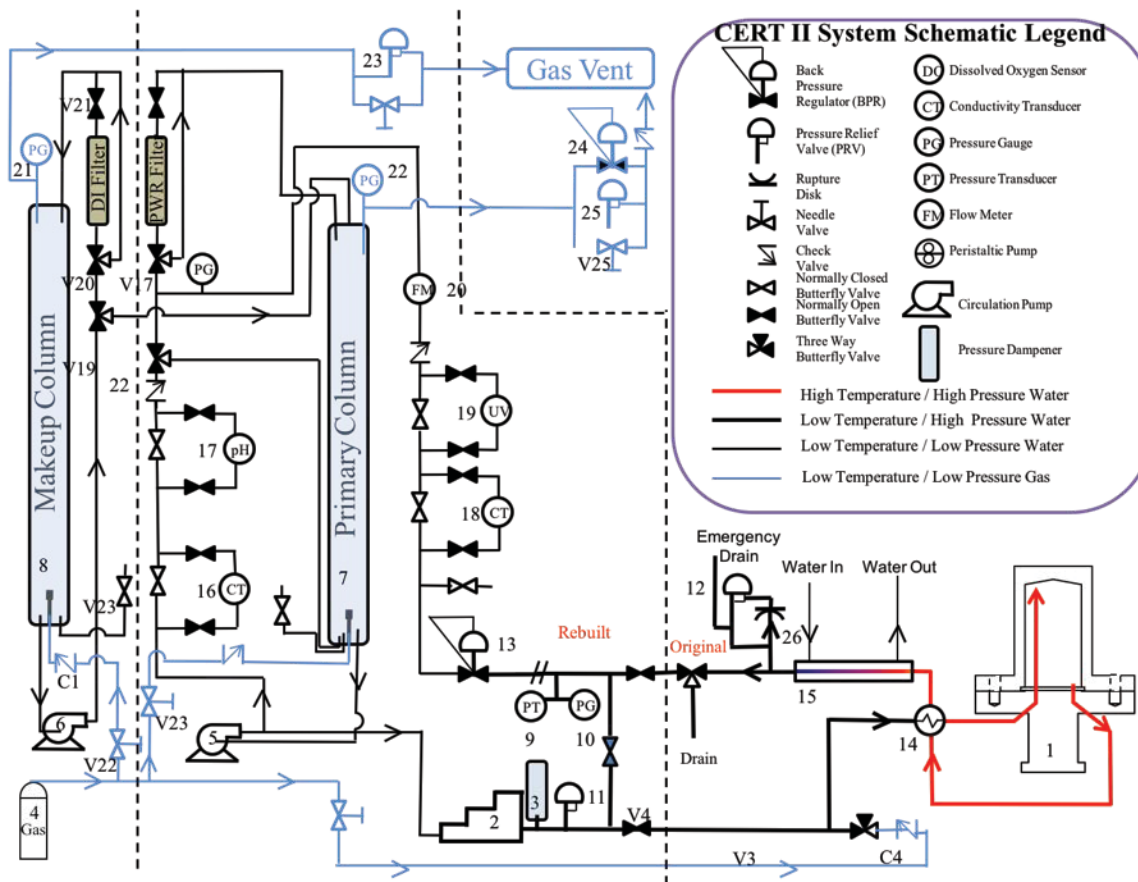


Figure 3-7 A schematic design of CERT (CERT II - PWR) test system.

3.7 Three Point Bend Test System and Procedure

In order to assess the relative ductility of the various alloys, Three point bend tests will be performed using a custom holder for the IMTL MTS RT/50 testing system. This holder is composed of interconnecting support and loading fixtures that pin and bend individual samples when the tester crosshead is raised, similar to a previously used four point bend test design [23]. Sample loads are measured by a load cell connected to the MTS system, while the center displacement of the sample is measured to a resolution of 0.6 μm by a LORD MicroStrain HSG-DVRT-6 differential variable reluctance transducer (DVRT). (DVRTs are a miniaturized variant on LVDT designs.) Analog signals from the load cell and DVRT are synchronized and recorded by a PC-monitoring system for later analysis. Components of the holder that contacted the samples was made from age hardened alloy 718 to prevent wear, and the three edges (“points”) that bend samples were rounded to a radius of 0.2 mm to prevent indentation. Drawings of the holder are shown in Figure 3-8.

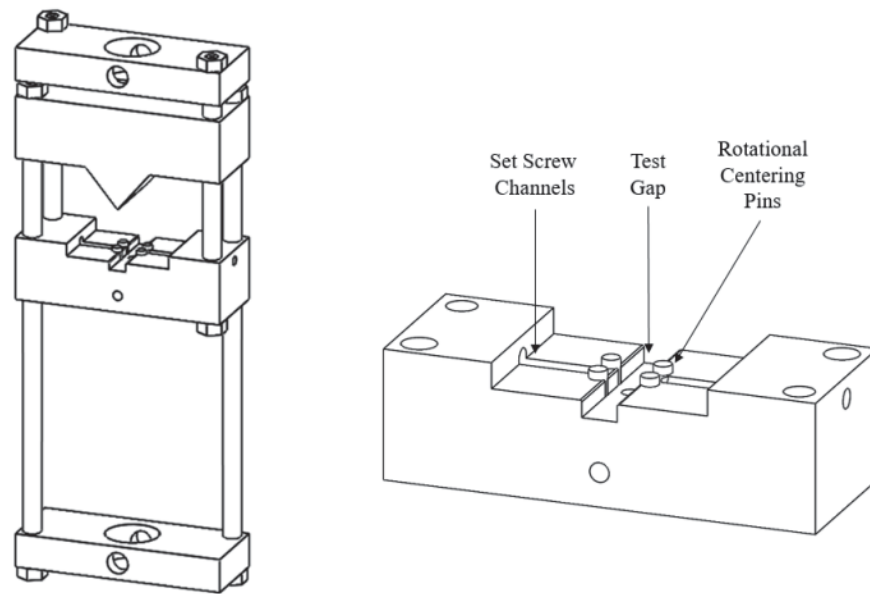


Figure 3-8 Custom three point bend test holder, with additional detail of the support plate.

Testing was conducted with incremental straining followed by SEM examinations. Each sample was first mounted between support plate pins to prevent rotational misalignment and centered above the test gap using brass tipped set screws. The MTS crosshead was then raised under manual control until the loading wedge approaches within 1 mm of the sample back surface. Then the DVRT probe is brought into contact with the sample test surface. Contact between the sample and the wedge were made automatically by the MTS system, to a 0.3 N load. Immediately before starting the test, the load and displacement measurements were zeroed and the set screws retracted from the sample. The automated testing proceeds at a crosshead displacement rate of 0.1 mm/min to the desired increment of sample strain, before unloading at the same crosshead displacement rate. Test surface imaging occurred between strain increments using the JEOL JSM-6480 SEM at IMTL. Intermediate to high magnifications were used identify nascent cracks, and thus calculate the relative ductility of samples.

4 RESULTS

4.1 Irradiation Experiments

During each irradiation, various experimental parameters were recorded. The following results are from the proton irradiation of alloy 690 to a dose of 5 dpa and are used as an example of the data recorded. Pressure of the entire beam line is plotted in Figure 4-1, and beam current is shown in Figure 4-2. Temperature histograms of each sample are plotted in Figure 4-3.

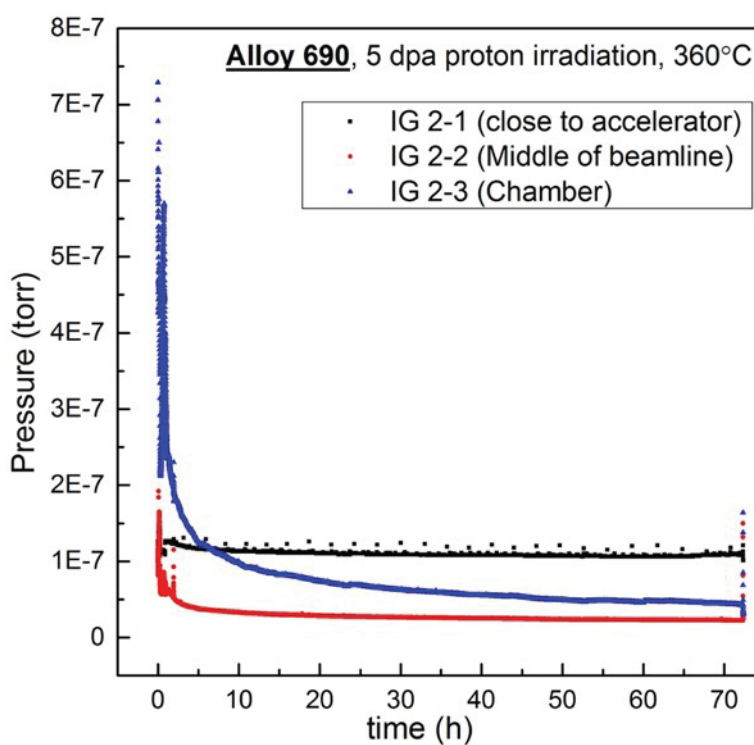


Figure 4-1 Pressure of the beam line during the Irradiation of alloy 690 to a dose of 5 dpa.

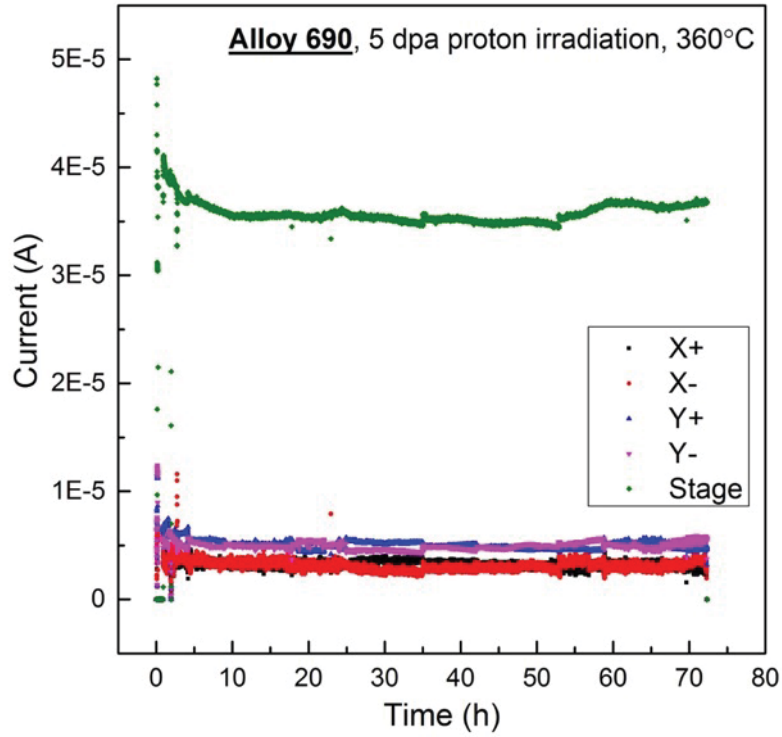
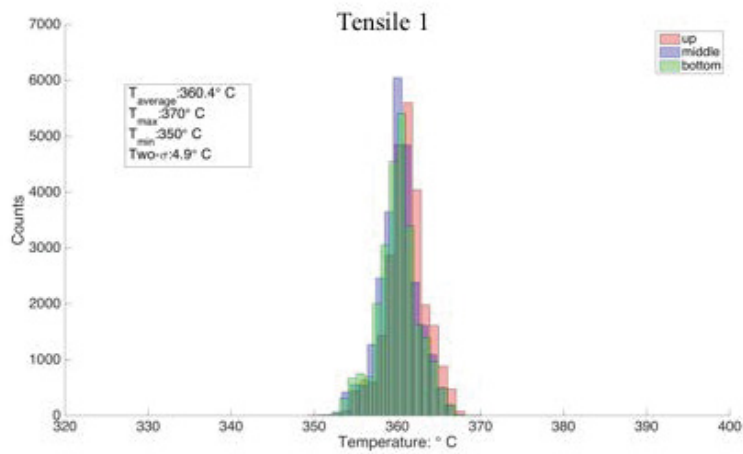
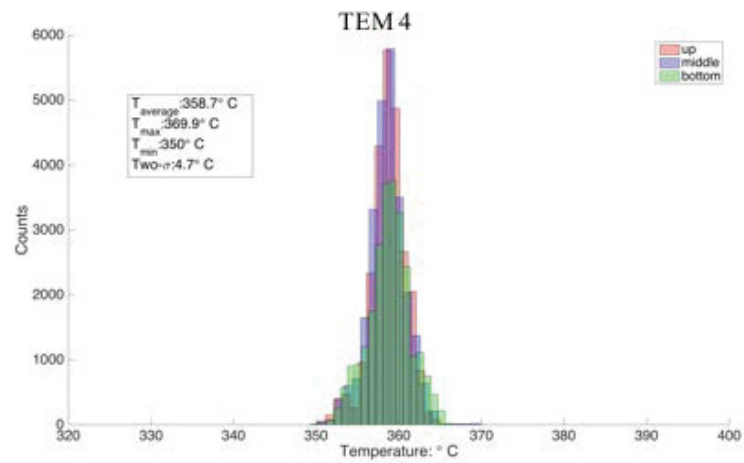
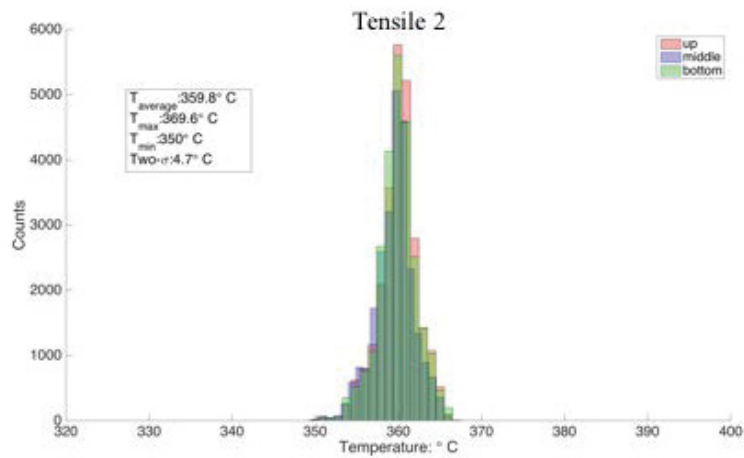
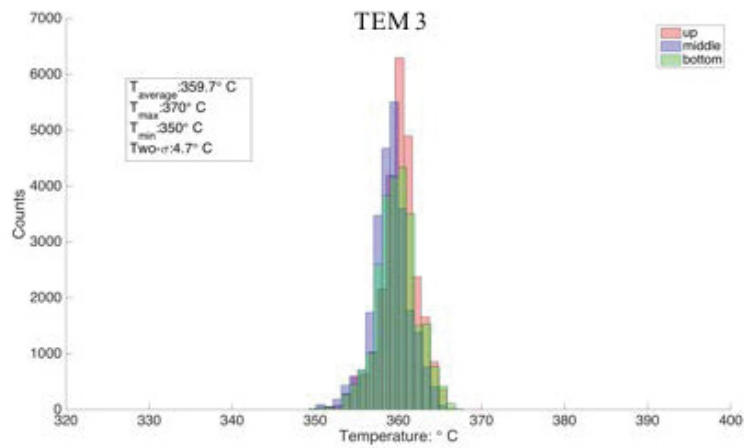


Figure 4-2 Current of the irradiation of alloy 690 to a dose of 5 dpa.



Results



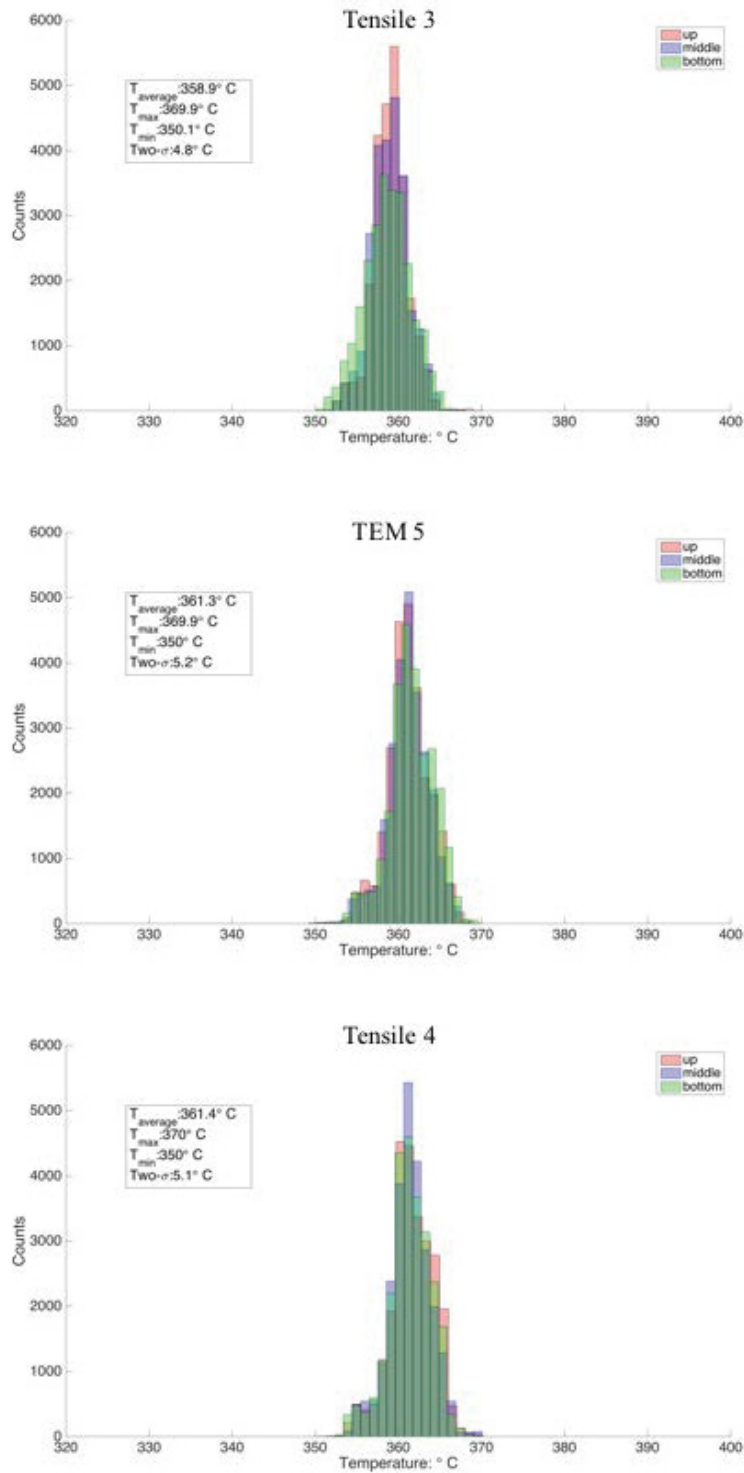


Figure 4-3 Temperature history diagrams for 4 tensile bars and 3 TEM bars of alloy 690 during the irradiation to a dose of 5 dpa.

The pressure of the chamber where the stage was located was between 10^{-7} and 10^{-8} torr. Under this high vacuum, no oxide was formed on the surface of the sample during the irradiation. The

Results

total beam current was around 50 μA , which was the maximum stable beam current that was achieved by the accelerator. About two-thirds of the beam, about 30 – 35 μA , was on the stage with the balance on the slits. This ensured that the samples were fully irradiated during the raster-scanning process. The temperature histogram showed the temperature distribution of three different positions located in the irradiation area of each sample. Generally, it follows a normal distribution, and the three positions: upper, middle, and bottom, were overlapped with each other. The average temperature for each sample was around 360 $^{\circ}\text{C}$, and the standard derivation value is less than 5 $^{\circ}\text{C}$. Thus, it ensured that the proton irradiation was well performed with maximum current under high vacuum at 360 ± 5 $^{\circ}\text{C}$.

The beta counting was conducted for each sample after irradiation to confirm that the samples were irradiated uniformly. The bar diagram of beta counting of the irradiation of alloy 690 to a dose of 5 dpa is shown in **Figure 4-4**. Guide samples (in grey) were not fully irradiated, thus they had lower beta counts. Four tensile and three TEM samples (in red) in the middle of the stage had very close beta counts, indicating that they were fully and uniformly irradiated.

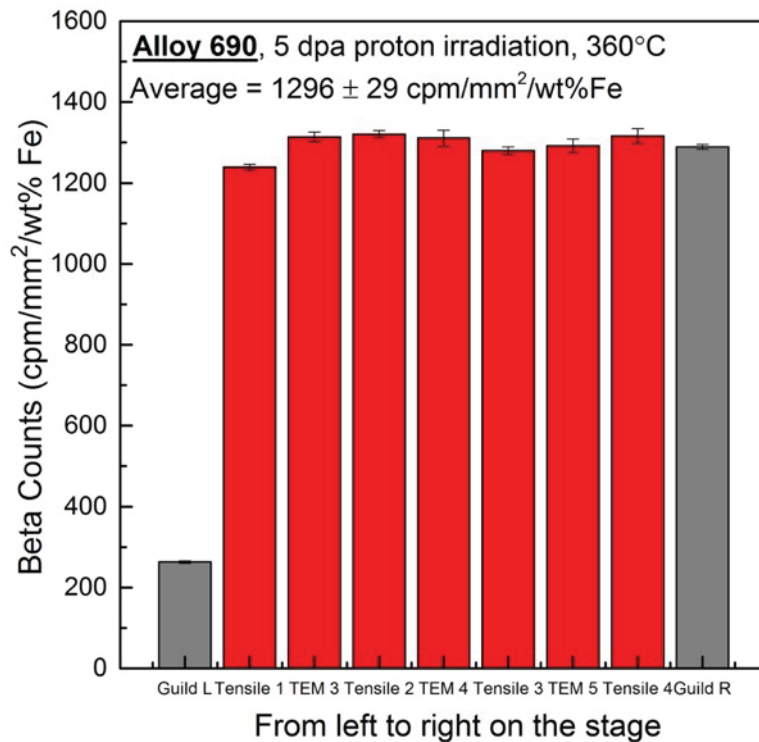


Figure 4-4 Bar diagram of beta counting of each sample after irradiation of alloy 690.

4.2 Microstructure Pre-characterization

The microstructure pre-characterization involves the grain size, grain boundary character, and precipitates identification. Previous results were limited to the alloy 625, 625Plus, 625DA and alloy 725. New results are summarized together with previous results. The grain boundary chemistry characterization of selected alloys will be reported in the radiation induced segregation session.

The average grain sizes of these alloys are listed in Table 4-1. Alloy 625Plus and alloy 718 have the largest average grain size while the average lath size of T92 is the smallest. Among the nickel-base alloys, alloy 625DA has the smallest average grain size of about 10 μm . Austenitic stainless steels typically have a grain size of tens of micrometers. Alloy 310 has a small grain size compared to that of alloy 800.

Table 4-1 The average grain size of as-received materials

Alloy ID	Grain size (μm)	# of grain involved
625	40 \pm 17	221
625Plus	120 \pm 87	223
625DA	12 \pm 7	365
725	60 \pm 32	366
718A	114 \pm 9	200
310	22 \pm 13	372
690	86 \pm 56	120
800	62 \pm 38	110
T92	0.56 \pm 0.54	1080

Table 4-2 Grain boundary character based on EBSD measurements

ID	LAGB		HAGB		Special GB		Random High angle		Area Analyzed (μm^2)
	L (μm)	Fraction %	L (μm)	Fraction %	L($\Sigma 3 + \Sigma 9$)	Fraction %	L (μm)	Fraction, %	
625	565.8	2.1	26,000	97.9	16,808+1,228	67.9	7,964	30	90,530
625Plus	743	1.1	67,800	98.9	50,117+2,369	76.6	15,314	22.3	1,012,842
625DA	229	2.8	7,990	97.2	4,021+209	51.5	3,760	45.7	13,457
725	506	2	24,900	98	16,414+512	66.6	7,974	31.4	235,292
718A	3290	7.2	42,200	92.8	21,300+186	47.2	20,714	45.6	1,005,235
310	867	4.5	18,700	95.5	8,830+197	46.2	9,673	49.3	50,388
690	2,352	8.6	25,000	91.4	13,100+432	49.3	11,468	42.1	276,049
800	945.1	2.5	36,400	97.5	22,500+1,760	65.1	12,140	32.4	389,518
T92	3,970	40.1	5,920	59.9	N/A	N/A	5,920	59.9	46,737

LAGB: low angle grain boundary, grain boundaries lower than 15°

HAGB: high angle grain boundary, grain boundaries larger than 15°

N/A: not applicable

The EBSD maps of alloys 690, 800 and 310 as shown in Figure 4-5 are similar to that of the nickel-base alloys presented in the previous report, which mainly contain large grains with annealing twins. Unlike the nickel-base alloys, T92 shows a hierarchical microstructure including prior austenite grain boundaries and lath boundaries. Low angle grain boundaries are prevalent in this material, constituting 40% of the total grain boundaries. The grain boundary

Results

characters of all alloys are listed in Table 4-2. TEM observation shows that the microstructure of the as-received austenitic alloys 310, 800 and 690 are free of intragranular precipitates. However, GB carbides are frequently observed as shown in Figure 4-6. In contrast, within the lath of T92, there are usually sub-boundaries with similar orientation as shown in Figure 4-7. Carbides are located at the lath boundaries and PAGBs. These carbides are presumably $M_{23}C_6$. No nano-scaled (NbC) carbides were observed in current heat of T92 steel. The statistical results of inter-lath distance and particles size are shown in Figure 4-8. The average value of inter-lath distance is 560 nm using the linear interception method with 500 laths.

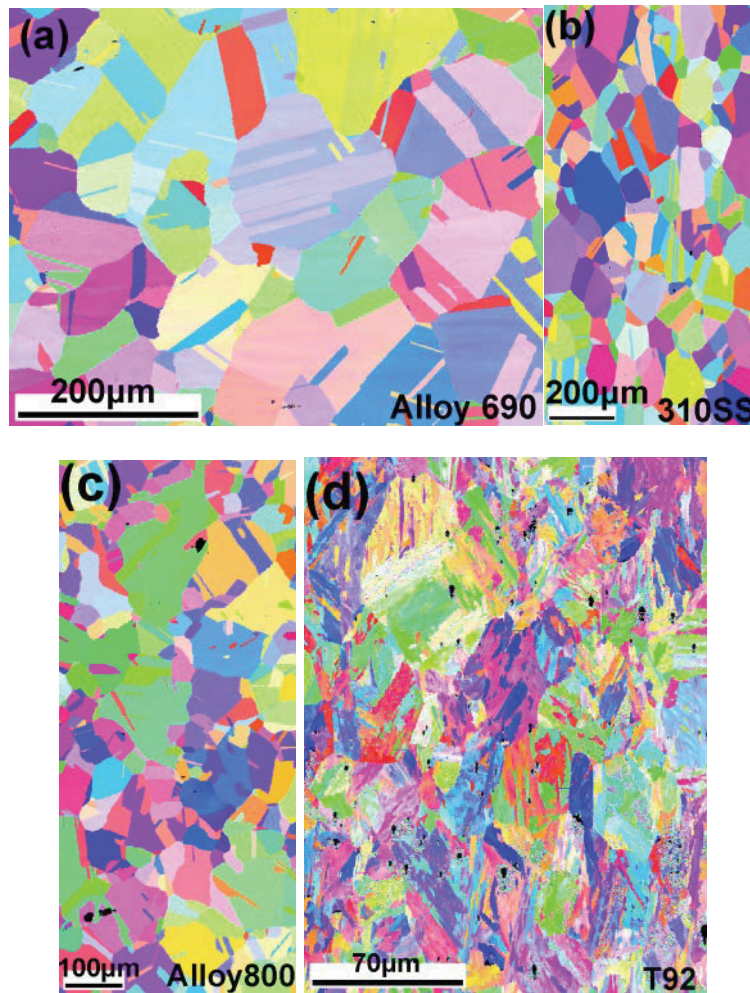


Figure 4-5 Orientation imaging maps (OIM) of (a) alloy 690 (b) alloy 310 (c) alloy 800 and (d) T92

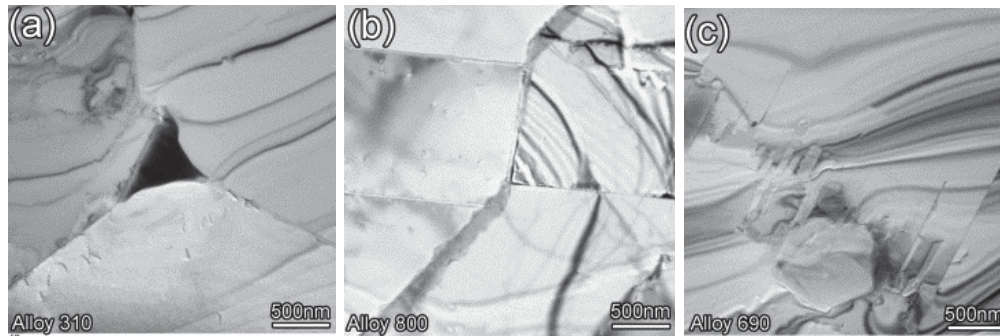


Figure 4-6 Bright field images of (a) alloy 690 (b) alloy 310 and (c) alloy 800 showing the presence of carbides

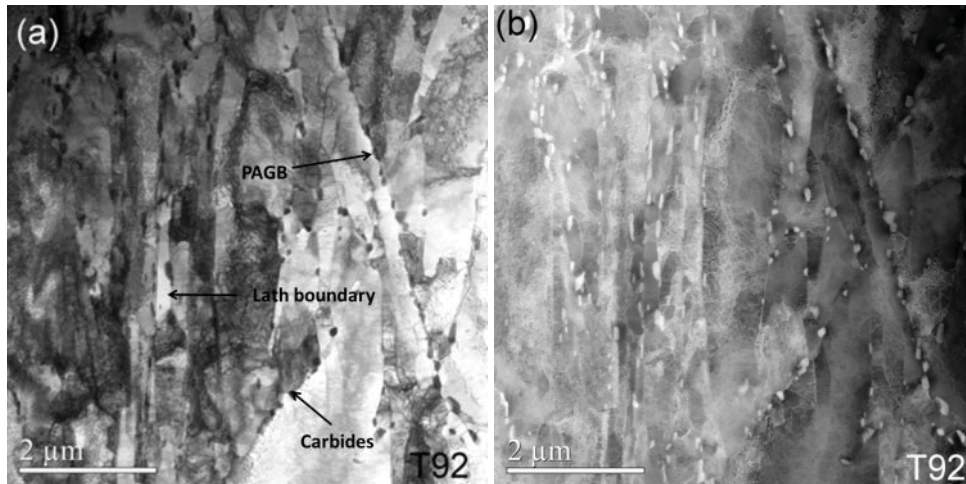


Figure 4-7 (a) TEM image and (b) STEM image show the lath structure of T92 steels. Carbides are frequently observed within the lath boundaries or at the PAGBs which are black particles in TEM mode and white dots in STEM image.

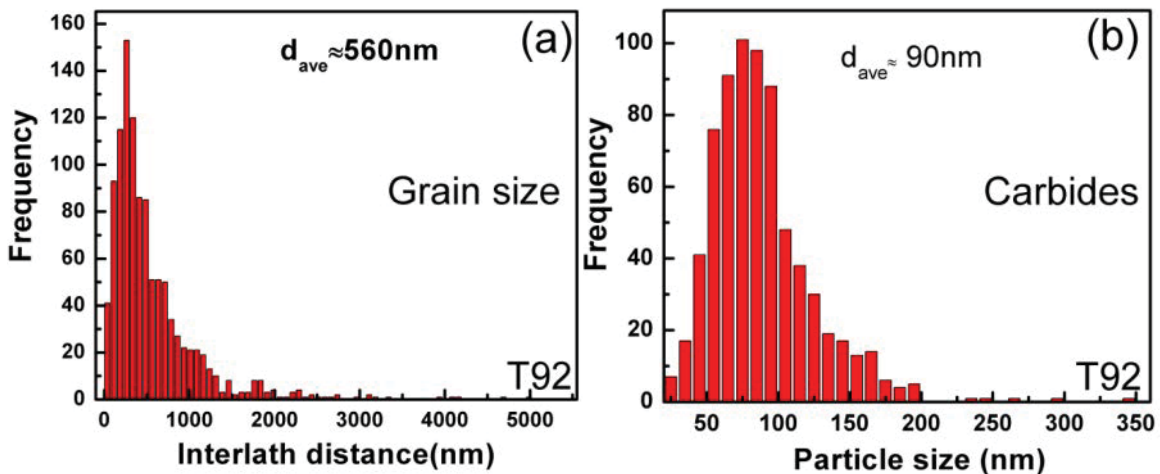


Figure 4-8 Statistical results of (a) inter-lath distance and (b) carbides particles size in T92 steel

4.3 Deformation structure of nickel-base alloys

In the previous report, the mechanical properties of alloy 625, 625Plus, 625DA and alloy 725 were tested. In this report, the deformation microstructures of precipitate hardened nickel-base alloys were studied to characterize the dislocation - particle interaction, which could further shed light on the work hardening behavior and deformation mechanism of irradiated materials.

In deformed specimens, such as that shown in Figure 4-9, the annealing twin boundary (TB) cannot be identified using the Brandon's criterion [24] ($\Delta\theta \leq 15\Sigma - 1/2$). Beside the rotation angle, significant deviation of the twin plane also occurred during deformation. Misorientation is developed within a grain after deformation while it is negligible before deformation. Deformation twinning was challenging to identify using EBSD due to their small size relative to the step size.

Planar slip prevailed in the deformed specimens in all the nickel-base alloys as shown in Figure 4-10. Both primary and secondary slip bands were activated in most of these alloys. In 625Plus, the slip bands and GB interaction were captured where the slip bands in the bottom grains met the GB, and activated slip in the upper grain. Deformation twinning was occasionally observed as shown in Figure 4-11. More interestingly, slip band-precipitate interaction was observed. In alloy 625Plus, precipitate free channels were observed in two 110 directions as shown in Figure 4-11a-d. The channels resulted from consecutive cutting of precipitates by glissile dislocations. Deformation twinning can also create a precipitate free channel as shown in alloy 625DA in Figure 4-11e-h. In alloy 718, the stacking faults as part of an extended dislocation were imaged. No evidence was observed that the particles were cut by the stacking fault in alloy 718 in Figure 4-11i-l. However, in alloy 725, particles were cut by the partial dislocation as marked in the white arrows in Figure 4-11m-p.

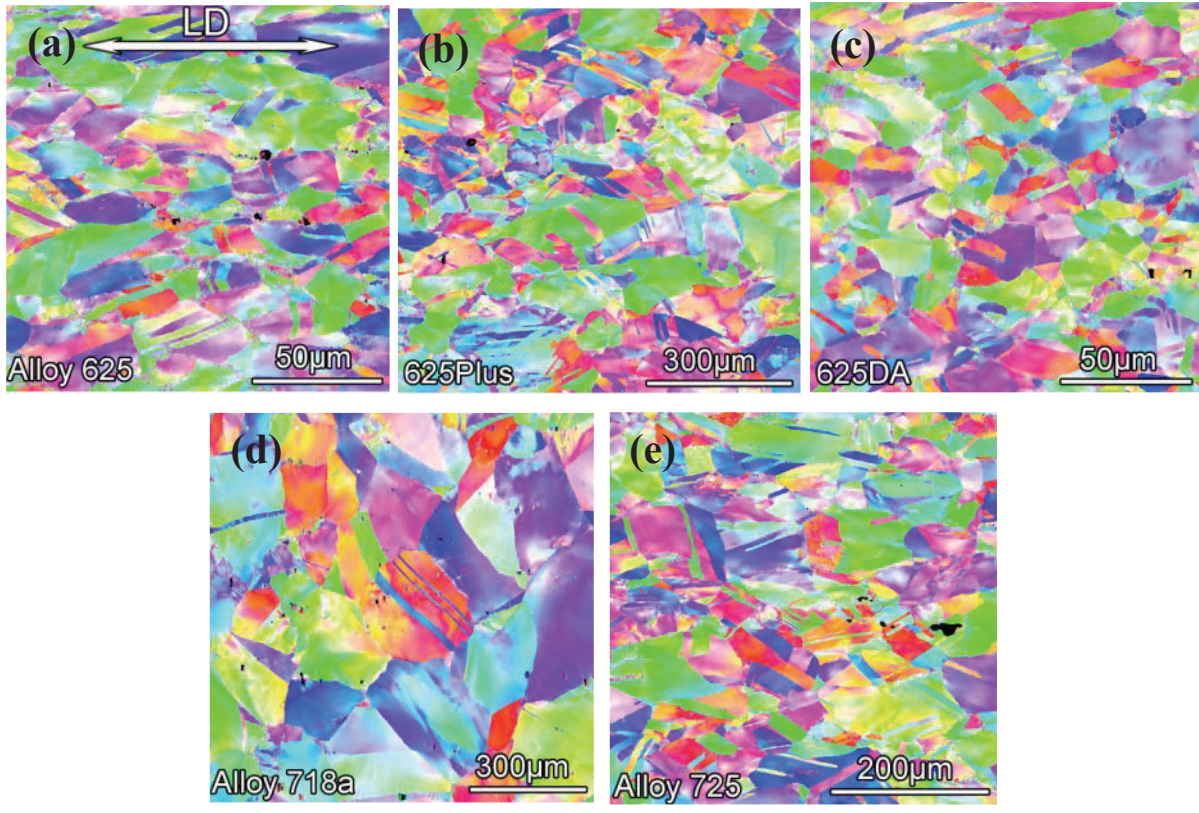


Figure 4-9 OIM maps of deformed structure (a) Alloy 625 (b) alloy 625Plus (c) alloy 625DA (d) alloy 718A and (e) alloy 725. Loading direction is marked by the arrow in (a). Misorientation was developed within the grains.

Results

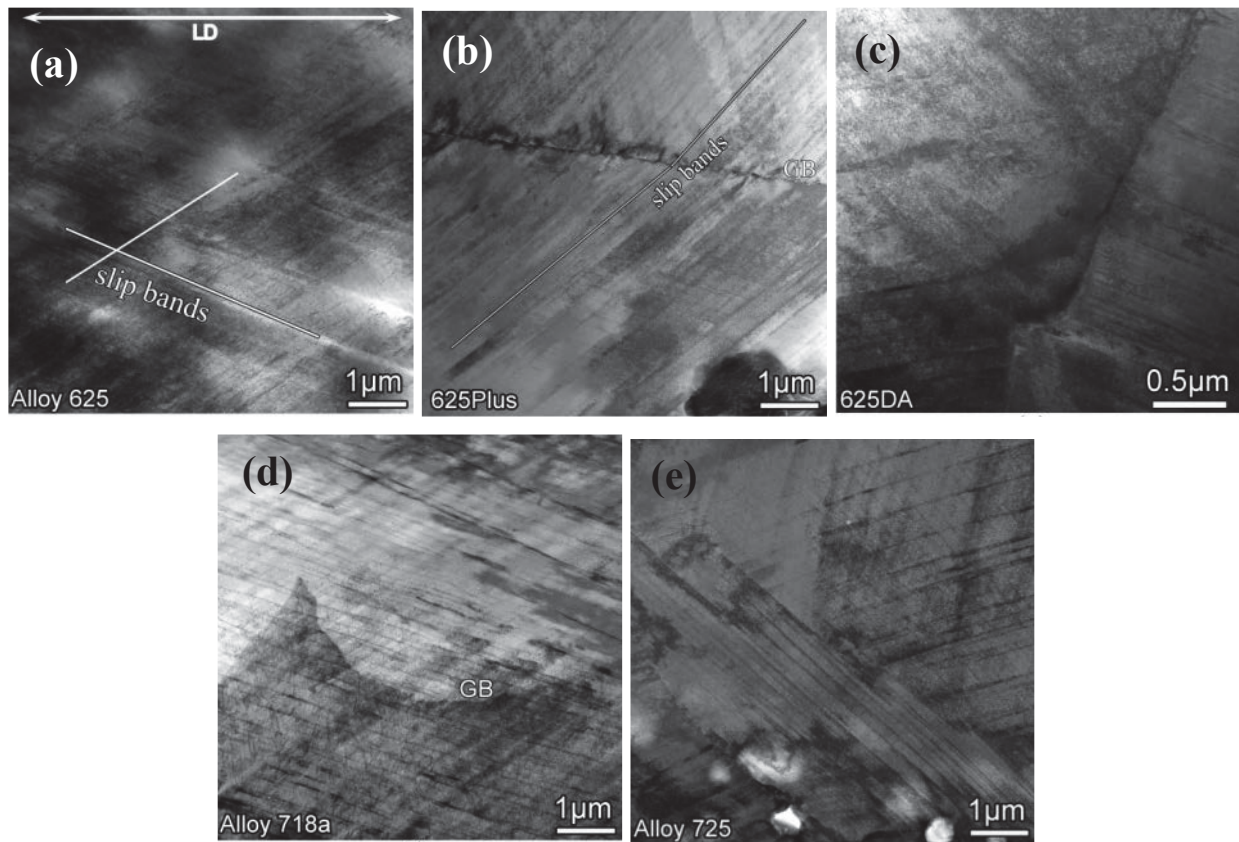


Figure 4-10 Planar slip in deformed nickel-base alloys (a) Alloy 625 (b) alloy 625Plus (c) alloy 625DA (d) alloy 718a (e) alloy 725. Loading direction is marked by the arrow in (a).

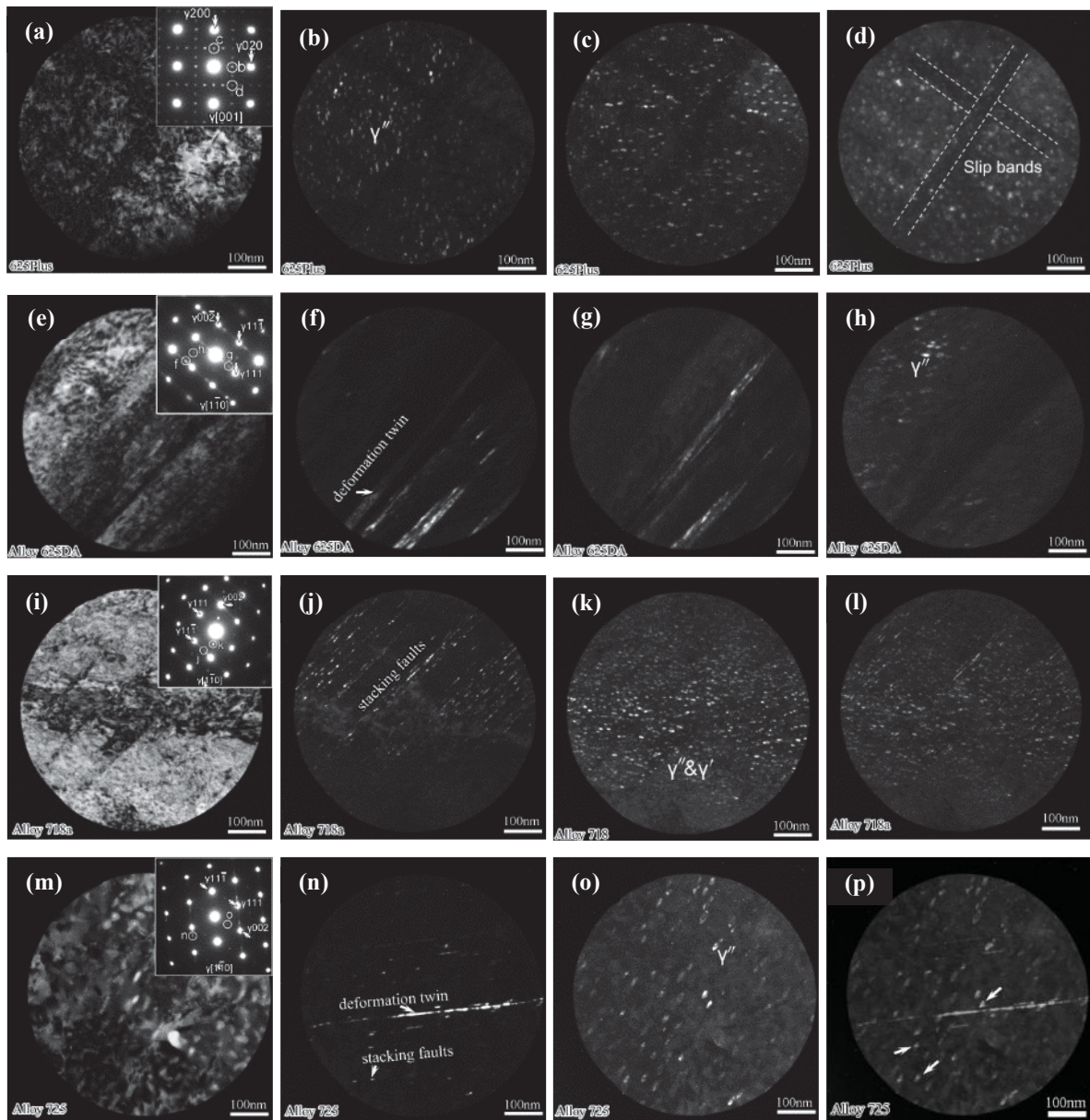


Figure 4-11 Dislocation and particle interaction in nickel-base alloy 625Plus (a-d), and 625DA (e-h), 718a (i-l), and 725 (m-p).

4.4 Microstructure Characterization of Irradiated Alloys

The microstructure of an irradiated alloy generally includes dislocation loops, irradiation induced or enhanced precipitates, voids, and radiation induced segregation. Table 4-3 summarizes the irradiation induced features observed in the alloys examined. The long range ordered (LRO) phase, loops and voids in alloy 625, 625Plus, 625DA and 725 were reported in a previous report [1]. The RIS results are reported here for the first time. All the data related to alloys 690, 310 and 800 are new.

Table 4-3 Microstructural features characterized in the irradiated alloys

Alloy ID	Microstructural features of irradiated materials			
	Irradiation induced precipitates	Loops	Voids	RIS
625	LRO	Y	N	Y
625Plus	LRO	Y	N	Y
625DA	LRO	Y	N	Y
725	LRO	Y	N	Y
690	LRO+ γ'	Y	N	Y
310	ND	Y	Y	Y
800	γ'	Y	N	Y

LRO: long range order phase, Ni₂Cr type precipitate. ND: not detected. TBD: to be determined. N: not observed. Y: observed.

Dislocation Loops

The size of dislocation loops of alloy 625, 625Plus, 625DA and alloy 725 have been summarized in a previous report [1]. Among those alloys, alloy 625DA contained the smallest loops while alloy 725 had the largest. More generally, Figure 4-12 shows a typical TEM rel-rod image of dislocation loops in alloy 800, which are the largest of all the alloys investigated. All the loops are inclined in the same direction as all of them share the same habit plane. The size distributions of loops for different alloys are shown in Figure 4-13. The smallest loops were observed in alloy 625DA. The loops with the largest average size were observed in alloy 800. Nickel-base alloy 625 and its derivatives show a similar size of dislocation loops of around 20 nm. The average loop size in austenitic stainless steel 310 is also around 20 nm. The loop density is on the order of $10^{21}/\text{cm}^3$ in alloys 690 and 800. The loop density in alloy 625DA is on the order of $10^{23}/\text{cm}^3$, which is the highest among all the alloys observed. Meanwhile, the loop density is around $10^{22}/\text{cm}^3$ in all the other alloys.

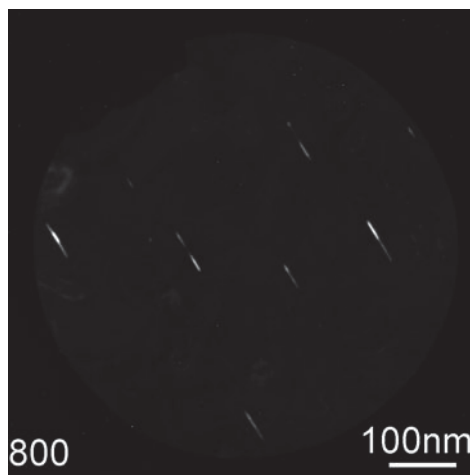


Figure 4-12 Faulted loops in alloy 800. These loops are observed using the rel-rod method. The alloys are irradiated at 360°C to around 5 dpa using protons.

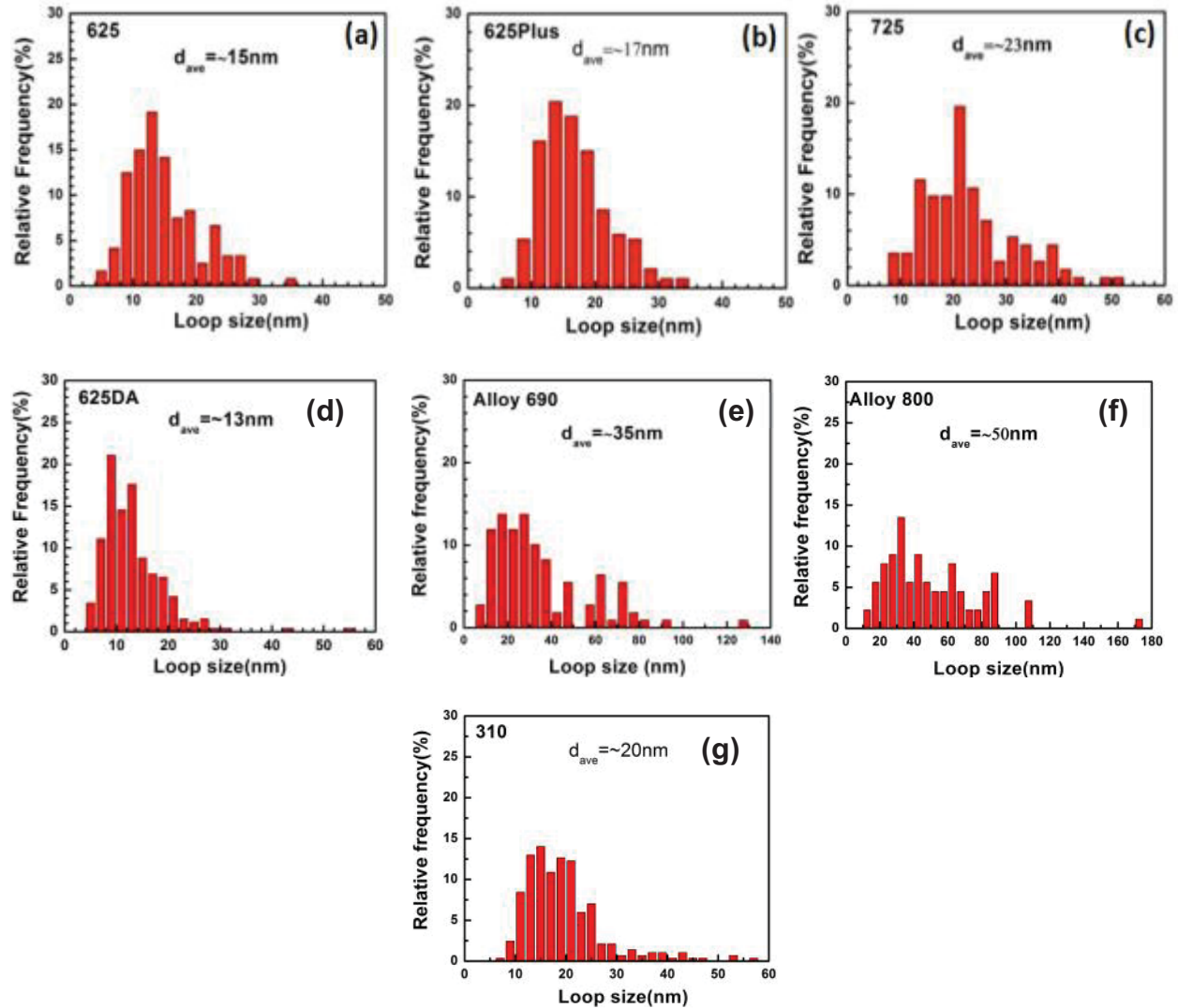


Figure 4-13 Statistical study of the dislocation loops in (a) alloy 625 (b) alloy 625 Plus (c) alloy 725 (d) 625DA (e)690 (f)800 and (g) 310. The largest loop size occurs in alloy 800. These alloys were irradiated at 360 °C to about 5 dpa by protons.

Irradiation Induced/Enhanced Precipitation

Irradiation Enhanced Long Range Ordered (LRO) Phase

LRO phases were observed in alloy 625, 625Plus, 625DA and 725 previously, with the largest size in alloy 725 and highest volume fraction in alloy 625 and 625DA. Here, the observation of LRO phases extends to alloys 690, 718 and 800 as shown in Figure 4-14. As the Fe content increases, the diffraction spots of the LRO phase become weaker. In alloy 718, no diffraction spot can be identified related to the LRO phase. As the alloy composition becomes iron rich, the γ' phase forms as, for example, in Alloy 800.

Results

Regarding the LRO phase, the key for the diffraction pattern is shown in Figure 4-14h. Three variants of the LRO phase were observed and only a single variant of γ'' phase can be observed. There are six variants in total for the LRO phase and they cannot be observed in a single zone axis. The six variants are defined according to their orientation relationship with the matrix: variant 1 $(001)[110]_M // (001)[100]_{Ni_2Cr}$, variant 2 $(001)[1-10]_M // (001)[100]_{Ni_2Cr}$, variant 3 $(001)[011]_M // (001)[100]_{Ni_2Cr}$ and variant 4 $(001)[0-11]_M // (001)[100]_{Ni_2Cr}$, variant 5 $(001)[101]_M // (001)[100]_{Ni_2Cr}$, and variant 6 $(001)[10\ 1]_M // (001)[100]_{Ni_2Cr}$. Among different alloys, a bias of these LRO phases was observed in the selected area diffraction pattern (SADP) shown in Figure 4-14a. According to diffraction theory, the intensity of the diffraction spots relative to transmission spots can be an indicator of the relative amount of each phase. It was apparent that the diffraction spots of three variant were not of the same intensity. The precipitation of LRO phase showed equality among variants in alloy 725 and alloy 690 and bias precipitation among variants in alloy 625Plus, 625DA and alloy 625. This effect is still not well understood and further effort is needed to unfold the underlying mechanism.

Size distributions for the LRO phase in the various alloys are shown in Figure 4-15. Larger precipitates were observed in alloy 725, alloy 625DA and alloy 690. Smaller sizes of LRO phase were observed in alloys 625 and 625Plus. The difference in size of precipitates for alloy 625 and 625Plus was insignificant. It should be noted that for alloy 725 the LRO phase is coherent with the matrix with an irregular shape as shown in Figure 4-16. The final size of these irradiation-induced precipitates is determined by the dynamic balance of irradiation-induced displacement and irradiation enhanced diffusion processes. It shows that the size varied with chemical composition of alloys while the influence of other intrinsic properties of the alloy is an open question.

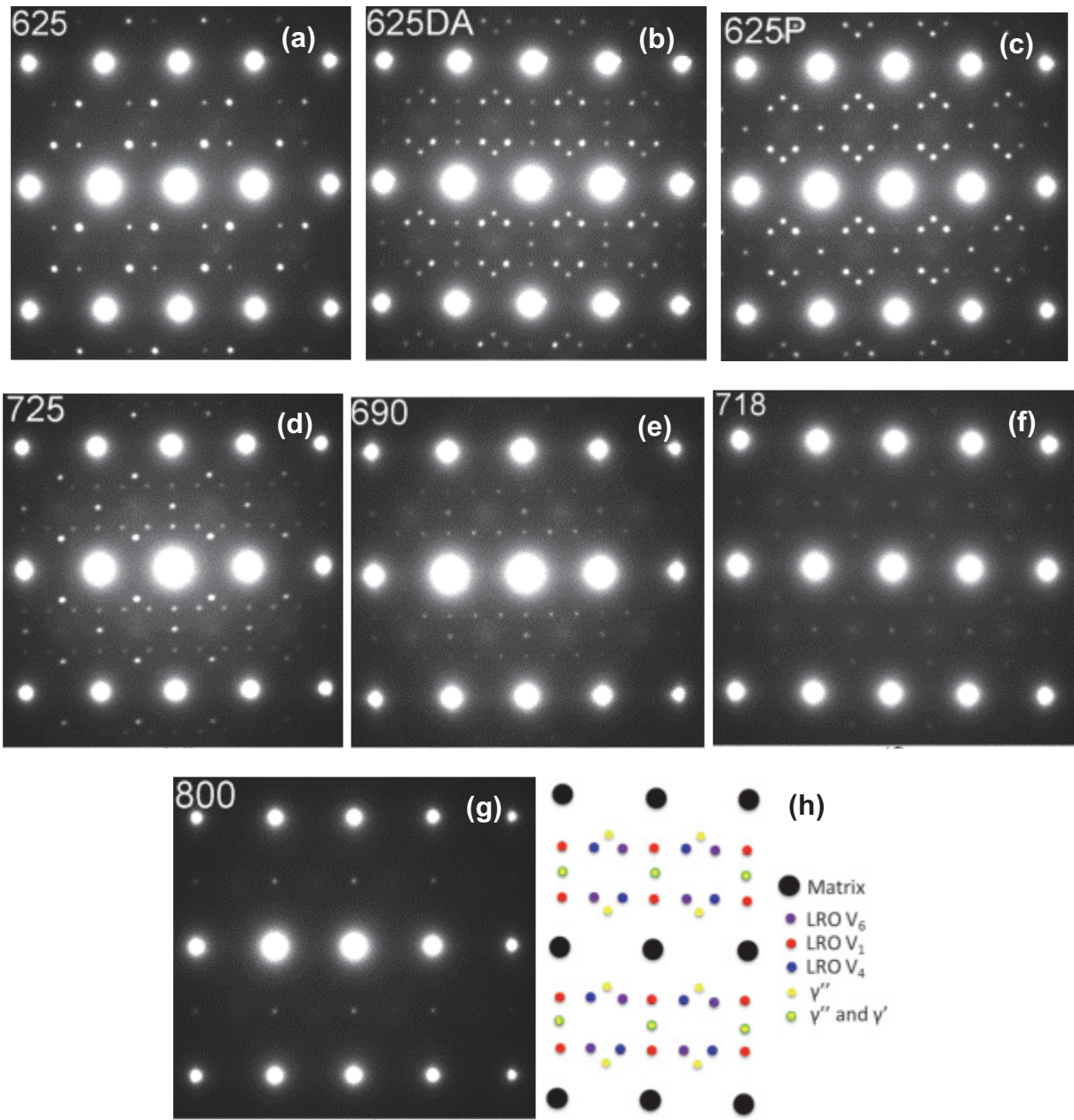


Figure 4-14 Diffraction patterns of the long range order phase (a) Alloy 625 after 5 dpa (b) Direct Aged 625 after 5 dpa (c) 625Plus after 5 dpa (d) Alloy 725 after 5 dpa (e) Alloy 690 after 5 dpa (f) Alloy 718 after 4 dpa (g) Alloy 800 after 5 dpa (h) Key for the diffraction pattern.

Results

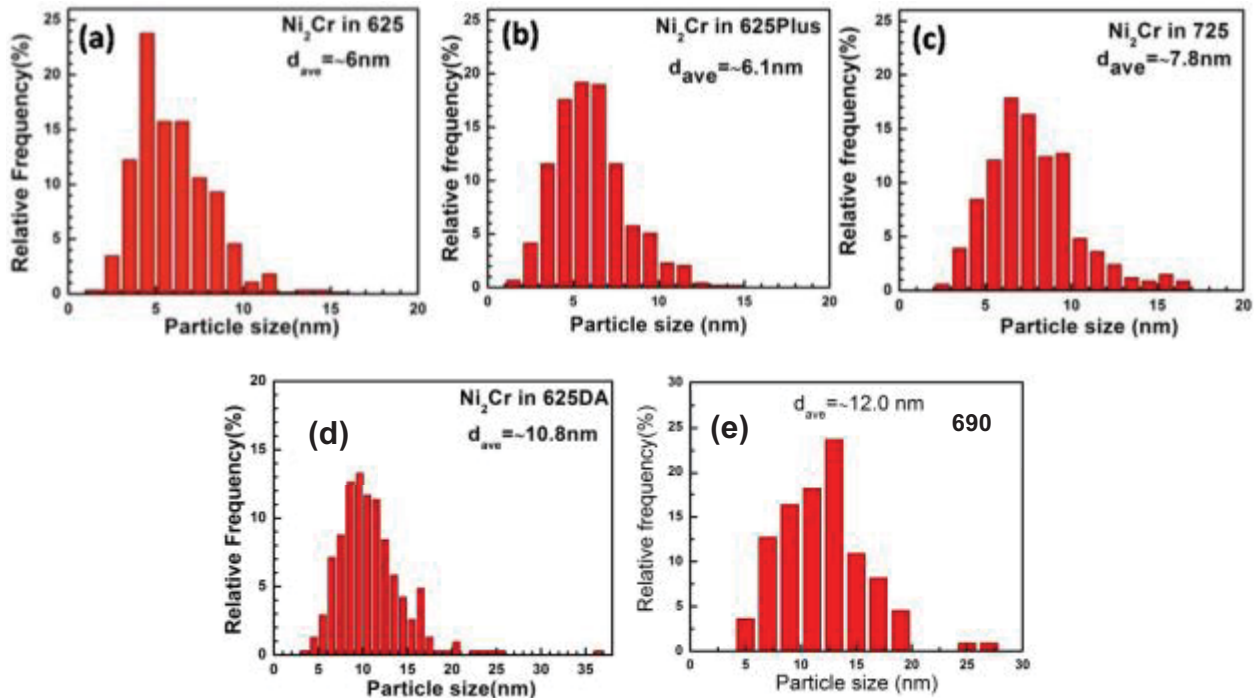


Figure 4-15 Size distribution of long range-order phase subjected to ~5 dpa at 360 °C using protons in alloy (a) 625, (b) 625Plus, (c) 725, (d) 625DA, and (e) 690. These long range-order phases are Pt₂Mo type structure with major chemical composition of Ni₂Cr. The detailed chemical compositions have yet to be determined.

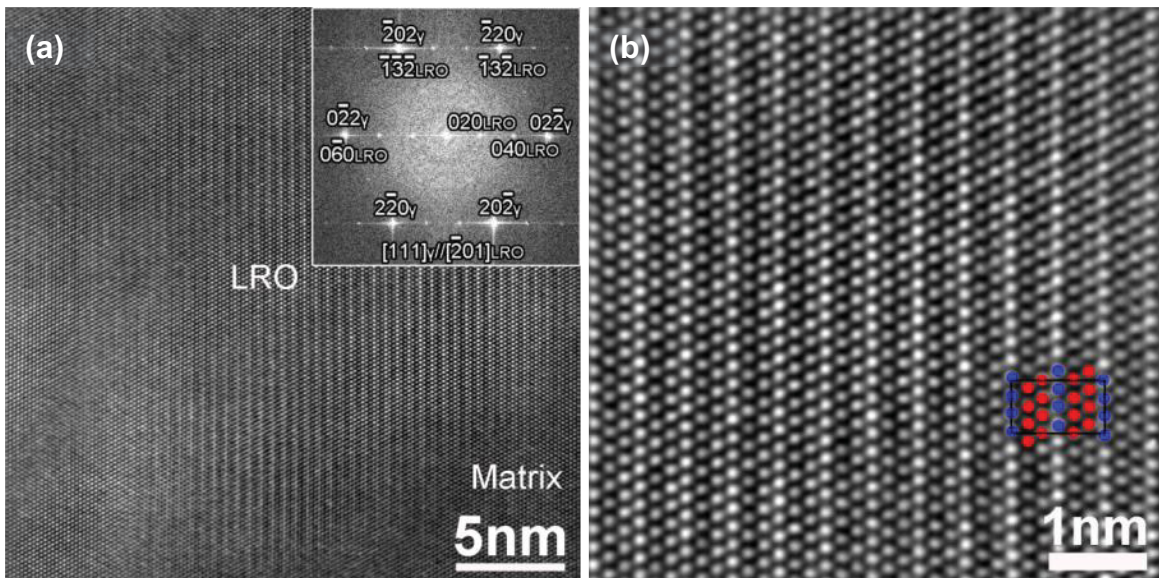


Figure 4-16 High resolution TEM images of LRO formed after 5 dpa irradiation at 360 °C in alloy 725. (a) The LRO is coherent with matrix. (b) Enlarged image of LRO phase after filtering. The overlapped dots is from [-201] direction of Ni₂Cr with Ni atom in red, Cr atom in blue.

Irradiation Induced γ' phase

The nickel and silicon enriched γ' phase is frequently observed in austenitic stainless steels after irradiation. Silicon segregates to the sinks under irradiation, which is believed to be the major cause for the formation of silicon-containing γ' phase [25]. However, it was not observed in alloys 625, 625Plus, 625DA and 725 reported previously [1]. Figure 4-17 shows the γ' phase in alloy 800 as confirmed by the diffraction pattern (inserted in the upright corner in Figure 4-17(a)). Dark field shows that the γ' precipitates are large elongated particles. STEM EDX mapping as shown in Figure 4-18 suggested that the Si and Ni are enriched in these γ' precipitates. Other elements were depleted in the particles. High-resolution TEM (HRTEM) in Figure 4-19 shows that the large elongated particles are composed of smaller ones around the dislocation. This observation is consistent with earlier observations. The γ' phase was also observed in alloy 690 as shown in Figure 4-20 with a diameter below 10 nm. The chemical analysis as shown in Figure 4-21 indicates that most of the γ' phase in alloy 690 is composed of Ti and Al.

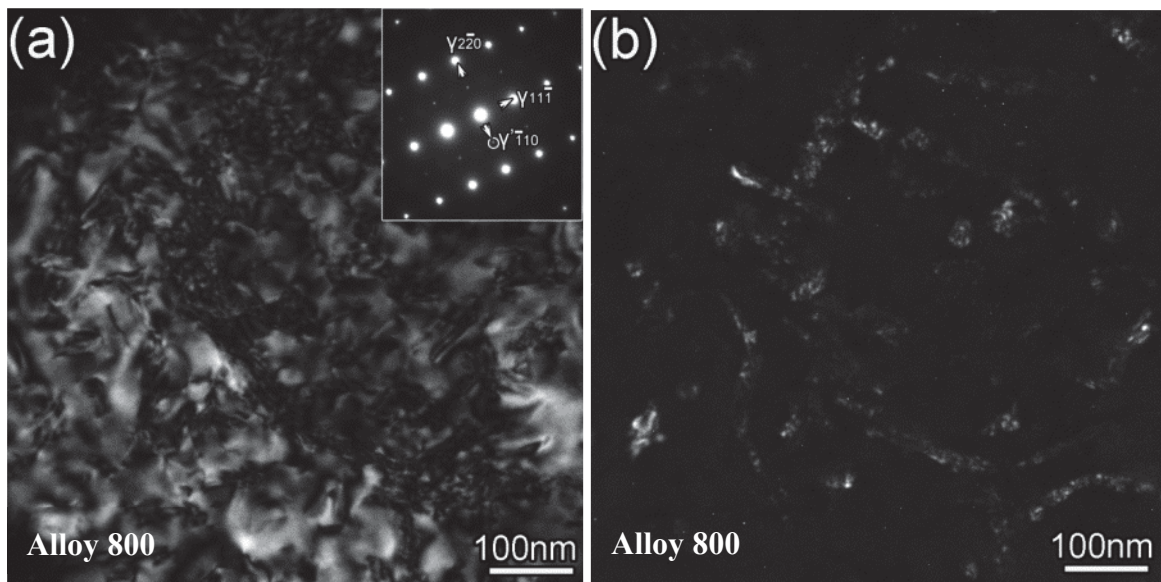


Figure 4-17 (a) Bright field (BF) and (b) dark field (DF) TEM image of γ' precipitates within the matrix in alloy 800

Results

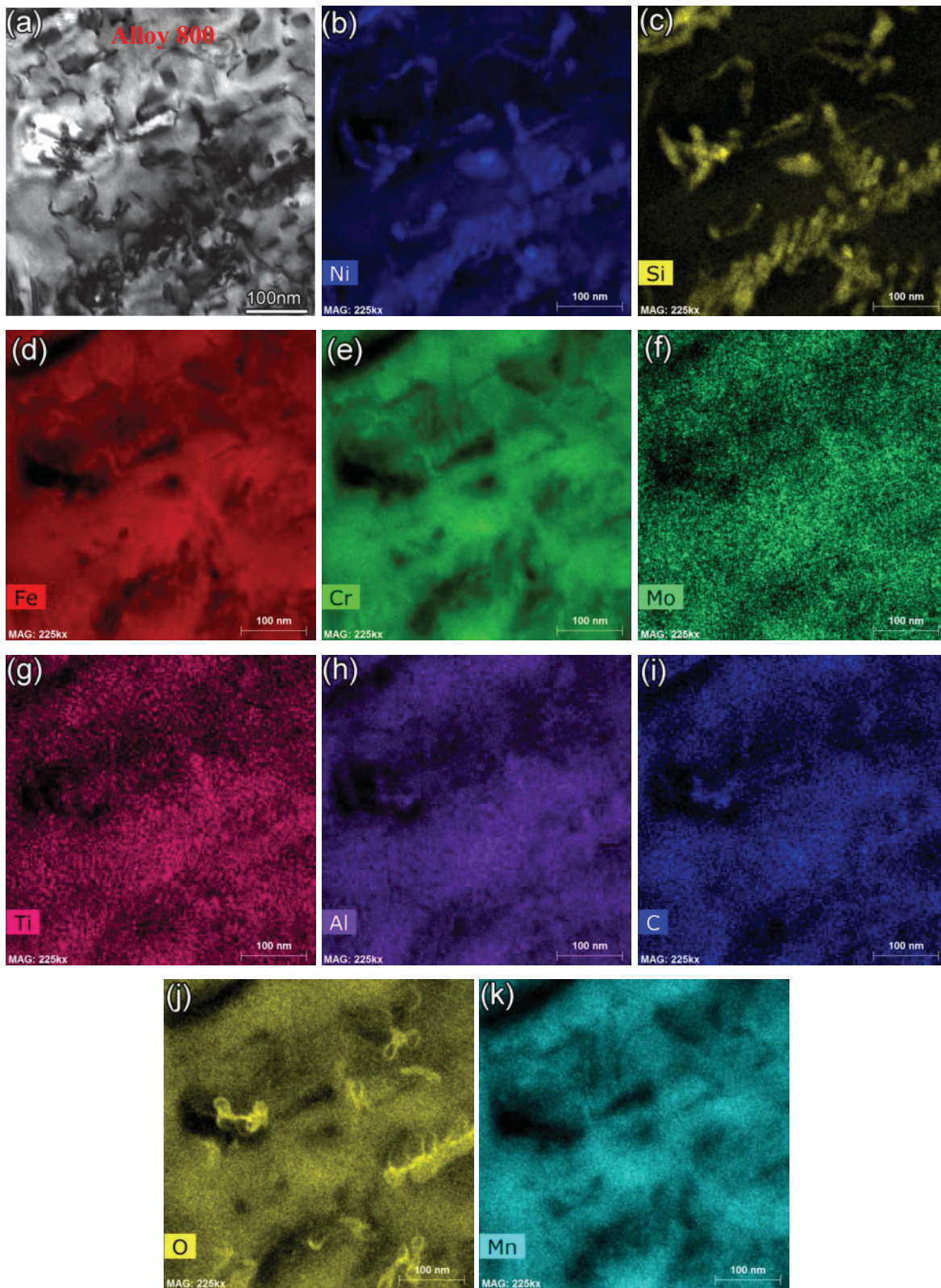


Figure 4-18 (a) Bright field (BF) and (b-k) elemental mapping of γ' precipitates within the matrix in alloy 800

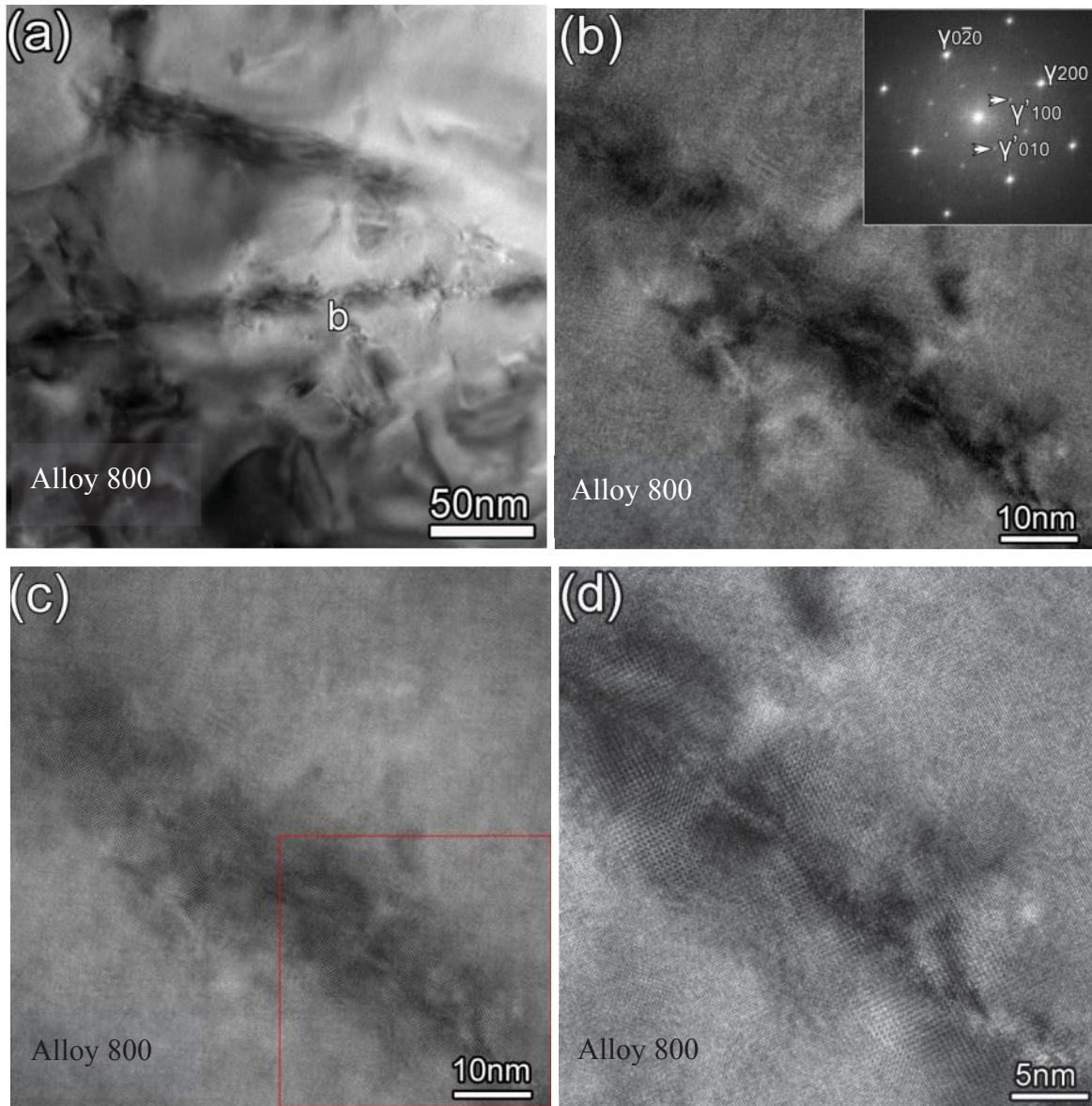


Figure 4-19 (a) Bright field of γ' precipitates within the matrix in alloy 800 and (b) HRTEM images of the particles (c) HRTEM image and overlapped with its filtered image and (d) enlarged picture of the redbox in (c).

Results

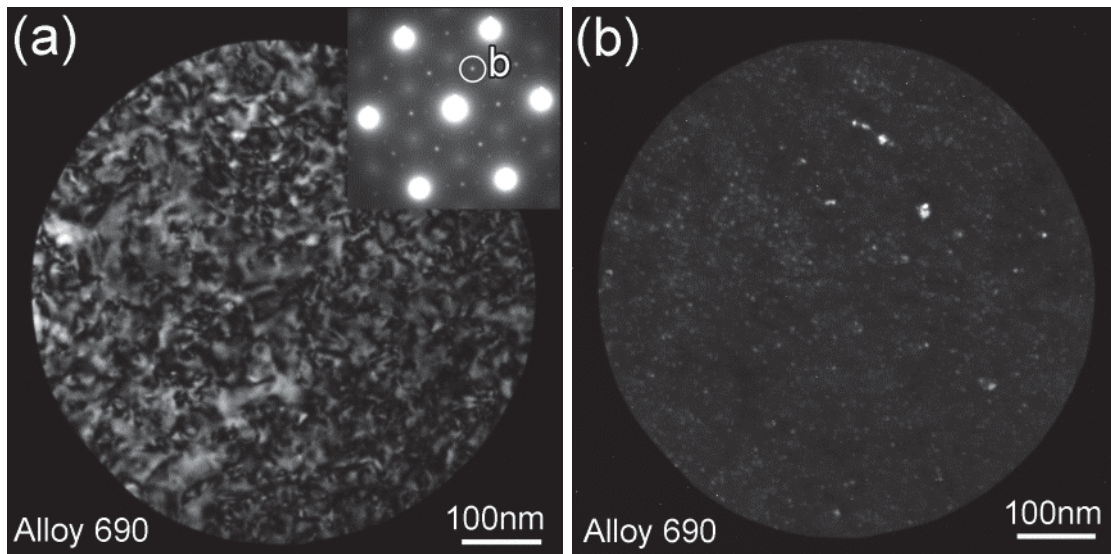
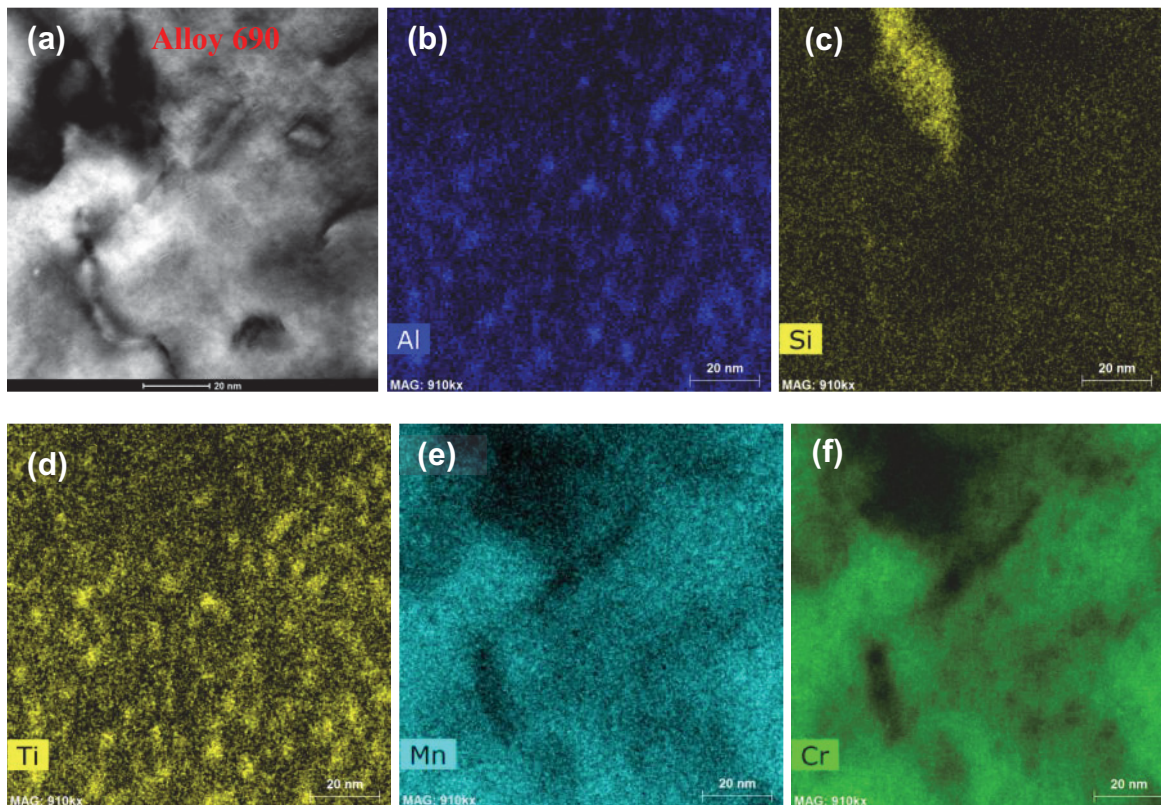


Figure 4-20 (a) Bright field and (b) dark field of γ' precipitates within the matrix in alloy 690



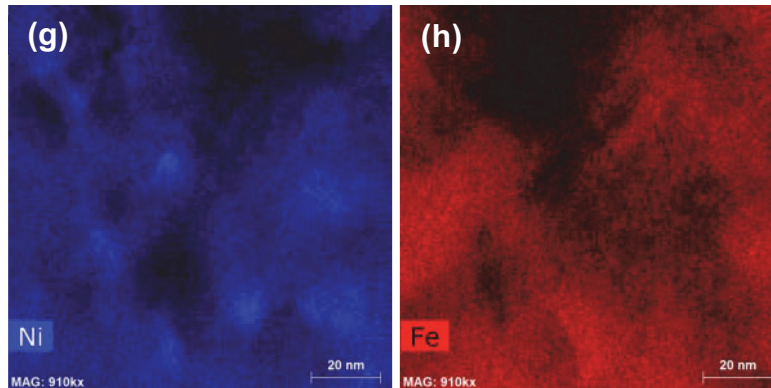


Figure 4-21 (a) Bright field (BF) and (b-h) elemental mapping of γ' precipitates within the matrix in alloy690

Voids

Void swelling is a common phenomenon in irradiated materials. It can change the dimension of the structure materials and significant residue stress may build up [26]. Poor resistance to void swelling is a common issue for austenitic stainless steel at high dpa. Some of the austenitic stainless steel or model alloys can form voids even at low dpa levels [27]. Voids were identified in alloy 310 as shown in Figure 4-22a. The voids in alloy 310 are faceted. The statistical results of voids size distributions are shown in Figure 4-22b. No voids were observed in any of the other alloys irradiated under the same conditions.

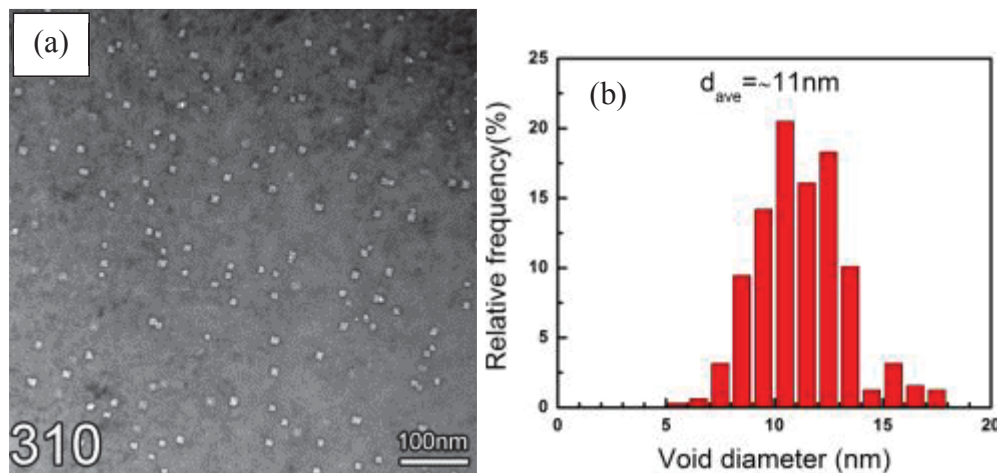


Figure 4-22 Voids in (a) alloy 310 and (b) voids distribution after 5dpa proton irradiation at 360°C

Irradiation Induced Segregation

Irradiation can significantly increase the population of point defects far from the equilibrium level. These point defects can migrate to the defect sinks such as free surface and grain boundary. This flux of point defects will change the elements around sinks, which causes radiation induced segregation (RIS). The RIS process around GB is widely investigated for

Results

various alloy systems. RIS is one of the primary concerns for causing irradiation assisted stress corrosion cracking. In the following sections, the RIS in nickel-base alloys and stainless steels are present separately due to the different chemical composition of minor elements.

RIS in nickel-base alloys

As shown in Figure 4-23, depletion of Ni, enrichment of Cr and Mo were observed in the as-received nickel-base alloys. The segregation seems smaller in alloy 625DA due to the lower aging temperature. As shown in Figure 4-24, following irradiation significant Ni enhancement was observed in the nickel-base alloy while Cr and Fe were always depleted. Mo was a slow diffuser, which was enriched in the as-received condition and depleted along with Cr in the irradiated condition. The segregation of other elements is insignificant or beyond the resolution of the instrumentation. A comparison of RIS in nickel-base alloys is summarized in Figure 4-25. 625DA showed the lowest GB Cr level around 8%. The nickel was enriched to 70%, which is around 10% above the bulk composition. The difference between nickel-base alloys is insignificant.

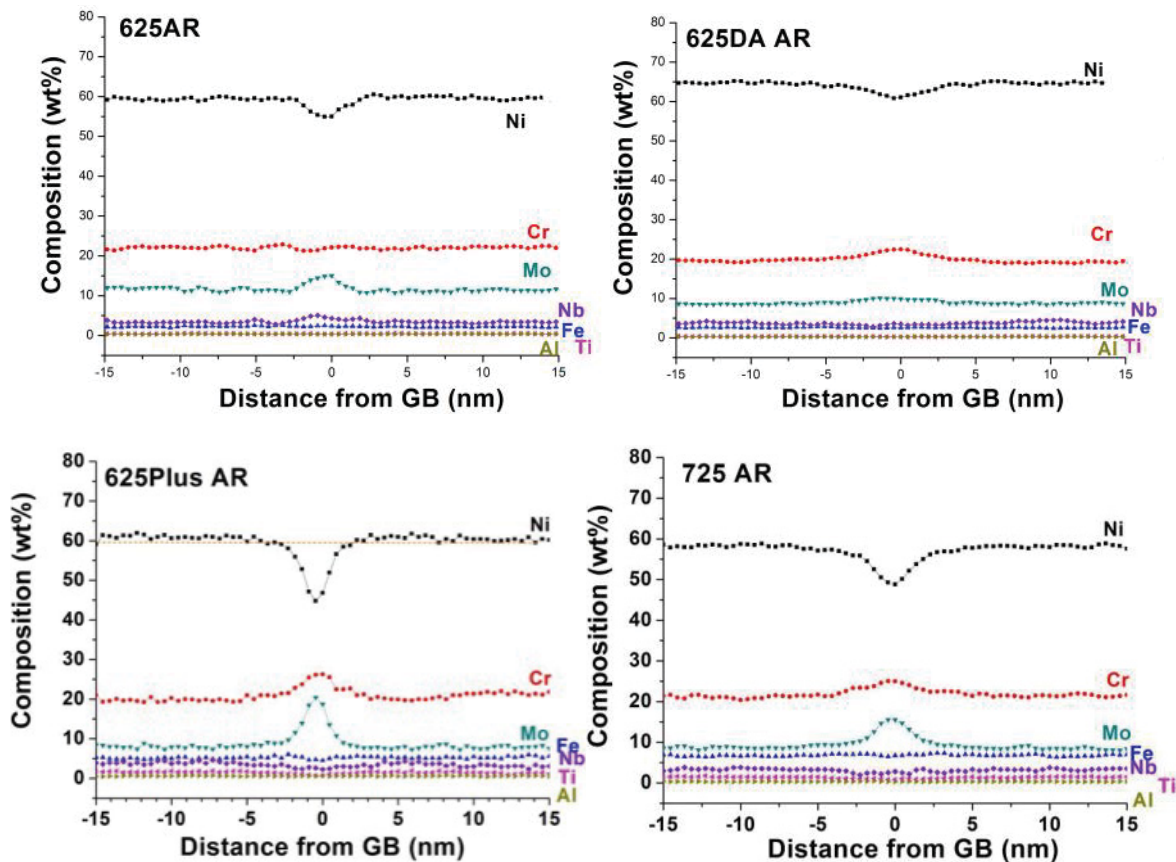


Figure 4-23 Segregation in as received thermally aged nickel-base alloys (a) alloy 625 (b) alloy 625DA (c) alloy 625Plus and (d) alloy 725

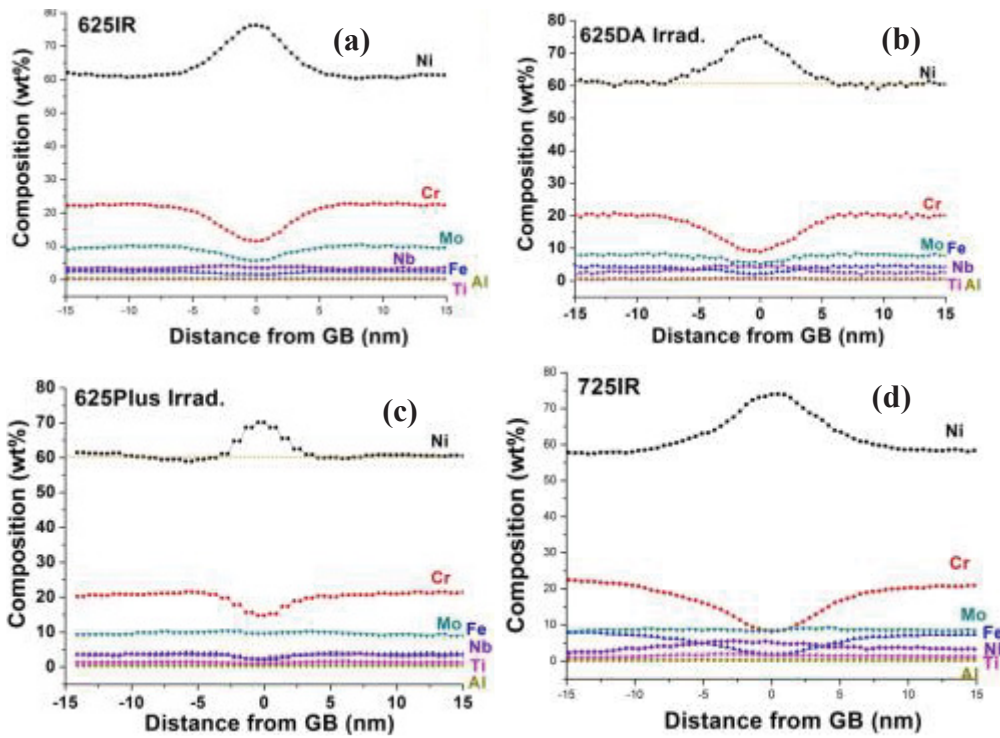


Figure 4-24 RIS in nickel-base alloys (a) alloy 625 (b) alloy 625DA (c) alloy 625Plus and (d) alloy 725 after around 5dpa proton irradiation at 360°C

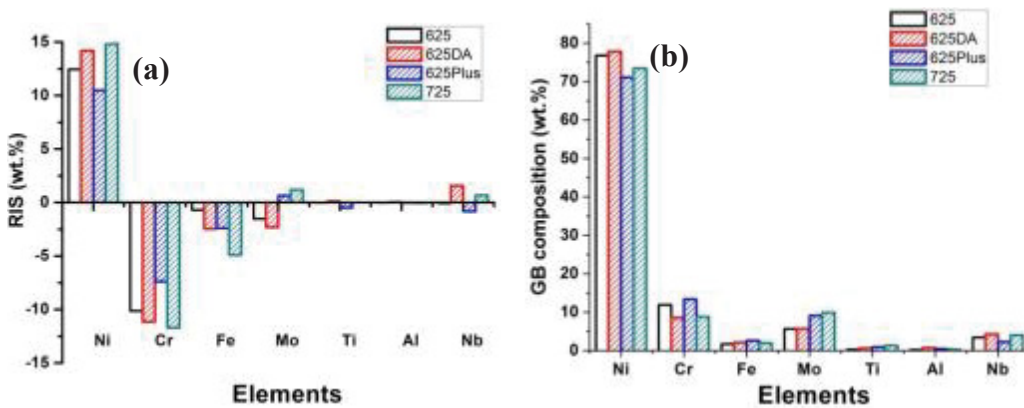


Figure 4-25 Comparison of (a) RIS and (b) GB chemical composition in nickel-base alloys

RIS in austenitic iron-base alloys

There was noticeable grain boundary segregation in alloy 310, Figure 4-26a, and insignificant in alloy 800, Figure 4-26c. Figure 4-26 RIS in steels (a) as received type 310 (b) irradiated type 310 (c) as received alloy 800 and (d) irradiated alloy 800. However, RIS is significant as shown in Figure 4-26b and d. The general pattern is the same as with the nickel-base alloys in which significant Ni diffused to the GB and Cr and Fe diffused away from the GB. The RIS of Si is pronounced, typically about 3 times its nominal value. In alloy 800, the amount of Si at the GB is

Results

comparable to that of Cr, with the nominal composition of Cr more than forty times that of Si in the alloy.

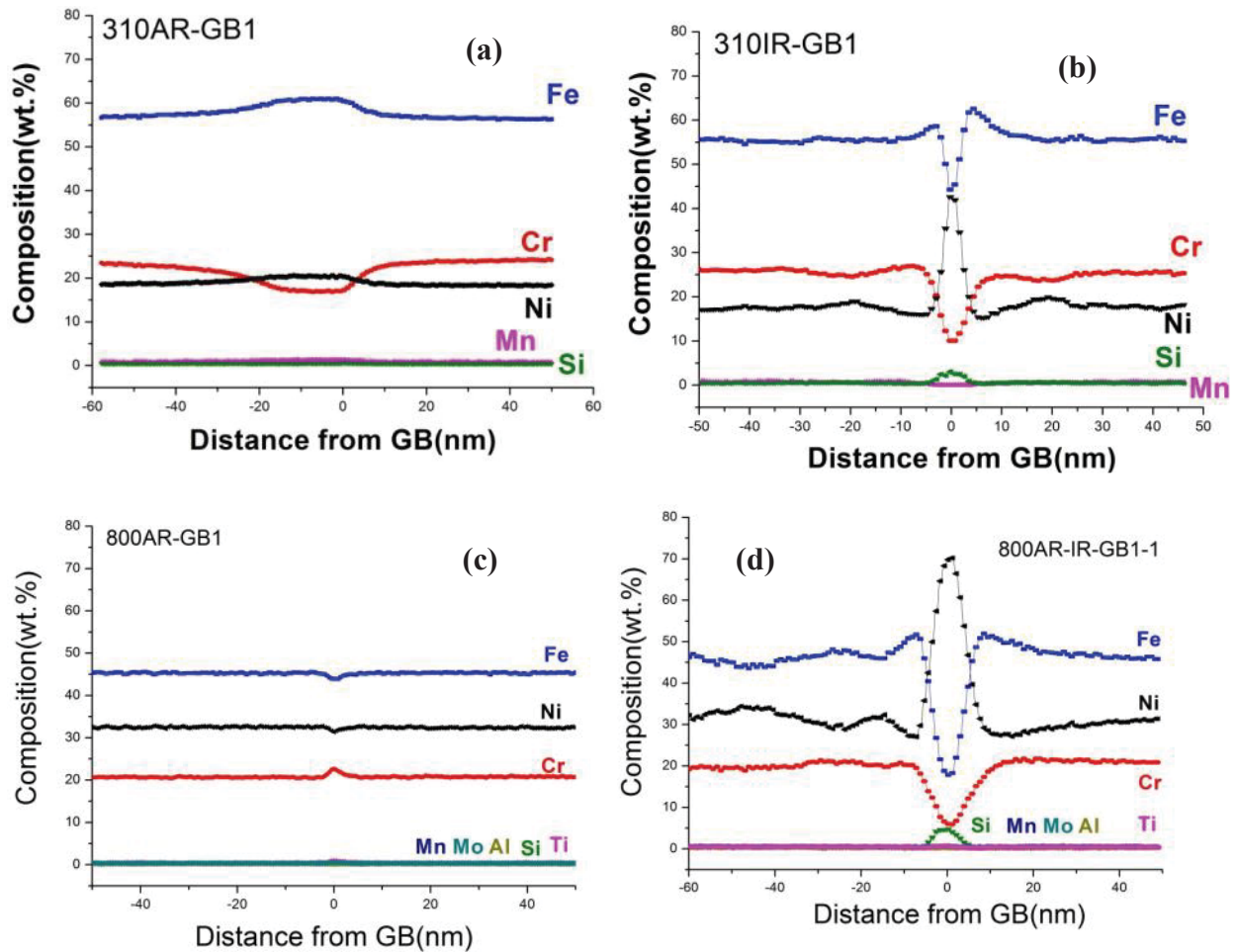


Figure 4-26 RIS in steels (a) as received type 310 (b) irradiated type 310 (c) as received alloy 800 and (d) irradiated alloy 800.

Microstructure Summary of Irradiated Samples

Table 4-4 summarizes all the microstructure features of the alloys after proton irradiation to 5 dpa at 360 °C. It was noted that the density of the LRO phase in alloy 625 and alloy 625DA was an order of magnitude higher than that in alloy 725. The dislocation density of all the nickel-base alloys was within an order of magnitude. Table 4-5 summarizes the RIS for all the nickel-base alloys. The austenitic alloys were shown in Table 4-6. All the major elements were listed.

Table 4-4 Effect of 2MeV proton irradiation to 5dpa at 360 on the microstructure features of alloys studied.

Alloy	Pre-existing Precipitates			New formed precipitates			Dislocation loops			Voids		
	before irradiation			after irradiation								
	d	f _v	ρ	d	f _v	ρ	d	f _v	ρ	d	f _v	ρ
	Ni ₂ Cr type											
	γ' phase											
625	N/A	N/A	N/A	6.0±2.2	N/A	43±19	4.9	14.9±5.6	4.7±2.0	2.19	N/A	
625P	13±3.3	4.5±3.5	2.51	12.7±3.4	6.3±1.6	3.3	6.1±2.1	10.5±2.6	1.2	16.7±5.4	3.1±0.8	1.62
725	18±6.0	2.9±1.2	3.69	18.9±4.7	2.3±0.9	3.2	7.8±2.6	2.0±0.9	0.5	23±8.7	1.4±0.6	1.01
625DA	12±3.1	2.1±0.2	0.78	11.5±3.3	6.6±4.0	2.7	10.8±3.8	9.6±3.9	6.3	13±5.8	10.2±1.1	4.16
690	N/A			12.0±4				0.61±0.53	0.6	34.6±21.7	0.45±0.13	0.49
	γ phase											
310	N/A			5.6±2.0			4.25±1.1	0.39		19.9±9.5	3.4±0.6	2.12
800	N/A			40.0 ±25.0			0.15±0.06	5.0	50.0 ±27	0.28±0.09	0.44	N/A

Unit: d (nm); ρ (10²²/m³); f_v (%); L (10¹⁵/m²).

Table 4-5 RIS for nickel-base alloys (wt.%)

Alloy	Ni	Cr	Fe	Mo	Ti	Al	Nb
625Plus	Matrix (wt. %)	60.65±0.77	20.79±0.50	5.00±0.76	1.43±0.12	0.52±0.12	3.11±0.32
	Avg.GB comp.(wt. %)	71.15±2.03	13.40±1.72	2.60±0.56	0.95±0.14	0.49±0.13	2.29±0.30
	RIS	10.49	-7.38	-2.40	-0.48	-0.03	-0.83
625DA	Matrix (wt. %)	63.67±0.045	19.70±0.70	4.62±0.30	0.56±0.04	0.70±0.13	2.74±0.24
	Avg.GB comp.(wt. %)	77.86±0.32	8.56±0.87	2.15±0.34	0.68±0.05	0.75±0.07	4.30±0.10
	RIS	14.19	-11.14	-2.47	0.12	0.048	1.56
625	Matrix (wt. %)	64.38±1.70	22.05±0.97	2.39±0.12	0.28±0.03	0.22±0.07	3.48±0.03
	Avg.GB comp.(wt. %)	76.82±0.09	11.92±0.43	1.70±0.05	0.27±0.03	0.20±0.12	3.41±0.38
	RIS	12.45	-10.13	-0.69	-0.02	-0.02	-0.06
725	Matrix (wt. %)	58.79±0.76	20.52±0.45	6.92±0.66	1.35±0.07	0.32±0.11	3.39±0.17
	Avg.GB comp.(wt. %)	73.58±1.73	8.83±1.02	1.99±0.25	1.35±0.31	0.26±0.07	4.07±1.24
	RIS	14.80	-11.69	-4.92	0.003	-0.058	0.68

Table 4-6 RIS for stainless steels (wt.%)

Alloy	Fe	Cr	Mn	Si	Ni	Al	Ti	Mo
-------	----	----	----	----	----	----	----	----

Results

310	Matrix (wt. %)	56.18±0.61	24.08±0.51	0.84±0.38	0.49±0.18	18.42±0.3
	Avg.GB comp. (wt. %)	48.78±6.36	13.84±5.35	0.21±0.30	2.39±0.89	34.78±11.12
	RIS	-7.39	-10.24	-0.62	1.9	16.35
800	Matrix (wt. %)	45.97±0.73	20.18±0.9	0.14±0.13	0.42±0.19	32.16±1.15
	Avg.GB comp. (wt. %)	21.60±3.79	6.15±0.39	0.04±0.07	2.91±1.66	67.91±2.5
	RIS	-24.37	-14.03	-0.10	2.49	35.75
					0.25±0.06	0.44±0.03
					0.22±0.04	0.82±0.06
					-0.04	0.38
						-0.09

4.5 Mechanical Properties

Irradiation hardening

Irradiation hardening measurements of all the ARRM alloys are listed in Table 4-7 and plotted in Figure 4-27. All the precipitate hardening alloys: 625Plus, 625DA, 725, and X750 show a similar hardness increase after irradiation of around 100 Hv, except for alloy 718, which is barely hardened. The hardness of austenitic stainless steels and solid solution nickel-base alloys doubled after irradiation, except for alloy 625. Alloy C22 showed the highest irradiation hardening of about 150%. The F/M steel T92 showed very little irradiation hardening.

Table 4-7 Microhardness Measurement before and after irradiation of the alloys investigated

Alloy	Pre-irradiation (Hv)	Post-irradiation (Hv)
625	346 ± 24.5	447 ± 20.4
625Plus	424 ± 22.5	482 ± 24.4
725	428 ± 17.8	526 ± 18.8
625DA	420 ± 16.0	577 ± 28.0
X750	411 ± 40	510 ± 46
718A	455 ± 28	461 ± 24
690	198 ± 12	345 ± 27
C22	198 ± 15	497 ± 23
800	154 ± 12.2	292 ± 25
310	170 ± 22	358 ± 28
T92	254 ± 12.1	281 ± 18

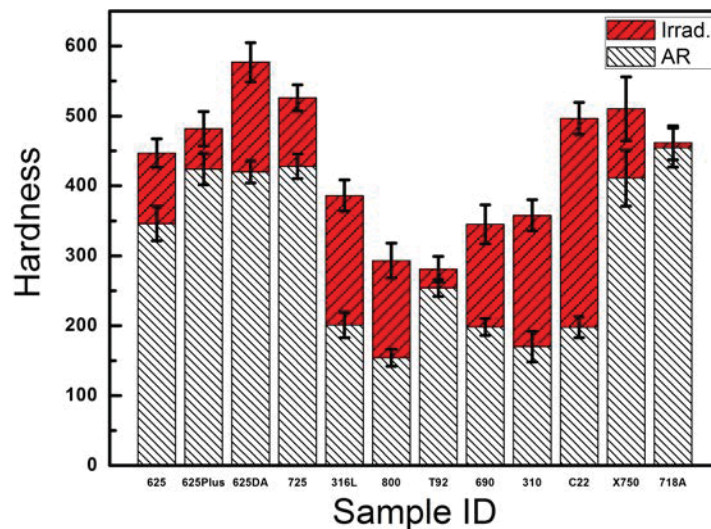


Figure 4-27 Irradiation induced hardening in various materials upto 5 dpa at 360 °C

Results

Room Temperature Tensile Behavior

Tensile test results of high stress alloys, 625Plus, 725, and 625DA, low strength alloy 625 are plotted in **Figure 4-28** and **Figure 4-29**, respectively. They were tested with multiple samples in the as-received condition and the mechanical property data are tabulated in **Table 4-8**.

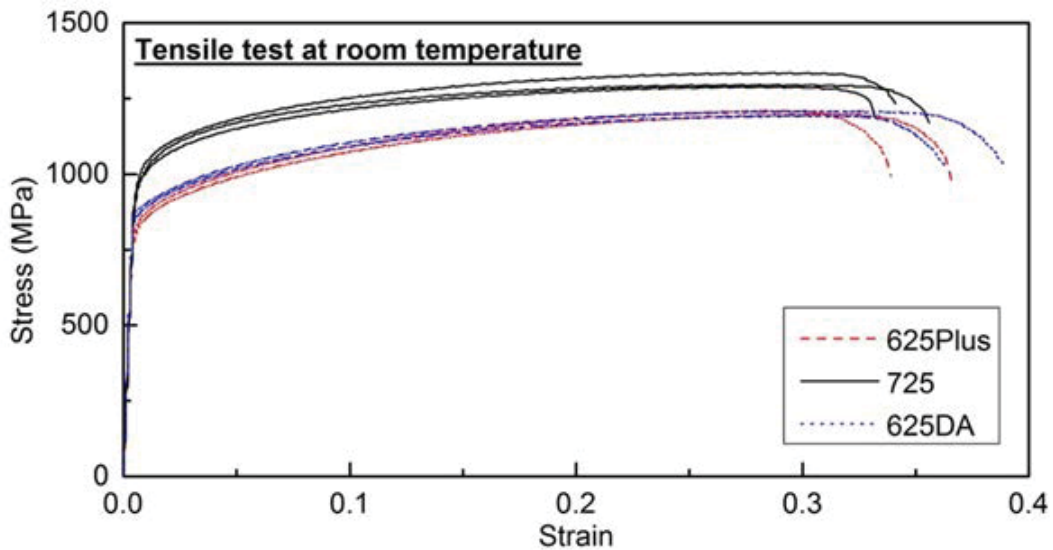


Figure 4-28 Stress-strain curve of high strength nickel-base alloys, 625Plus, 725, and 625DA (as-received condition) at room temperature in air.

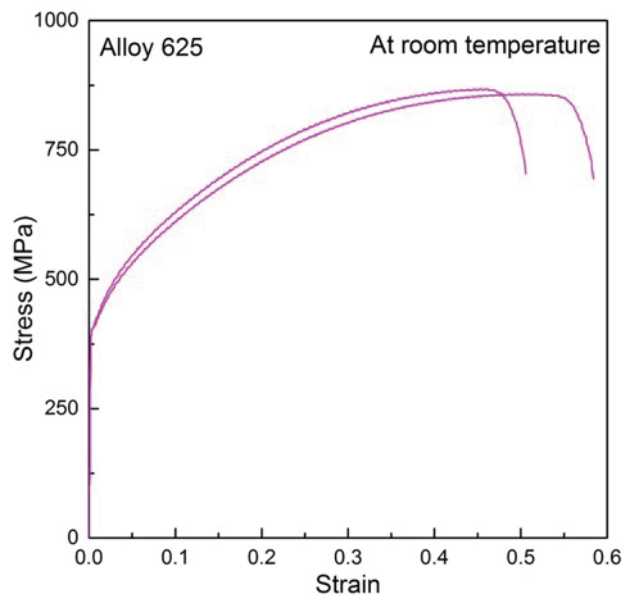


Figure 4-29 Stress-strain curve of low strength alloy 625 (as-received condition) at room temperature in air.

Table 4-8 Mechanical properties of nickel-base alloys 625Plus, 725, 625DA, 625.

Alloy	Elastic Modulus (GPa)	Yield Stress (MPa)	Ultimate Tensile Stress (MPa)	Plastic Strain at UTS (mm/mm)
625Plus	203 ± 7	828 ± 4	1205 ± 8	0.301 ± 0.013
725	207 ± 2	989 ± 10	1307 ± 25	0.29 ± 0.007
625DA	226 ± 20	871 ± 13	1202 ± 10	0.306 ± 0.006
625	253 ± 39	410 ± 8	854 ± 17	0.456 ± 0.046

Among the high strength alloys, 725 has the highest mechanical properties in yield strength and ultimate tensile stress and a very close elongation with 625Plus and 625DA. 625Plus and 625DA have quite similar mechanical properties. Alloy 625, on the other hand, is a low strength alloy and has lower strength properties but a much longer elongation.

4.6 CERT Test Results

Environmental Conditions

The CERT tests were conducted in two different water environments, the experimental conditions were plotted in Figure 4-30 and Figure 4-31 for BWR-NWC environment, and Figure 4-32, Figure 4-33, and Figure 4-34 for PWR-PW environments. For BWR-NWC, the pressure, the temperature, the conductivity, and the dissolved oxygen content during the entire CERT experiment were recorded. The pressure, temperature and dissolved oxygen were maintained at very stable levels during the entire straining process. The outlet conductivity increased during heating, likely due to cations released into the water environment due to corrosion at high temperature. After purification by the ion exchange filter, the conductivity returned to the desired level within the 24 hours.

PWR-PW tests have more parameters to control compared to tests in BWR-NWC. Due to the higher temperature, 320 °C vs. 288 °C, the pressure was also higher. Both pressure and temperature remained stable during the entire straining process. Outlet and inlet conductivities were in the range 20 to 30 μS/cm because of the saturation of boron and lithium ions. Combining the conductivity data and pH measurement (conducted several times during the experiment), the concentration of [B] and [Li] was calculated and adjustments were then made to maintain the target concentrations.

CERT tests were also conducted in an inert gas (argon) environment at 320 °C.

Results

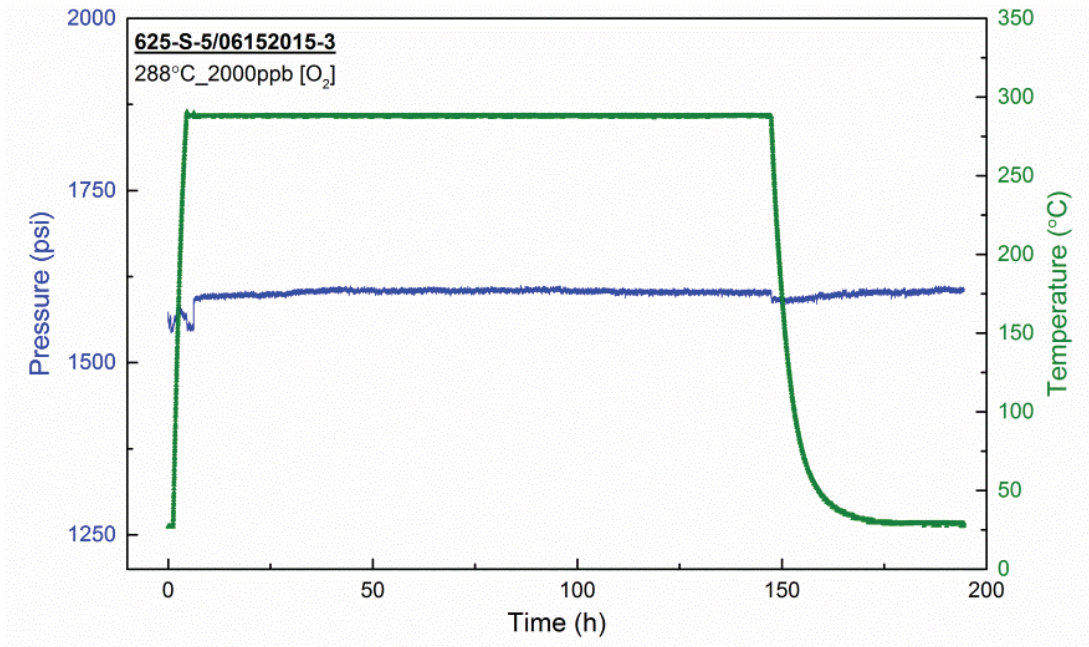


Figure 4-30 Experimental conditions for alloy 625 (5 dpa) in BWR-NWC environment: pressure (left) and temperature (right) versus time.

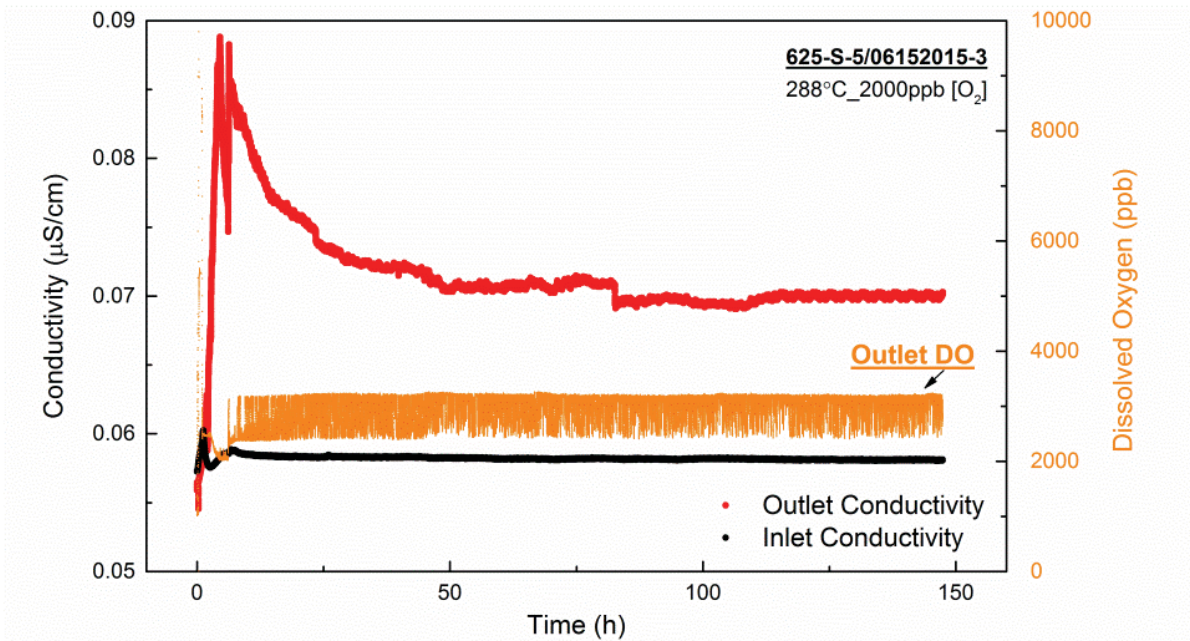


Figure 4-31 Experimental conditions for alloy 625 (5 dpa) in BWR-NWC environment: conductivity (left) and dissolved oxygen (right) versus time.

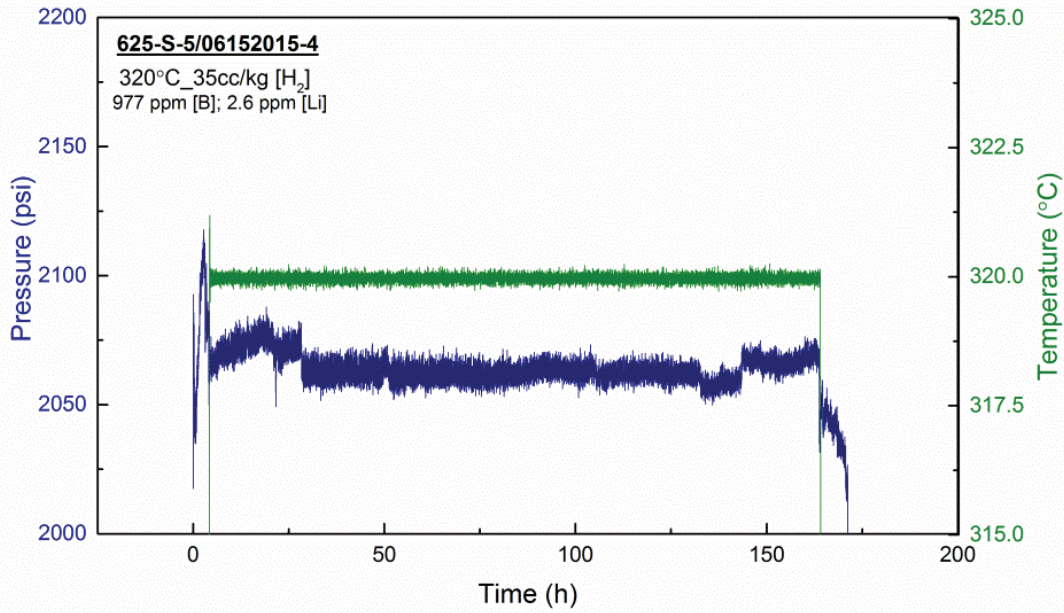


Figure 4-32 Experimental conditions for alloy 625 (5 dpa) in PWR-PW environment: pressure (left) and temperature (right) versus time.

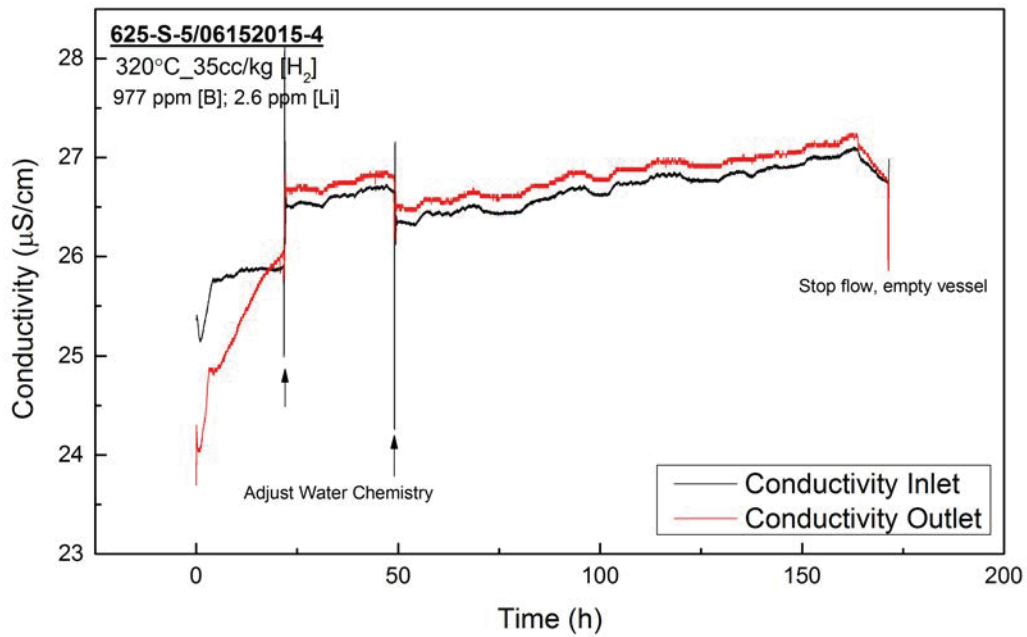


Figure 4-33 Experimental conditions for alloy 625 (5 dpa) in PWR-PW environment: conductivity versus time.

Results

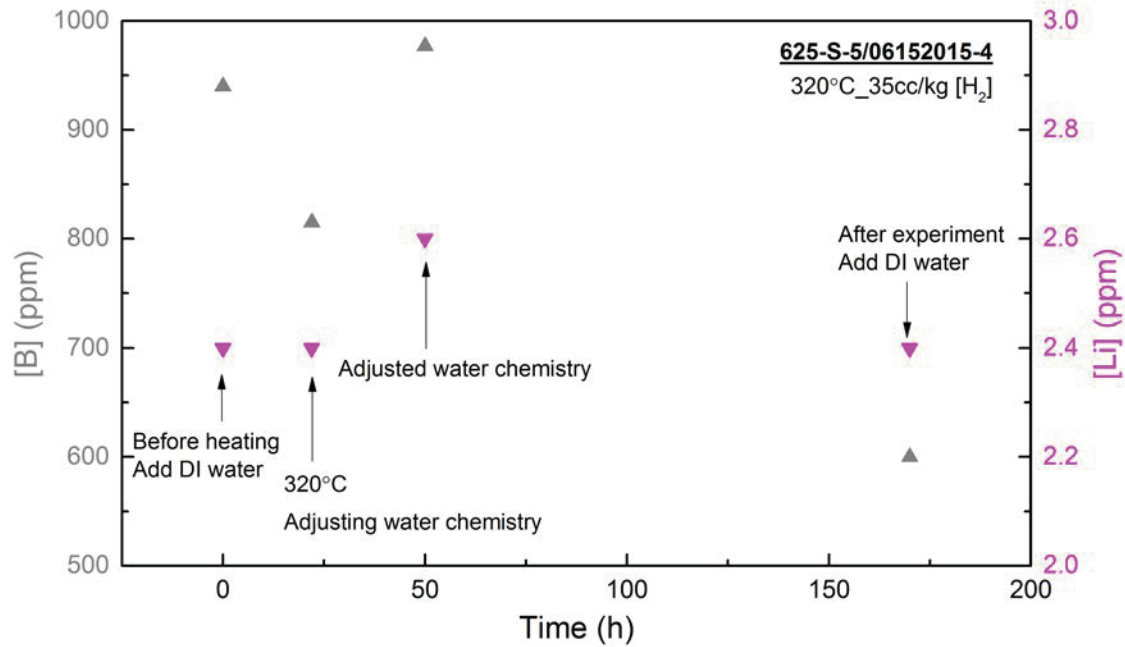


Figure 4-34 Experimental conditions for alloy 625 (5 dpa) in PWR-PW environment: [B] concentration (left) and [Li] concentration (right) versus time.

High strength alloys

CERT tests on high strength nickel-base alloys, 625Plus, 725, and 625DA were completed in both BWR-NWC and PWR-PW environments. Two samples of each alloy were tested for each environment. All alloys were strained to a plastic strain close to 4% as determined by the LVDT, and later verified from the fiducial marks on the samples. The stress-strain curves of each alloy are shown in Figure 4-35, Figure 4-36, and Figure 4-37. The stress-strain curves of nickel-base alloys in high temperature are plotted in Figure 4-38. The summary of mechanical properties at high temperature is listed in

Table 4-9.

Because less than 1% of the thickness of the alloy samples received irradiation damage by the proton beam ($20\ \mu\text{m}$ irradiation depth over 2 mm bar thickness), the yield strengths obtained were not expected to show any effect of irradiation. The serrations in the plastic deformation region were due to the dynamic strain aging of the alloys. Due to the high temperature, a significant decrease in mechanical properties was evident for all the alloys in both environments, compared to room temperature tests (**Figure 4-28**). Among all alloys, alloy 725 had the highest yield strength.

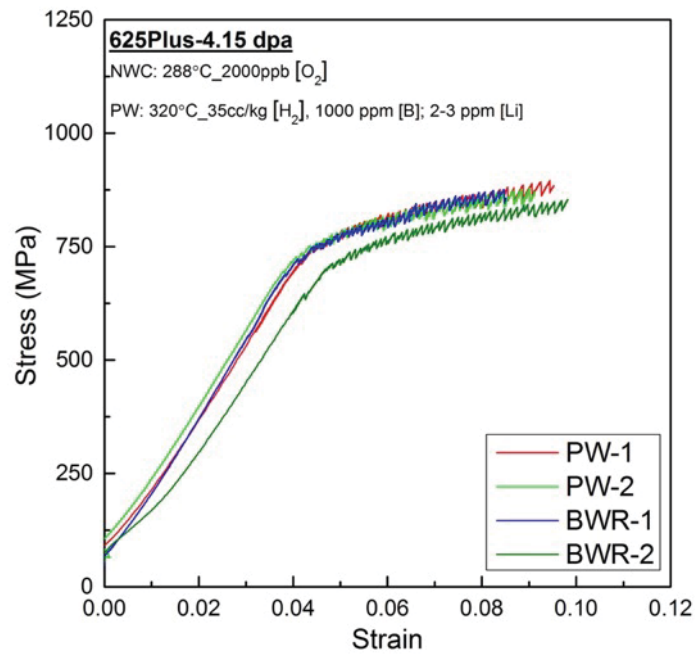


Figure 4-35 Stress-strain curve of 625Plus in both BWR-NWC and PWR-PW environments.

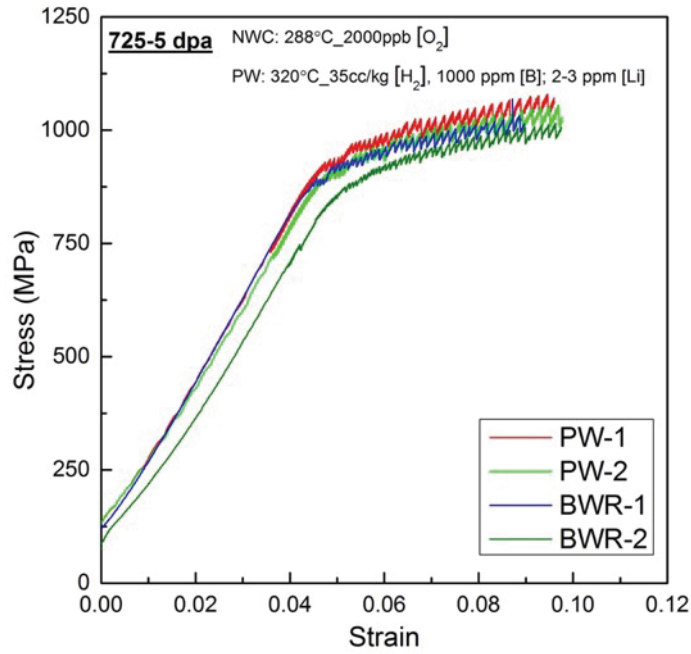


Figure 4-36 Stress-strain curve of 725 in both BWR-NWC and PWR-PW environments.

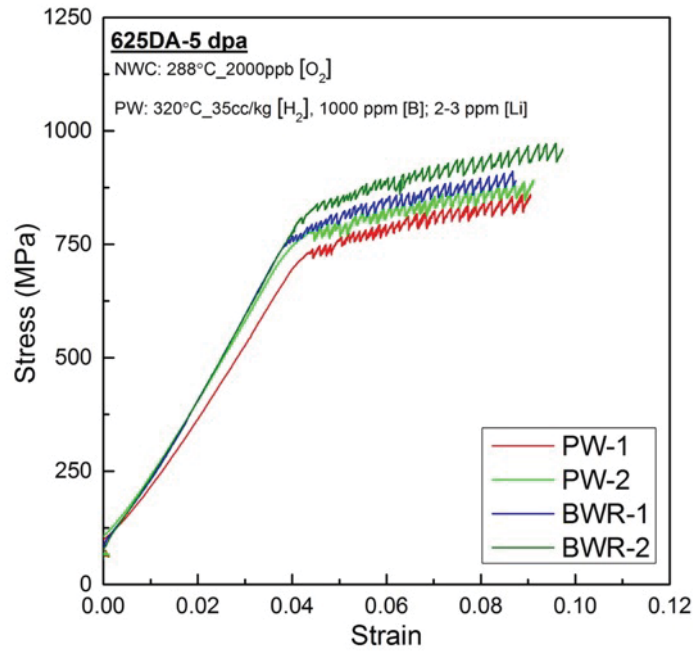


Figure 4-37 Stress-strain curve of 625DA in both BWR-NWC and PWR-PW environments.

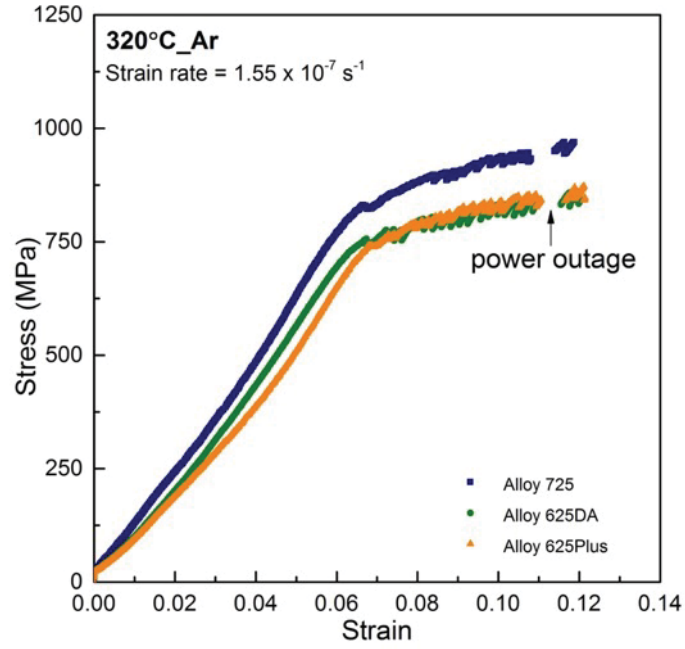


Figure 4-38 Stress-strain curve of high strength nickel-base alloys in Ar environment at high temperature.

*Results***Table 4-9 CERT results summary of high strength nickel-base alloys, NM: no measurement.**

Alloy	Environment	Yield Stress (MPa)	Plastic strain by LVDT (%)	Plastic Strain (%) from fiducial marks
625Plus	NWC-1	730 ± 17	3.6 ± 0.1	NM
	NWC-2	713 ± 9	4 ± 0.1	3.9
	PW-1	740 ± 7	4.25 ± 0.1	4
	PW-2	732 ± 9	4.15 ± 0.2	3.9
	AR	754 ± 23	4.3 ± 0.4	3.6
725	NWC-1	890 ± 17	3.7 ± 0.1	NM
	NWC-2	874 ± 13	3.9 ± 0.2	3.9
	PW-1	923 ± 10	4.1 ± 0.1	4
	PW-2	911 ± 19	4.25 ± 0.2	3.9
	AR	830 ± 45	4.2 ± 0.2	3.5
625DA	NWC-1	760 ± 11	4.0 ± 0.1	3.8
	NWC-2	830 ± 11	4.55 ± 0.1	4.4
	PW-1	732 ± 11	3.9 ± 0.2	3.8
	PW-2	767 ± 13	4.2 ± 0.1	4.0
	AR	756 ± 21	4.6 ± 0.2	4.1

Low strength alloys

The CERT test of low strength nickel-base alloy 625 was completed in both BWR-NWC and PWR-PW environments, the stress-strain curve is shown in Figure 4-39. The detailed CERT results are given in Table 4-10. Due to a problem with the irradiation, only one specimen was available for testing in BWR-NWC. However, since the two results in PWR-PW were quite different, another test in primary water will be conducted.

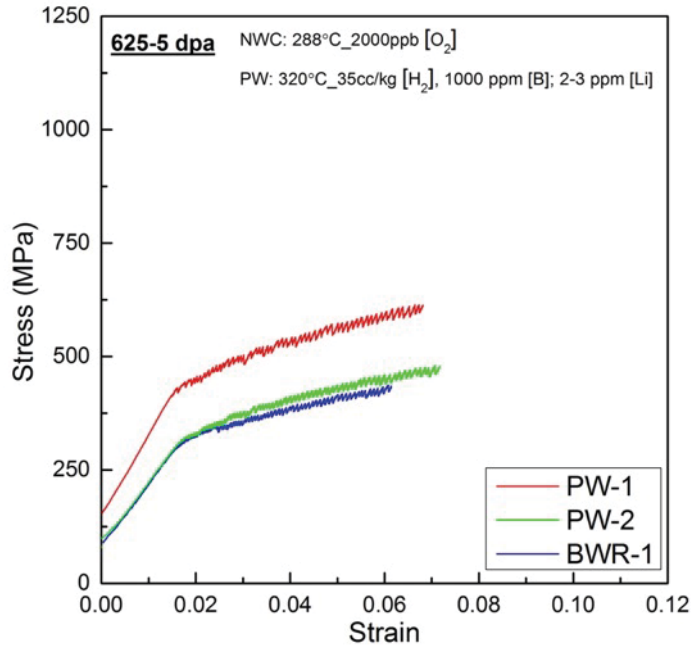


Figure 4-39 Stress-strain curve for alloy 625 (5 dpa) in BWR-NWC and PWR-PW environment.

Table 4-10 CERT results summary of high strength nickel-base alloys, NM: no measurement.

Alloy	Environment	Yield Stress (MPa)	Plastic strain by LVDT (%)	Plastic Strain (%) from fiducial marks
625Plus	NWC-1	326 ± 8	3.45 ± 0.1	NM
	PW-1	380 ± 9	4.05 ± 0.1	NM
	PW-2	327 ± 8	4.2 ± 0.1	4.0

4.7 Cracking Behavior

High Strength Alloys

Cracks were observed in both non-irradiated and irradiated areas for all the high strength nickel-base alloys in BWR-NWC and PWR-PW environments. However, no cracks were observed in an inert environment (argon gas). Micrographs of these cracks are shown in the following figures, **Figure 4-40** for BWR-NWC, **Figure 4-41** for PWR-PW, and **Figure 4-42** for inert environment, respectively. The strain (stress) direction was horizontal.

For both BWR-NWC and PWR-PW environments, the surface was covered with oxide crystallites. The oxide formed on nickel-base alloys should consist of a duplex oxide; an inner layer of continuous Cr-rich oxide with a discontinuous external layer with composition, morphology and microstructure depending on the environment and exposure duration [28, 29]. However, most of the external oxide should be an iron-rich spinel oxide, typically of the form of $Ni_{1-x}Fe_{2+x}O_4$, which may be the small crystallites observed on the surface [30-32].

Results

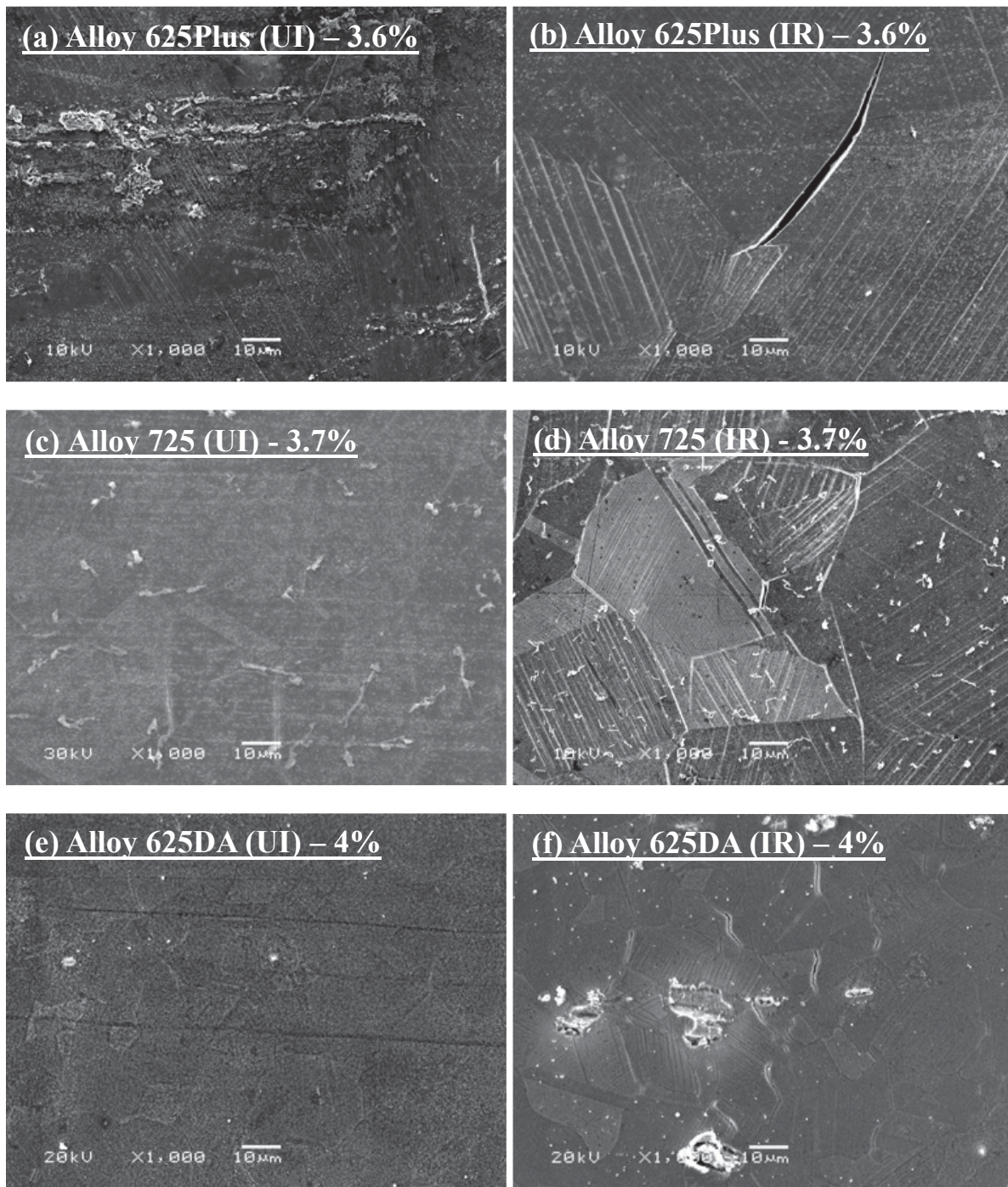


Figure 4-40 SEM micrographs of high strength nickel-base alloys 625Plus in (a) and (b), 725 in (c) and (d), and 625DA in (e) and (f), irradiated to a dose of 5 dpa and strained to ~ 4% in BWR-NWC environment, stress direction: horizontal.

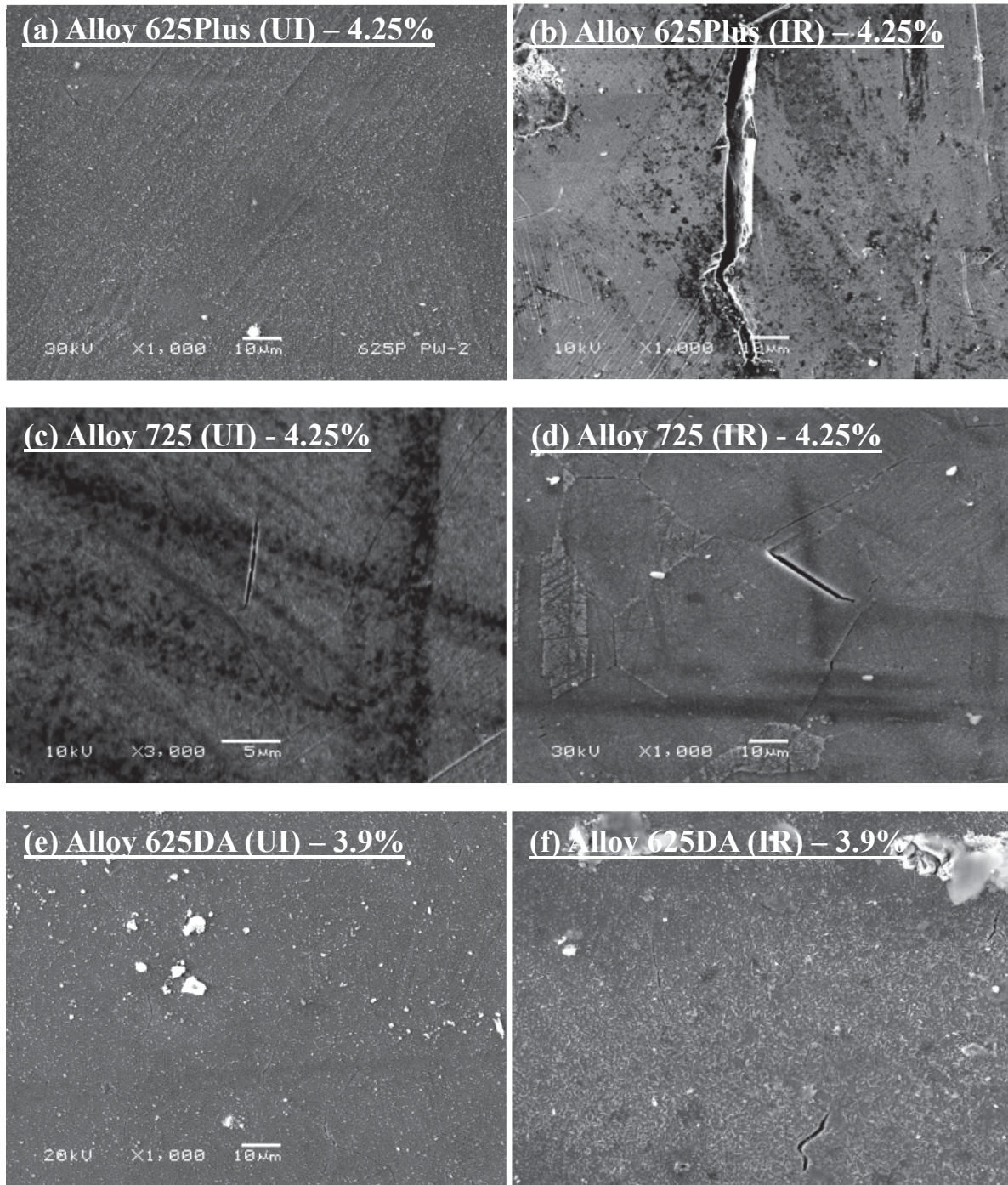


Figure 4-41 SEM micrographs of high strength nickel-base alloys 625Plus in (a) and (b), 725 in (c) and (d), and 625DA in (e) and (f), irradiated to a dose of 5 dpa and strained to ~ 4% in PWR-PW environment, stress direction: horizontal.

Results

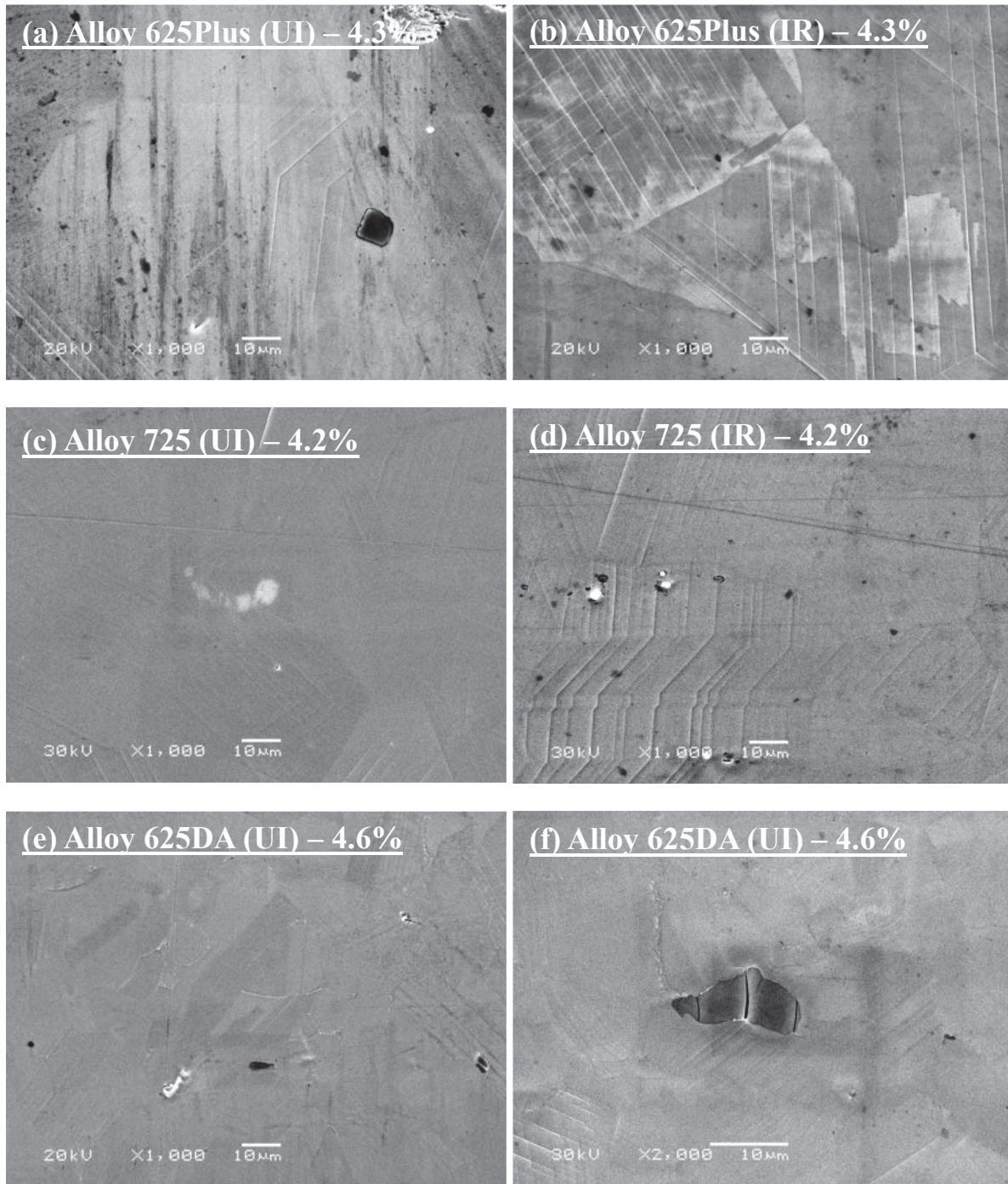


Figure 4-42 SEM micrographs of high strength nickel-base alloys 625Plus in (a) and (b), 725 in (c) and (d), and 625DA in (e) and (f), irradiated to a dose of 5 dpa and strained to ~ 4% in inert environment (Ar gas), stress direction: horizontal.

The morphology of the cracks for each alloy was different for the irradiated and non-irradiated areas. The number of cracks in the irradiated area was greater than in the non-irradiated area.

Crack opening was also greater in the irradiated area (several microns) compared to the non-irradiated area (less than one micron). In the irradiated area, the cracks on alloy 625Plus were wide and long, with lengths of tens to hundreds of micrometers in both water environments. The cracks on alloy 725 were easy to find at the triple junctions of the grains as most of them had just initiated thus were relatively small. Alloy 625DA had a very small grain size, so most cracks were small and extended along several facets. In the non-irradiated area, cracks for all the alloys were relatively very short and narrow.

In the inert environment, no cracks were found in alloy 625Plus, 725, and 625DA. However, dislocation channels were obvious in the irradiated area.

Low Strength Alloy

The cracks of alloy 625 in both BWR-NWC and PWR-PW environments are shown in **Figure 4-43**, and **Figure 4-44**. The cracking behavior seemed similar to that in the high strength alloys. Long, wide cracks were found in the irradiated area while short, narrow cracks were predominant in the non-irradiated area in both environments.

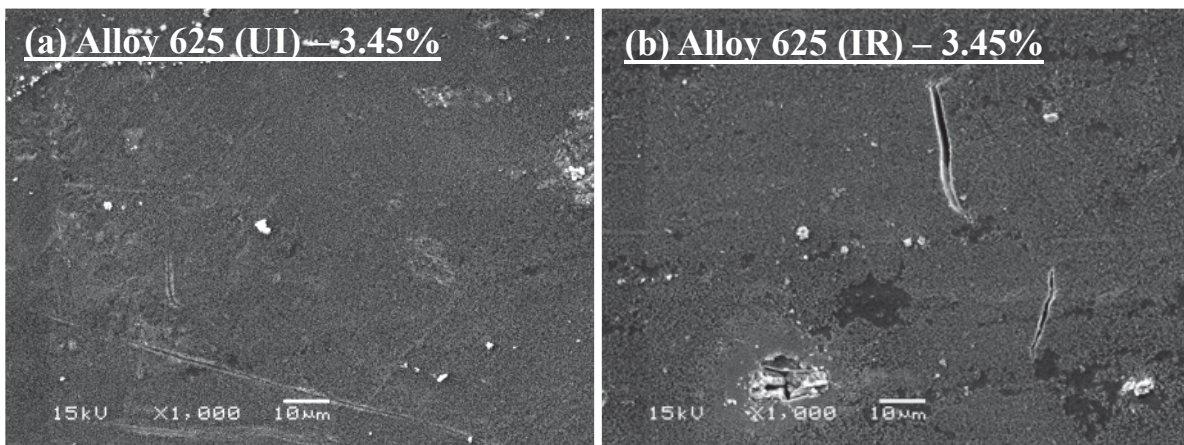


Figure 4-43 SEM micrograph of low strength nickel-base alloy 625 in (a) and (b), irradiated to a dose of 5 dpa and strained to ~ 4% in BWR-NWC environment, stress direction: horizontal.

Results

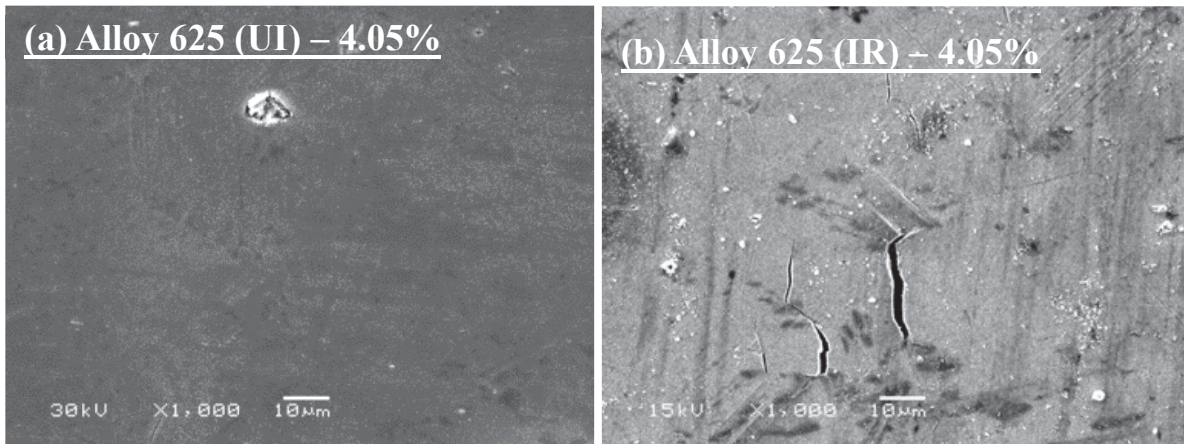


Figure 4-44 SEM micrograph of low strength nickel-base alloy 625 in (a) and (b), irradiated to a dose of 5 dpa and strained to ~ 4% in PWR-PW environment, stress direction: horizontal.

IASCC Susceptibility

To evaluate the cracking behavior of different alloys, SEM images were taken over similar size areas (approximately 1 mm²) in both irradiated and non-irradiated areas of the tensile sample. Only intergranular cracks were considered for the measurement.

Crack characterization for each condition including the following parameters:

- Average crack length;
- Crack density: the number of cracks observed per unit area;
- Crack length per unit area: the total crack length divided by the analyzed area;

The most representative metric to describe the cracking susceptibility is crack length per unit area, which measures the extent of cracking by incorporating both the density and the length of cracks. For all the alloys, the crack length per unit area was much higher in the irradiated area than in the non-irradiated area. The IASCC susceptibility of nickel-base alloys in BWR-NWC and PWR-PW are plotted in **Figure 4-45**, and **Figure 4-46**. The details of the cracking data are listed in **Table 4-11**.

By crack length per unit area, alloy 625DA was the most susceptible alloy to IASCC in both BWR-NWC and PWR-PW environments, especially in NWC. Using this same metric, alloy 725 had the lowest susceptibility. Alloy 625Plus also had a high IASCC susceptibility in both water environments. In NWC, a data point of austenitic stainless steel 304 from the paper Jiao *et al.* [33] was included for reference. That alloy was irradiated to the same dose at the same temperature and strained in the same environment to several percent plastic strain. All the nickel-base alloys studied had a much higher IASCC susceptibility than 304 stainless steel alloy in BWR-NWC environment. However, it should be noted that 304 is a low strength alloy, and therefore the comparison with alloy 625 is more appropriate. A reference from the category of high strength alloy needs to be used to compare the cracking susceptibility with the others. For alloy 625, as the only low strength alloy, the cracking behavior in PWR-PW was very inconsistent between samples, being high in one specimen and low in the other, just like the

CERT results. Therefore, the cracking behavior for alloy 625 in PWR-PW environment is still being investigated.

The ensemble of crack length per unit area of all nickel-base alloys is plotted in Figure 4-47. For high strength nickel-base alloys, the cracking susceptibility was always higher in BWR-NWC than in PWR-PW environment. It was quite reasonable since the NWC environment is far more aggressive [34, 35] than primary water and resulting in more and longer cracks. It was still hard to interpret the result for alloy 625 due to the inconsistent cracking behavior in primary water.

Another metric used to measure cracking susceptibility is the fraction of grain boundary length that cracked. This metric eliminates the influence of grain size in the data. The ratio between cracked grain boundary length and high angle grain boundary (HAGB) length is shown in Figure 4-48. The data shows that 625Plus had the highest ratio of grain boundary cracking. In other words, alloy 625Plus had the highest IASCC susceptibility in both BWR-NWC and PWR-PW environments. However, among the three high strength alloys that were tested alloy 725 still had the lowest susceptibility.

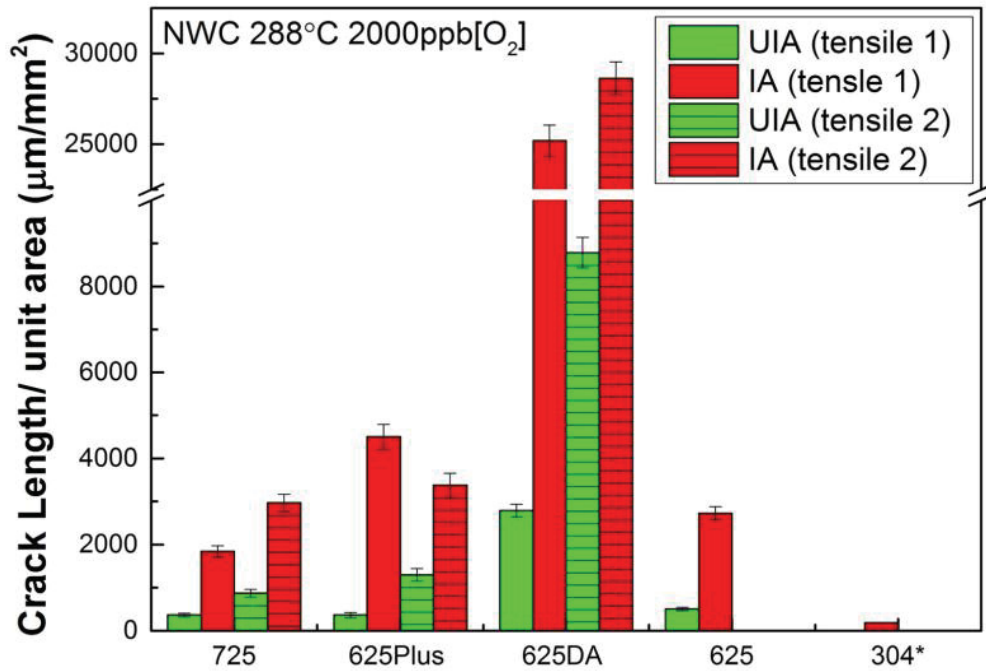


Figure 4-45 Crack length per unit area in both irradiated and non-irradiated areas of alloy 625, alloy 625Plus and alloy 725 irradiated to a dose of ~ 5 dpa and strained to ~ 4% in BWR-NWC environment, *data from literature.

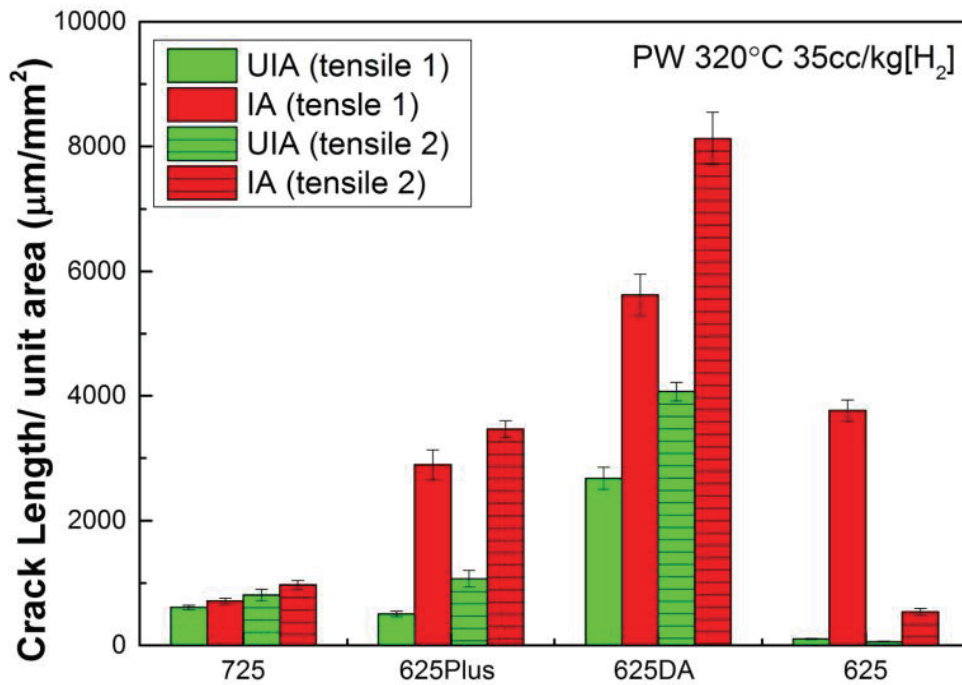


Figure 4-46 Crack length per unit area in both irradiated and non-irradiated areas of alloy 625, alloy 625Plus and alloy 725 irradiated to a dose of ~ 5 dpa and strained to ~ 4% in PWR-PW environment.

Table 4-11 Crack data for alloy 625, alloy 625Plus, and alloy 725 irradiated to a dose ~ 5 dpa and strained to ~ 4% in BWR-NWC environment.

Alloy	Env.	Area	Cracks counted	Average crack length (μm)	Crack density (#Cracks/ mm^2)	Crack length/unit area ($\mu\text{m}/\text{mm}^2$)	Cracked length/ HAGB length (%)	
625Plus	NWC-1	UIA	28	12 ± 2	30 ± 0.2	364 ± 160	2.41 ± 0.44	
		IA	204	26 ± 2	171 ± 1	4502 ± 291	29.78 ± 0.07	
	NWC-2	UIA	110	11 ± 1	118 ± 1	1295 ± 147	8.56 ± 0.11	
		IA	210	15 ± 1	226 ± 1.4	3377 ± 280	22.33 ± 0.08	
	PW-1	UIA	83	6 ± 0.5	89 ± 0.5	503 ± 47	3.33 ± 0.09	
		IA	244	11 ± 1	263 ± 2	2895 ± 239	19.15 ± 0.08	
	PW-2	UIA	94	11 ± 1	101 ± 1	1069 ± 131	7.07 ± 0.12	
		IA	186	17 ± 1	200 ± 1	3465 ± 265	22.92 ± 0.08	
	725	NWC-1	UIA	41	8 ± 1	44 ± 0.3	365 ± 47	1.08 ± 0.13
			IA	191	9 ± 1	206 ± 1	1847 ± 129	5.45 ± 0.07
NWC-2		UIA	60	14 ± 1	131 ± 1	875 ± 89	2.58 ± 0.1	
		IA	154	18 ± 1	166 ± 1	2967 ± 196	8.75 ± 0.07	
PW-1		UIA	111	5 ± 0.3	119 ± 1	609 ± 37	1.8 ± 0.06	
		IA	118	6 ± 0.4	127 ± 1	711 ± 48	2.1 ± 0.07	
PW-2		UIA	78	8 ± 1	106 ± 1	807 ± 90	2.38 ± 0.11	
		IA	84	8 ± 1	114 ± 1	968 ± 73	2.86 ± 0.08	
625DA	NWC-1	UIA	97	10 ± 0.5	292 ± 2	2792 ± 150	1.00 ± 0.05	
		IA	526	13 ± 0.4	1982 ± 11	25196 ± 862	9.02 ± 0.03	
	NWC-2	UIA	166	8 ± 0.3	1072 ± 7	8785 ± 355	3.14 ± 0.03	
		IA	481	9 ± 0.3	3107 ± 20	28632 ± 900	10.25 ± 0.03	
	PW-1	UIA	66	6 ± 0.4	426 ± 3	2676 ± 177	1.00 ± 0.07	
		IA	117	7 ± 0.3	756 ± 5	5620 ± 332	2.01 ± 0.06	
	PW-2	UIA	182	7 ± 0.3	588 ± 4	4067 ± 148	1.46 ± 0.04	
		IA	316	8 ± 0.4	1020 ± 6	8127 ± 421	2.91 ± 0.06	
625	NWC-1	UIA	61	8 ± 0.6	66 ± 0.4	503 ± 41	0.57 ± 0.08	
		IA	217	12 ± 0.6	234 ± 0.7	2728 ± 152	3.1 ± 0.06	
	PW-1	UIA	19	5 ± 0.5	20 ± 0.1	103 ± 10	0.12 ± 0.1	
		IA	403	9 ± 0.4	434 ± 3	3762 ± 171	4.28 ± 0.05	
	PW-2	UIA	12	5 ± 0.4	13 ± 0.1	59 ± 8	0.07 ± 0.1	
		IA	59	8 ± 0.9	63 ± 0.4	537 ± 54	0.61 ± 0.1	

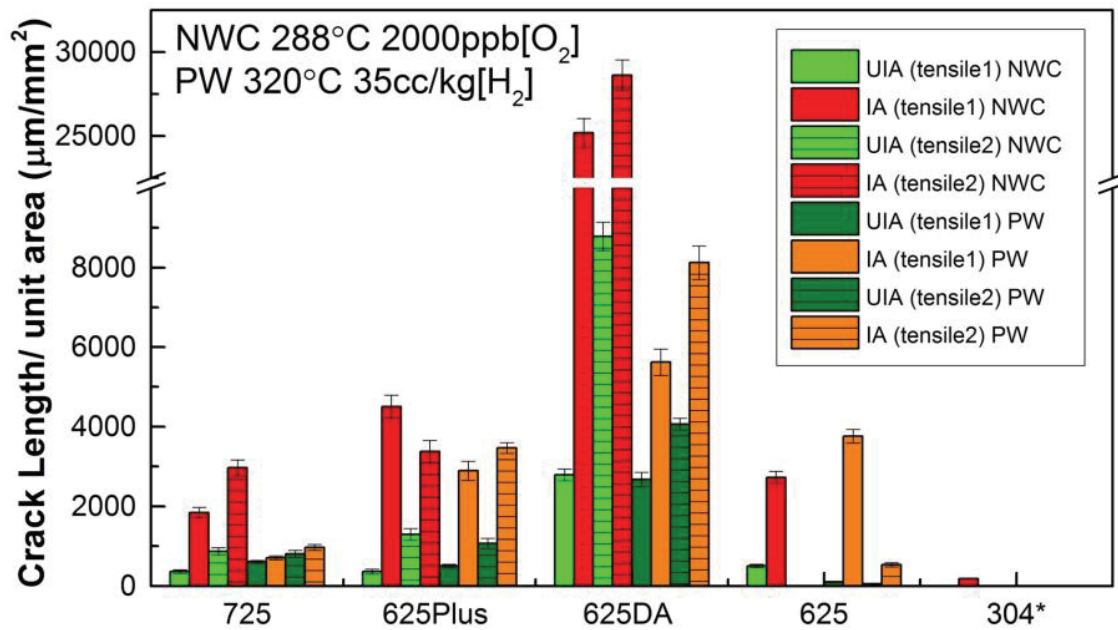


Figure 4-47 Crack length per unit area in both irradiated and non-irradiated areas of alloys 625Plus, 725, 625DA, and 625 irradiated to a dose of ~ 5 dpa and strained to ~ 4% in both BWR-NWC and PWR-PW environments.

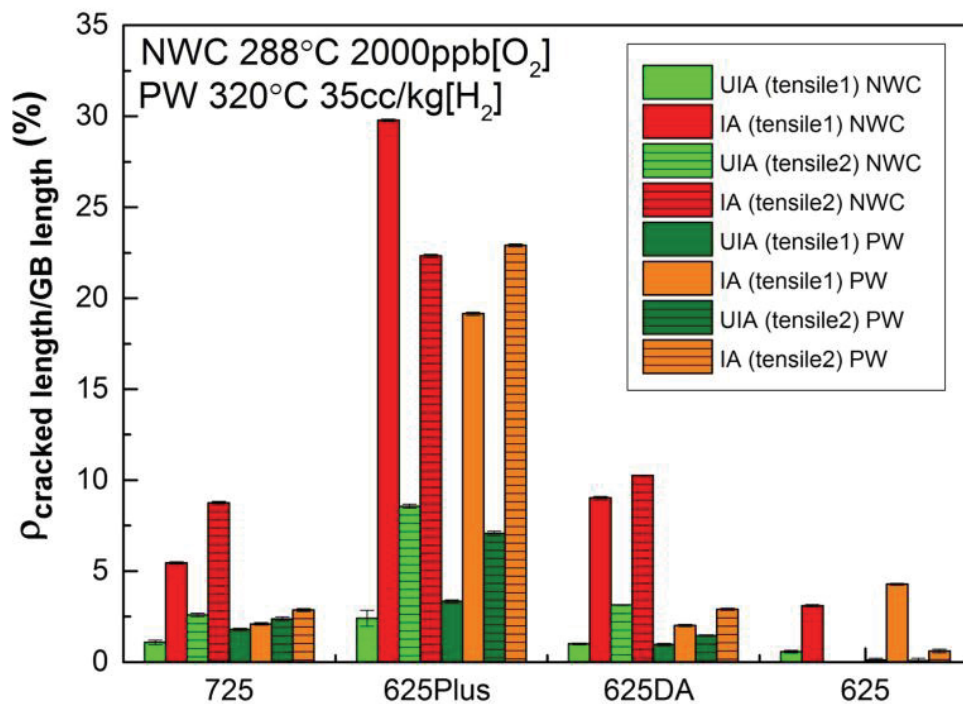


Figure 4-48 Ratio between cracked length and HAGB length in both irradiated and non-irradiated areas of alloys 625Plus, 725, 625DA, and 625 irradiated to a dose of ~ 5 dpa and strained to ~ 4% in both BWR-NWC and PWR-PW environments

5 DISCUSSION

5.1 Formation of LRO phase

Irradiation Enhanced Formation of LRO Phase

The data related to the LRO phase in commercial alloys are limited because of sluggish kinetics at low temperatures. It takes between 1000 and several tens of thousands of hours for a model or engineering alloy to form the LRO phase, and depends on the composition, aging temperature and thermo-mechanical treatment history. For example, LRO phase is observed in alloy 625 after service in petrochemical plant for 50,000h at 500°C [36], although it was identified as a commensurate superstructure. Young et al. performed systemic studies [37, 38] to identify the influence of cold work, quench rate, and alloying effects on the formation of LRO phase in model Ni-Cr-X alloys, which resembles alloy 690. They found that cold work delays the ordering process; Fe addition lowers the stable temperature of the ordered phase, while excess vacancies from quenching accelerate its formation. Irradiation can create vacancy concentrations that are orders of magnitude above that at thermal equilibrium. As a result, diffusion can be significantly enhanced. Both factors can lead to a rapid precipitation compared to thermal condition. Frely et al. [39] reported an enhanced LRO formation of a model alloy under electron irradiation. Meanwhile, ordering was absent in an engineering alloy with a similar composition. Related to engineering alloys, irradiation enhanced LRO has only been observed once in direct aged alloy 625 after neutron irradiation at a temperature of 360°C [40].

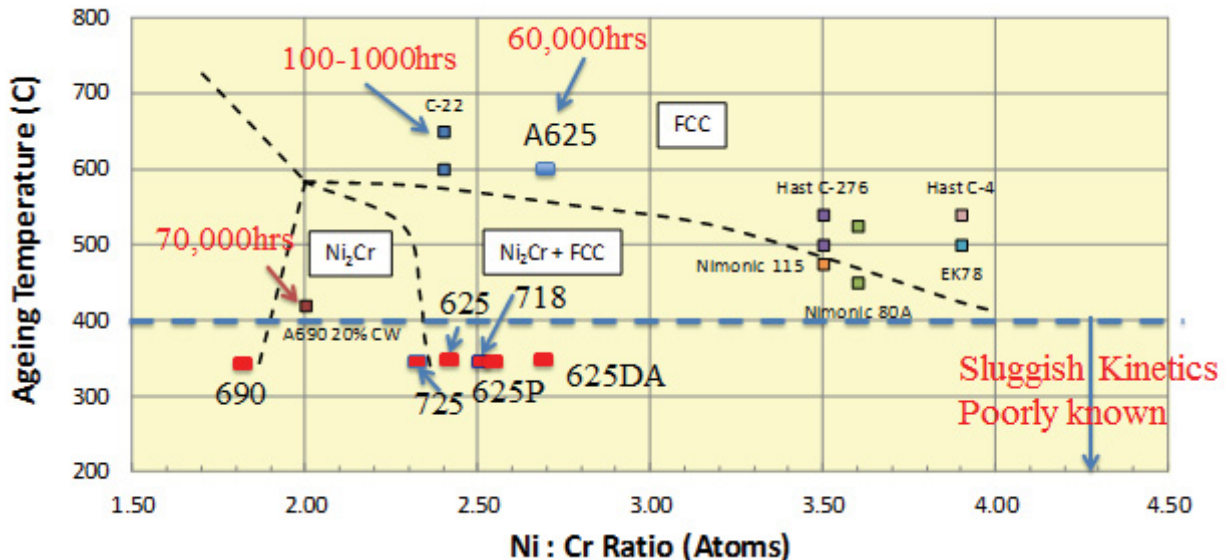


Figure 5-1 Engineering alloys reported to show LRO are relative to a recent Ni-Cr phase diagram [41] and alloys in current investigation (marked by red).

The LRO phase formed under thermal aging condition and the results were summarized in Figure 5-1. The LRO phase formed in all nickel base alloys 625, 625Plus, 625DA, 725 and alloy 690 after 5dpa proton irradiation. On the other hand, LRO phase was absent in alloy 725 aged for 1000h at the same temperature. This suggests that the LRO phase can be accelerated by at least an order of magnitude by irradiation. This emphasizes the fact that ion irradiation can be applied for phase transformation study in the case in which kinetics are sluggish and formation by thermal aging may take very long.

Effect of Iron on The Formation of LRO Phase

The effect of Fe on the formation of LRO was investigated by Young et al.[41]. They suggested that Fe can reduce the stability of LRO phase in a Ni-Cr-Fe model alloy. With the addition of Fe, the thermally stable range of Ni₂Cr was forced to lower temperature. Here, it is observed that Fe can reduce the volume fraction of LRO phase as shown in **Figure 5-2**, which is similar to their observation. The volume fraction of LRO is also very sensitive to the Fe when the content of Fe is small. As a result, significant differences in LRO volume fraction are noted among alloy 625DA, 625 and 625Plus. However, as the Fe content increases to 20% percent, no LRO phase was observed. The suppression of LRO phase by Fe is a very important observation because it can provide new design criteria for engineering alloys. If an alloy was designed to be hardened by LRO phase, the Fe should be minimized. On the contrary, Fe addition can be used to prevent the formation of the LRO phase.

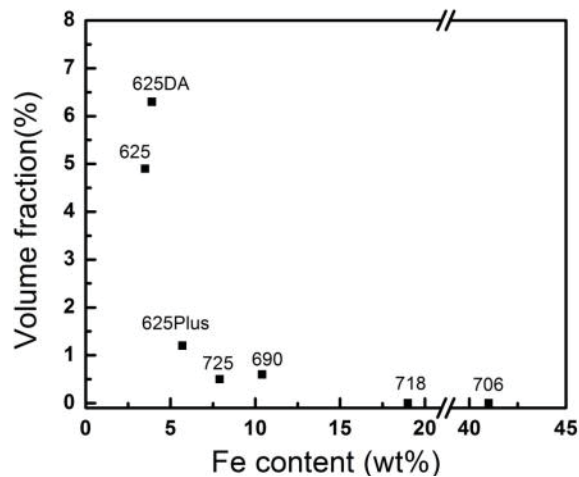


Figure 5-2 Iron reduced the volume fraction of LRO phase

5.2 IASCC Susceptibility of Nickel-Base Alloys

One major purpose for the ARRM program is to evaluate the IASCC resistance of the candidate alloys. Of the four nickel-base alloys studied, three were high strength alloys; alloy 625Plus, alloy 725, and 625DA, and only alloy 625 was low strength. Thus, the following section is a brief discussion on the IASCC susceptibility of these nickel-base alloys obtained in the program thus far with comparison to the existing data.

Discussion

High Strength Alloys

Alloy 625Plus, alloy 725, and alloy 625DA are all from the alloy 625 family used for high strength applications. Among the three alloys, alloy 725 had the lowest IASCC susceptibility in both BWR-NWC and PWR-PW environments. Further interpretation may be needed to understand the IASCC mechanism; however, it is clear that alloy 625DA and alloy 625Plus were both highly susceptible to IASCC.

There are two parameters used to evaluate the IASCC behavior, either crack length per unit area or fraction of cracked grain boundary. These two parameters provide somewhat different information. Crack length per unit area is the total length of all the cracks in the sample per unit area observed. It combines both the crack density and the crack length and in fact, is approximately equal to the product of the average of both. It directly indicates the performance of the alloy from the application/engineering point view. Fraction of cracked grain boundary, on the other hand, is a measure of the fraction of the total grain boundary length that has cracked. It also is independent of grain size. Usually, grain size has an influence on SCC behavior, with increasing SCC susceptibility with grain size. But, some processes used to reduce grain size may leave defects on grain boundaries (such as, precipitates, carbides, etc.) which could cause an increase on IASCC susceptibility. Therefore, for one alloy, if either the value of cracking length per unit area or fraction of cracked grain boundary is high, the IASCC susceptibility is high. Although, from the perspective of ARRM program, crack length per unit area is the criteria used more often for evaluation.

Figure 5-3 illustrates a direct ranking of IASCC susceptibility versus radiation hardening and microstructural changes due to irradiation. Using the metric of crack length per unit area, 625DA had the highest cracking susceptibility. Also, 625DA had the highest hardness after irradiation and the most radiation hardening. Moreover, 625DA also had the most microstructural changes due to irradiation, the change in existing precipitates, formation of LRO phase, formation of dislocation loops, and the lowest Cr concentration at the grain boundary. Thus, the alloy that had the greatest change in microstructural features also had the highest IASCC susceptibility. However, this makes it hard to determine which parameter controls the IASCC behavior. Alloy 725 had the lowest IASCC susceptibility, which also had the least amount of change in microstructure after irradiation, except for the radiation induced segregation (RIS). It almost had the same level of Cr concentration at the grain boundary as did 625DA. Therefore, it revealed that RIS did not play an important role on IASCC susceptibility for high strength nickel-base alloys.

Using the metric of fraction of cracked grain boundary, 625Plus is the most susceptible alloy among all in both water environments, Figure 5-3. Once the crack length is normalized to the high angle grain boundary (HAGB) length, it was considered that the grain size effect was eliminated. As listed in the figure, the grain size of 625Plus was 10 times larger than that for 625DA. In addition, the HAGB length per unit area of 625DA was around 20 times more than that of 625Plus (EBSD results shown in Table 4-2). Therefore, the ranking of 625DA dropped while 625Plus increased due to the mathematic calculation. Physically, it also suggested that over 25% of the grain boundaries in alloy 625Plus were cracked after an irradiation dose of 5 dpa. Although the microstructural changes induced by irradiation might not be that significant in 625Plus, it was highly susceptible to IASCC. Meanwhile, alloy 725, with an intermediate grain

size, still had the lowest ranking even by this metric. Together with the ranking of microstructural changes, alloy 725 was the most IASCC resistant material in LWR environments among all the high strength alloys studied in the ARRM program.

It is worth noting that the IASCC data of high strength alloys used in LWRs are limited. The alloys with the most data are nickel-base alloy X-750 and alloy 718. Numerous studies [14, 40, 42, 43], have been reported on Alloy X-750 in both PWR-PW and BWR-NWC environments. Depending on the heat treatments, alloy X-750 may exhibit a fairly high SCC resistance in LWR environments; however, at the cost of a loss in mechanical properties. No direct comparison can be made with the high strength nickel-base alloys studied in the ARRM program with alloy X-750 in reference because first the SCC susceptibility varies significantly with the heat treatments and second the criteria are so different. The comparison between alloy X-750 and alloy 625 with the same HTH heat treatment [40] showed that alloy 625 had a higher IASCC resistance than did alloy X-750 in PWR environment. Alloy 718 [44-46] on the other hand, was reported to have much higher SCC resistance if the heat treatment was appropriate to the corresponding environment. Although, most studies for alloy 718 for nuclear applications were used in PWRs, both alloy 718 and alloy X-750 are now added in the ARRM program scope, making a thorough evaluation of high strength alloys possible soon. In this case, alloy X-750 will be considered the control alloy to which other high strength alloys will be compared.

Low Strength Alloys

Alloy 625 was the only low strength alloy that was tested so far in this program. A comparison of crack length per unit area for alloy 625 and Type 304 austenitic stainless steel (commercial grade) of which the data coming from Jiao *et al.* [33] were plotted in the previous section (**Figure 4-45**). The data for Type 304 austenitic stainless steel came from experiments conducted under conditions (irradiation and CERT environment) similar to those for alloy 625. Clearly, the crack length per unit area of alloy 625 is much higher than that for Type 304 stainless steel in the irradiated area. Moreover, for the non-irradiated area, there is no cracking reported for the Type 304 austenitic stainless steel. In brief, from the point view of IASCC susceptibility, alloy 625 seems to be higher than Type 304 austenitic stainless steel in the BWR-NWC environment.

Discussion

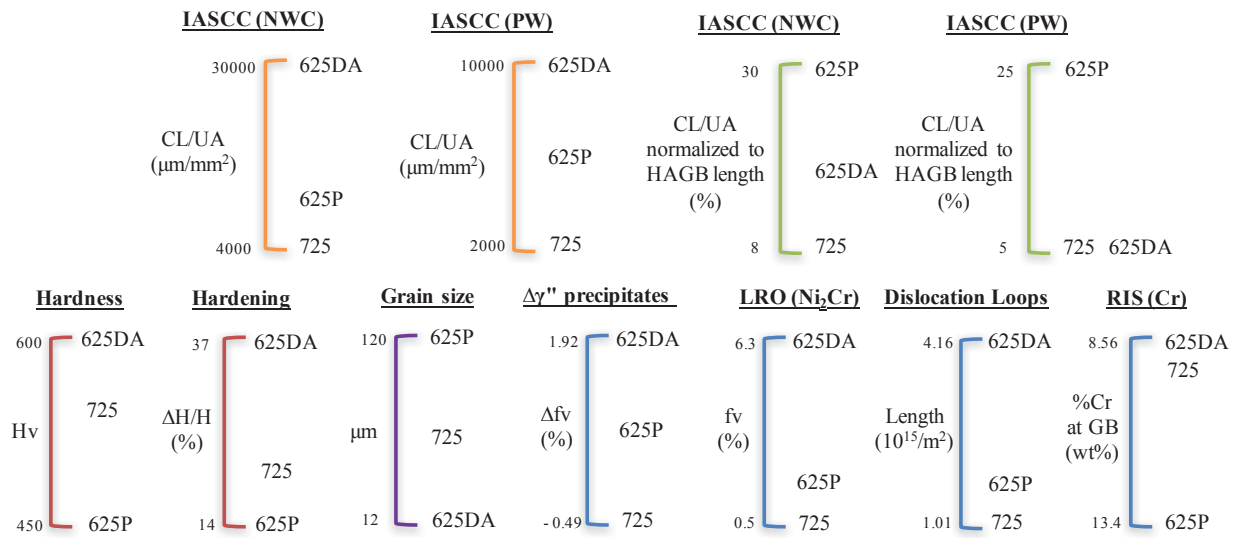


Figure 5-3 IASCC behavior of high strength nickel-base alloys versus irradiation hardness and change in microstructural features due to irradiation

6 CONCLUSIONS

Over the period between December 2015 and January 2017, proton irradiations were conducted on several alloys including alloys 690, 310, 800, X750, C22 and T92. Pre-characterization of these materials was performed to identify the phase structure and evaluate the homogeneity of as-received materials. Post-irradiation analysis, irradiation hardening and CERT test were performed to evaluate the response of the alloys to proton irradiation and to evaluate their resistance to IASCC. Major findings are as follows:

- The austenitic stainless steels and non-precipitation hardened nickel base alloys show a similar feature of white clean grain structure. T92 steel shows a hierarchy microstructure including prior austenitic grain boundary, lath boundaries and carbides.
- Dislocation loops prevail in the irradiated microstructure while voids were limited to a few alloys.
 - Dislocation loops formed in all the alloys irradiated with the largest loops in alloy 800 about ~50 nm and smallest loops in 625DA about ~13nm, with all the other materials in-between. The loop density is the reverse, alloy 625DA is on the order of $10^{23}/\text{m}^3$ about 40 times that of alloy 800.
 - Voids were observed in Type 310 with a size less than 10 nm and swelling less than 0.28%. No voids were observed in alloy 625, 625DA, 625Plus, 725, 690 and 800.
- Both irradiation enhanced and induced precipitates were observed.
 - Irradiation enhanced long range ordered phase (Ni_2Cr) was observed in most of the nickel base alloys (alloy 625, 625Plus, 625DA, 725, 690, C22) after proton irradiation. The volume fraction of LRO phase is determined primarily by the Fe content. With the addition of Fe, the volume fraction of LRO phase is decreased. The precipitation of LRO phase can be enhanced by a least an order of magnitude compared to thermal aging.
 - Irradiation induced γ' phase was observed in alloy 690 and 800, with the chemical composition is $\text{Ni}_3(\text{Ti}, \text{Al})$ in 690 and Ni_3Si in alloy 800. The Ni_3Si in alloy 800 is dominated by sinks and precipitation around dislocation is observed.
- RIS were observed in all these alloys tested.
 - In nickel base alloy 625, 625Plus and 625DA and 725, the as-received alloys show a depletion of Ni, and enrichment of Cr and Mo and GB. After irradiation, Ni is enriched, and Cr and Fe are depleted at GBs. Mo diffuses slowly away from GBs. RIS of other elements is insignificant. RIS differences among these alloys is insignificant.
 - In austenitic steels, type 310 exhibits significant grain boundary Cr depletion and Ni enrichment and alloy 800 shows little enrichment/depletion in the as-received

conditions. Significant RIS is observed where Ni is enriched and Cr, Fe is depleted at GBs. Si is segregated to GBs more than three times its nominal composition. RIS of other elements is insignificant.

- All the alloys were subjected to the irradiation hardening.
 - Irradiation hardening was significant in austenitic stainless steels alloy 310, 800 and non-precipitation hardening nickel base alloys C22 and 690. Alloy C22 shows the highest amount of irradiation hardening up to 150%. Alloy 625 shows slightly lower irradiation hardening compared to these alloys.
 - Irradiation hardening was lower in the precipitation hardened alloys (725, 625DA, 625Plus, X750 and 718) with less than 25% hardening. Alloy 718 showed no irradiation hardening.
 - Grade T92, the only F/M steel tested in the program, shows barely any irradiation induced hardening.
- Evaluation of IASCC behavior of the high strength nickel-base alloys (alloys 625Plus, 725, and 625DA) in both BWR-NWC and PWR-PW was made:
 - Alloy 725 had the highest yield strength among all the high strength nickel-base alloys and exhibit the lowest IASCC susceptibility in both environments.
 - Alloy 625Plus and alloys 625DA had similar mechanical properties and they were both highly susceptible to IASCC.
 - The IASCC susceptibility of 625DA was correlated with the changes in microstructure after irradiation; however, no indication of dominant features could be found.
 - RIS does not play an important role in the IASCC susceptibility of high strength nickel-base alloys tested in this project.
 - A high electrochemical potential environment significantly enhanced cracking behavior, IASCC susceptibility is higher in BWR-NWC than in PWR-PW.
- Evaluation of IASCC behavior of low strength nickel-base alloy 625 in both BWR-NWC and PWR-PW was made:
 - Alloy 625 had an intermediate IASCC susceptibility compared to that for the high strength nickel-base alloys.
 - For the low strength alloy, alloy 625 was much more susceptible to IASCC than a reference alloy (austenitic stainless steel Type 304) in BWR-NWC environment.
 - The cracking behavior of 625 in PWR-PW is still not clear.

Based on the microstructure, alloy 310 showed the best phase stability under irradiation. All nickel-base alloys (625, 625DA, 625Plus, 690, C22, 725) exhibited formation of a LRO phase. Nickel-base alloys exhibited less RIS compared to austenitic stainless steels. Voids were limited to alloy 310 with 0.28% swelling. Irradiation hardening was insignificant in alloy 718 and T92. High strength (precipitation hardened) alloys generally shows less irradiation hardening compared to low strength alloys.

Conclusions

Based on the IASCC susceptibility in both BWR-NWC and PWR-PW environments, high strength alloy 625Plus and alloy 625DA exhibited very high IASCC susceptibility following proton irradiation to 5 dpa and alloy 725 showed the lowest IASCC susceptibility. Although the IASCC susceptibility of alloy 625 in primary water is still not clear at this stage, it also exhibited a higher IASCC susceptibility than austenitic stainless steel type 304 in BWR-NWC environment.

7 REFERENCES

-
- [1] IASCC Susceptibility and Evolution of Microstructure in Several Ni-Base Alloys after Proton Irradiation, EPRI, 3002007461, (2016).
- [2] P. Scott. A review of irradiation assisted stress corrosion cracking, *J. Nucl. Mater.* 211 (1994) 101-122.
- [3] E. Kenik, R. Jones, G. Bell. Irradiation-assisted stress corrosion cracking, *J. Nucl. Mater.* 212 (1994) 52-59.
- [4] G.S. Was, S.M. Bruemmer. Effects of irradiation on intergranular stress corrosion cracking, *J. Nucl. Mater.* 216 (1994) 326-347.
- [5] J. Busby, G. Was, E. Kenik. Isolating the effect of radiation-induced segregation in irradiation-assisted stress corrosion cracking of austenitic stainless steels, *J. Nucl. Mater.* 302 (2002) 20-40.
- [6] G. Was, P. Ampornrat, G. Gupta, S. Teysseyre, E. West, T. Allen, K. Sridharan, L. Tan, Y. Chen, X. Ren. Corrosion and stress corrosion cracking in supercritical water, *J. Nucl. Mater.* 371 (2007) 176-201.
- [7] S.J. Zinkle, G. Was. Materials challenges in nuclear energy, *Acta Mater.* 61 (2013) 735-758.
- [8] G. Was, Y. Ashida, K. Stephenson, A. Flick, P. Andresen. Identifying Mechanisms and Mitigation Strategies for Irradiation Assisted Stress Corrosion Cracking of Austenitic Steels in LWR Core Components, EPRI 3002003105 (2014).
- [9] S. Bruemmer. New Issues Concerning Radiation-Induced Material Changes and Irradiation-Assisted Stress Corrosion Cracking in Light Water Reactors. Proc. 10th Int. Conf. Environmental Degradation of Materials in Nuclear Power Systems—Water Reactors (Houston, TX: NACE, 2002), 2002.
- [10] O. Chopra, A. Rao. A review of irradiation effects on LWR core internal materials—Neutron embrittlement, *J. Nucl. Mater.* 412 (2011) 195-208.
- [11] O. Chopra, A. Rao. A review of irradiation effects on LWR core internal materials—IASCC susceptibility and crack growth rates of austenitic stainless steels, *J. Nucl. Mater.* 409 (2011) 235-256.
- [12] P. Andresen, F. Garner, J. Gorman, S. Maloy, J. Nelson, L. Tan, M. Toloczko, G. Was. Critical Issues Report and Roadmap for the Advanced Radiation-Resistant Materials Program 1026482, EPRI 1026482 (2012).
- [13] F.A. Garner, B.M. Oliver, L.R. Greenwood, D.J. Edwards, S.M. Bruemmer, M.L. Grossbeck. Generation and retention of helium and hydrogen in austenitic steels irradiated in a variety of LWR and test reactor spectral environments. Pacific Northwest National Laboratory (PNNL), Richland, WA (US), 2002.
- [14] M. Miglin, H. Domian. Microstructure and stress corrosion resistance of alloys X750, 718, and A286 in light water reactor environments, *Journal of materials engineering* 9 (1987) 113-132.

- [15] G. Smith, D. Tillack, S. Patel. Alloy 625: impressive past, significant presence, awesome future, *Superalloys 718,625,706 and various derivatives* (1991) 35-46.
- [16] L.E. Shoemaker. Alloys 625 and 725: trends in properties and applications, *Superalloys 718, 625, 706 and derivatives* (2005) 409-418.
- [17] J.M. Rakowski, C.P. Stinner, M. Lipschutz, J. Preston Montague. The use and performance of wrought 625 alloy in primary surface recuperators for gas turbine engines, *Superalloys 718, 625, 706 and derivatives* (2005) 271-286.
- [18] S. Mannan, E. Hibner, B. Puckett. *Physical Metallurgy of Alloys 718, 725, 725H, and 925 for Service in Aggressive Corrosive Environments*, CORROSION (2003).
- [19] R.B. Bhavsar, A. Collins, S. Silverman. Use of alloy 718 and 725 in oil and gas industry, *Superalloys 718, 625, 706 and Various Derivatives* (2001) 47-55.
- [20] K.A. Esaklul, T.M. Ahmed. Prevention of failures of high strength fasteners in use in offshore and subsea applications, *Engineering Failure Analysis* 16 (2009) 1195-1202.
- [21] J.P.B. J.F.Ziegler. SRIM 2013 Program, IBM Corporation, Yorktown ,NY.
- [22] G. Gupta, Z. Jiao, A. Ham, J. Busby, G. Was. Microstructural evolution of proton irradiated T91, *J. Nucl. Mater.* 351 (2006) 162-173.
- [23] K.J. Stephenson, G.S. Was. The role of dislocation channeling in IASCC initiation of neutron irradiated stainless steel, *J. Nucl. Mater.* 481 (2016) 214-225.
- [24] D. Brandon. The structure of high-angle grain boundaries, *Acta Metall.* 14 (1966) 1479-1484.
- [25] K.C. Russell. Phase stability under irradiation, *Prog. Mater Sci.* 28 (1984) 229-434.
- [26] C. Cawthorne, E. Fulton. Voids in irradiated stainless steel, *Nature* 216 (1967) 575-576.
- [27] Z. Jiao, J. Busby, G. Was. Deformation microstructure of proton-irradiated stainless steels, *J. Nucl. Mater.* 361 (2007) 218-227.
- [28] F. Carrette, M. Lafont, G. Chatainier, L. Guinard, B. Pieraggi. Analysis and TEM examination of corrosion scales grown on Alloy 690 exposed to pressurized water at 325 C, *Surface and interface Analysis* 34 (2002) 135-138.
- [29] A. Machet, A. Galtayries, S. Zanna, L. Klein, V. Maurice, P. Jolivet, M. Foucault, P. Combrade, P. Scott, P. Marcus. XPS and STM study of the growth and structure of passive films in high temperature water on a nickel-base alloy, *Electrochimica Acta* 49 (2004) 3957-3964.
- [30] L. Marchetti, S. Perrin, Y. Wouters, F. Martin, M. Pijolat. Photoelectrochemical study of nickel base alloys oxide films formed at high temperature and high pressure water, *Electrochimica Acta* 55 (2010) 5384-5392.
- [31] M. Sennour, L. Marchetti, F. Martin, S. Perrin, R. Molins, M. Pijolat. A detailed TEM and SEM study of Ni-base alloys oxide scales formed in primary conditions of pressurized water reactor, *J. Nucl. Mater.* 402 (2010) 147-156.
- [32] L. Marchetti-Sillans. PhD thesis (2007).
- [33] Z. Jiao, G. Was. Localized deformation and IASCC initiation in austenitic stainless steels, *J. Nucl. Mater.* 382 (2008) 203-209.
- [34] D. Macdonald. The electrochemical nature of stress corrosion cracking, *Stress Corrosion Cracking of Nickel Based Alloys in Water-Cooled Nuclear Reactors: The Coriou Effect* (2016) 239.
- [35] G.S. Was, "Irradiation Assisted Corrosion and Stress Corrosion Cracking (IAC/IASCC) in nuclear reactor systems and components" in *Nuclear Corrosion Science and Engineer*, Woodhead Publishing, 2012. .

- [36] C. Thomas, P. Tait. The performance of Alloy 625 in long-term intermediate temperature applications, *Int.J.Pres. Ves. Pip.* 59 (1994) 41-49.
- [37] G. Young, J.D. Tucker, D. Eno. The kinetics of long range ordering in Ni-Cr and Ni-Cr-Fe alloys, 16th International Conference on Environmental Degradation of Materials in Nuclear Power Systems—Water Reactors, ed. P.L. Andresen (Houston, TX: NACE, 2013). (2013).
- [38] G. Young, D. Eno. Long range ordering in model Ni-Cr-X alloys, *Fontevraud 8* (Paris, France: SFEN,2014) (2014).
- [39] E. Frely, B. Beuneu, A. Barbu, G. Jaskierowicz. Short and Long-Range Ordering of (Ni 0.67 Cr 0.33) 1-x Fe x Alloys Under Electron Irradiation. *MRS Proceedings*, vol. 439: Cambridge Univ Press, 1996. p.373.
- [40] R. Bajaj, W. Mills, M. Lebo, B. Hyatt, M. Burke. Irradiation-assisted stress corrosion cracking of HTH Alloy X-750 and Alloy 625. *Seventh International Symposium on Environmental Degradation of Materials in Nuclear Power Systems--Water Reactors.*, vol. 2, 1995. p.1093-1107.
- [41] G. Young, D. Eno. Long range ordering in model Ni-Cr-X alloys, (2015).
- [42] J. Olivera, J. Pierrey, F. Le Naour, D. Gilbon, R. Cauvin. Failure of Inconel X-750 bolts of internals of the CHOOZ-A nuclear power plant. *CEA Centre d'Etudes Nucleaires de Fontenay-aux-Roses*, 1989.
- [43] A.A. Stein and M.S. Gennaro, “Material Specification for Alloy X-750 for use in LWR Internal Components”, EPRI NP-7032, 1990.
- [44] J.M. Rakowski, C.P. Stinner, M. Lipschutz, J. Montague. The use and performance of wrought 625 alloy in primary surface recuperators for gas turbine engines, *Proceedings of Superalloys 718* (2005) 625-706.
- [45] S. Mannan, E. Hibner, B. Puckett. *Physical Metallurgy of Alloys 718, 725, 725H, and 925 for Service in Aggressive Corrosive Environments*, CORROSION (2003).
- [46] R.B. Bhavsar, A. Collins, S. Silverman. Use of alloy 718 and 725 in oil and gas industry, *Minerals, Metals and Materials Society/AIME, Superalloys 718, 625, 706 and Various Derivatives(USA)* (2001) 47-55.